CHARACTERIZING EXCITED STATE TRANSPORT AND CHARGE CARRIER DYNAMICS IN LEAD HALIDE PEROVSKITES

by

Casey Lynn Hickey

A dissertation submitted in partial fulfillment
of the requirements for the degree

of

Doctor of Philosophy

in

Chemistry

MONTANA STATE UNIVERSITY
Bozeman, Montana

April 2020

DEDICATION

To my husband and parents, because this journey wasn’t mine alone.

AKNOWLEDGEMENTS

First and foremost, I would like to acknowledge my advisor, Dr. Erik Grumstrup. Dr. Grumstrup has been a tremendous mentor to me. It was a great joy and privilege to work in his lab over the past several years. Next, I would like to acknowledge the other members of my committee: Dr. Rob Walker, Dr. Rufus Cone, Dr. Aleks Rebane, and Dr. Mary Cloninger, each of whose dedication to teaching has benefited me greatly.

I would also like to acknowledge the National Science Foundation Graduate Research Fellowship, Montana State University, the Harlan Byker Research Assistantship, the Mildred Livingston Grant, and the Gordon Pagenkopf Award for financial support of me and my research.

Finally, I would like to thank the many colleagues who contributed to both my work and wellbeing over the years. In particular, I would like to acknowledge Dr. Märtha Welander whose support of me has been boundless.

TABLE OF CONTENTS

TABLE OF CONTENTS CONTINUED

TABLE OF CONTENTS CONTINUED

LIST OF TABLES

Table Page

LIST OF FIGURES

Figure Page

LIST OF FIGURES CONTINUED

ABSTRACT

Understanding fundamental processes which drive the behavior of photoexcited charge carriers is essential to the development of novel semiconducting materials. The studies presented in this work combine ultrafast microscopy with a novel data analysis technique to provide an in-depth characterization of the excited state transport and recombination dynamics which occur in a series of lead halide perovskites. An investigation of the impact halide composition has on recombination dynamics in $CsPbI_2Br$ revealed that trap-mediated recombination dominates at low fluences, with Auger recombination becoming increasingly important as the excitation density increases. Additionally, the average diffusivity measured for $CsPbI_2Br$ ($D_A = 0.27$ cm^2/s) is nearly 10x lower than that observed in $MAPbI_3$. Further, it was determined that the dielectric constants relevant to photoexcited charge carriers in $CsPbBr_3$ and $MAPbBr_3$ perovskites (11.5 and 13, respectively) are intermediate between the high and low frequency limits, and that halide chemistry plays an integral role in determining the screening ability of lead halide perovskites. By correlating charge carrier diffusivities to locally measured crystal quality, it was found that solution processing methods can cause subtle lattice defects which act to impede transport and risk going undetected by bulk measurement techniques. Finally, to improve upon the traditional method for extracting diffusivities from transport measurements, which relies on perfectly Gaussian point spread functions, a new method was developed which instead relies on a numerical convolution of the actual point spread function with the diffusion equation. Compared to the traditional Gaussian method, the numerical convolution method proved to more accurately determine the diffusion coefficient, especially in the case of an anomalous point spread function.

CHAPTER ONE

INTRODUCTION

1.1 Introductory Remarks

In 2009 the first mention of lead halide perovskites (LHPs) as light absorbers for solar cells marked the beginning of a new era in the photovoltaic community.[1] The unique photophysical properties of LHPs, combined with easy, low-cost fabrication techniques have provided exciting opportunities for researchers with the future design of photovoltaic and optoelectronic devices in mind. High optical absorption coefficients,[2] long carrier diffusion lengths,[3-4] chemical tunability,[5] and high photoconversion efficiencies,[6] have led to device applications which include solar cells, light emitting diodes,[7-8] lasers,[9-11] and photodetectors.[12-13] However, despite a decade of research and tremendous progress implementing LHPs into a variety of devices, a predominately trial and error approach to innovation has resulted in uncertainty regarding fundamental photophysical properties intrinsic to this class of material. For example, in the case of $CsPbBr_3$, values reported for the static dielectric range from 22 to $>10^3$,[14-15] and the carrier mobility values range from 20 – 4500 $cm^2/V\ s$[16-19].

Much of the reported variation in LHP properties stem from the fact that high-performance LHPs can be fabricated via a wide array of solution processing techniques. Solution processability, while advantageous for achieving low-cost devices, inherently introduces structural and chemical heterogeneities into the resulting thin-films.[20-22] Structural defects which act to impede transport can be detrimental to device performance

and need to be carefully considered. For example, defects introduced during fabrication have been shown to reduce both photoconversion efficiency and stability in LHP thin-film devices.[23] Further complications arise from chemical heterogeneity often introduced as a way to tune the band structure of LHPs. Again, while desirable for device design, modifying the chemical composition of LHPs can result in photoinduced ion migration,[24] bandgap instability,[25] and disorder in the energetic landscape of the material.[26]

Unfortunately, bulk measurement techniques with macroscopic probing volumes can only treat sample defects in an average way and as a result provide an incomplete picture of the underlying photophysics. Therefore, to obtain a more complete understanding of charge carrier transport and decay dynamics in LHPs it is necessary to employ microscopy techniques capable of making precise correlations between structure and functional properties observed in this class of material. Ultrafast microscopy, with high spatial (sub-micron) and temporal (sub-picosecond) resolution, has emerged as an effective tool for characterizing photoinduced excitations in disordered and low dimensional semiconductors.[27-29] Resolution at the length-scale of structural heterogeneities provides a means for understanding how structural and chemical disorder impact the behavior of photoexcited charge carriers.

This dissertation summarizes efforts aimed at disentangling the impacts of chemical and structural heterogeneity on properties intrinsic to lead halide perovskites. Through a series of ultrafast pump-probe microscopy (PPM) experiments and development of a more accurate and robust approach for measuring transport, we provide

novel insight into photophysical properties driving the behavior of photoexcited charge carriers in disordered semiconductors.

The remaining sections of Chapter 1 provides motivation for the work presented in the following chapters as well as necessary background summaries of both lead halide perovskites and pump-probe microscopy. Each of Chapters 2-5 are directed toward elucidating specific aspects of the photophysical properties of LHPs and how they are determined by structure and composition. Chapter 2 addresses the impact of partial halide substitution on carrier transport and decay dynamics in cesium lead mixed-halide perovskites. Chapter 3 provides insight into the role of halide chemistry on dielectric screening and how it determines the behavior of photoexcited charge carriers. Chapter 4 discusses the impact of subtle lattice defects on carrier transport and also provides a method for characterizing lattice strain in LHPs. Chapter 5 develops an alternative approach for analysis of spatially separated pump-probe microscopy images which provides more accurate diffusion coefficients, especially in the case of anisotropic diffusion and non-Gaussian shaped beams. Finally, Chapter 6 provides a summary and future directions for the work presented herein.

1.2 Lead Halide Perovskites

Perovskite is a mineral composed of calcium titanate ($CaTiO_3$) that was first discovered by Gustav Rose in 1839 and named after Russian mineralogist Lev Perovski.[30] Since that time, perovskite has lent its name to any compound with a crystal structure that follows the same form, ABX_3. In the ABX_3 structure, a divalent metal (B) coordinates with six anions (X) to form corner sharing octahedra $[BX_6]^{4-}$ which surround an A-site cation. Within the constraint of a Goldschmidt tolerance factor ($\tau = (r_A + r_X)/\sqrt{2}(r_B + r_X)$, where r is the ionic radius of the respective component) the perovskite structure can accommodate different combinations of elements (or molecules) represented by A, B and X.[31-33] After development of the tolerance factor, it was found that τ alone was not enough to reliably predict stable perovskite structures so an additional factor, the octahedral factor ($\mu = r_B/r_X$), has been added to increase predictability of the model.[34] Most perovskites have a tolerance factor value between 0.75 and 1.0, and an octahedral factor greater than 0.41.[35] In the ideal case, $\tau = 1$ and the crystal adopts a cubic lattice structure, however even the prototypical perovskite, calcium titanate, has an orthorhombic lattice structure and a tolerance factor of $\tau = 0.84$. In the case of lead halide perovskites, the divalent metal is lead ($r_B = 1.19$ Å) , X represents I ($r_X = 2.20$ Å), Br ($r_X = 1.96$ Å), or Cl ($r_X = 1.81$ Å), and the A-site cation is typically cesium ($r_A = 1.67$ Å), methylammonium (MA, $r_A = 1.8$ Å)[36] or formamidinium (FA, $r_A = 1.9 - 2.2$ Å)[37]. For stable LHPs at room temperature, τ is typically between 0.81 and 1.11 and μ is between 0.44 and 0.90.[37] When τ is between 0.89 and 1 the crystal is likely to form a cubic structure, and tetragonal or orthorhombic structures below 0.89.[37-38]

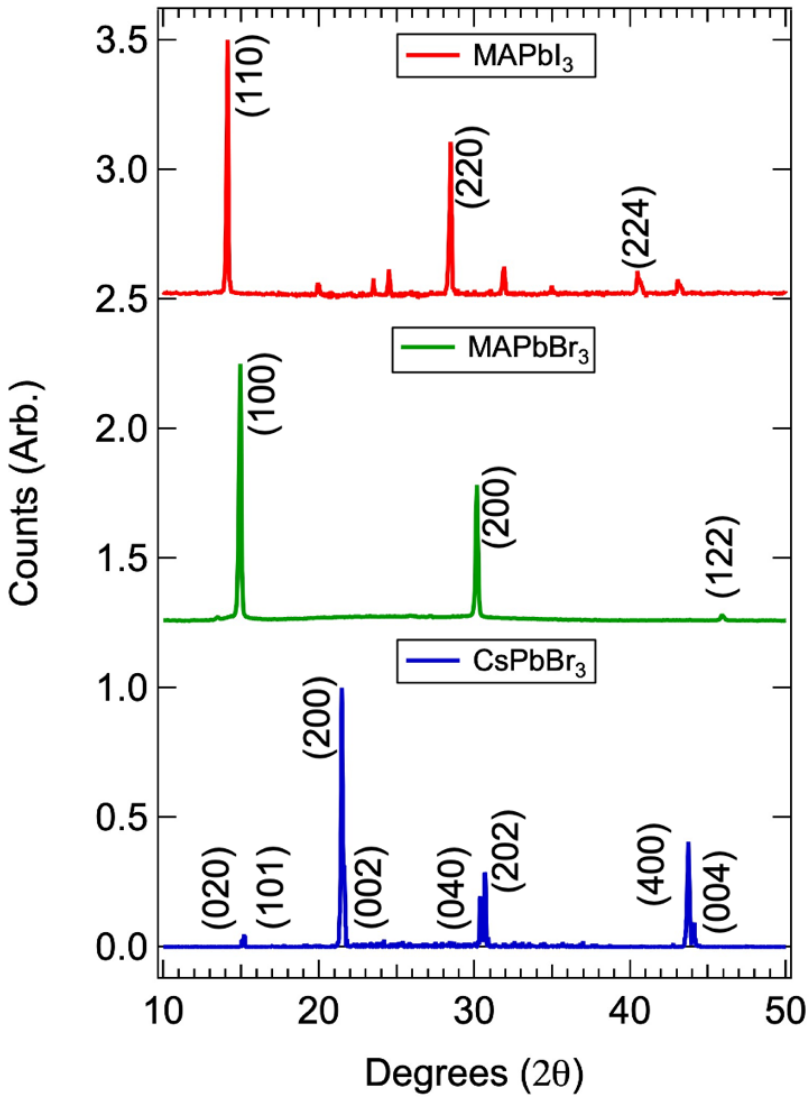

Figure 1.1. LHP XRD patterns. The red, green and blue traces represent XRD patterns for tetragonal $MAPbI_3$, cubic $MAPbBr_3$ and orthorhombic $CsPbBr_3$, respectively. $MAPbI_3$ (red) is shifted to smaller degrees (2θ) due to an expansion of the lattice, and $CsPbBr_3$ (blue) peaks is shifted to larger degrees (2θ) due to a contraction of the lattice relative to cubic $MAPbBr_3$.

For example, cubic $MAPbBr_3$ has a tolerance factor of $\tau = 0.91$, whereas tetragonal $MAPbI_3$ and orthorhombic $CsPbBr_3$ have tolerance factors of 0.83 and 0.81, respectively. XRD patterns presented in Figure 1.1 illustrate changes in lattice structure

due to chemical modification. Cubic $MAPbBr_3$ (green trace) has a lattice parameter of a_c = 5.919 Å. Substituting MA for a smaller Cs atom results in a contraction of the lattice to an orthorhombic geometry with pseudo-cubic lattice parameter of $a_{pc} \approx 5.85$ Å. Therefore, according to Bragg's Law ($n\lambda = 2dSin(\theta)$), the XRD pattern for $CsPbBr_3$ (blue trance) is shifted to larger diffraction angles, relative to $MAPbBr_3$. Alternatively, if bromide ions are substituted for larger iodide ions, the lattice expands slightly to a tetragonal geometry with a pseudo-cubic lattice parameter of $a_{pc} \approx 6.30$ Å. As a result, the XRD pattern for $MAPbI_3$ (red trace) is shifted to smaller diffraction angles, relative to $MAPbBr_3$.

For semiconductors like LHPs, the energy required to create an excited state in the material is determined by the bandgap energy (E_{bg}). The bandgap is simply the difference in energy between the conduction band (analogous to the LUMO) and the valence band (analogous to the HOMO) of the material. Distortions of the lattice, like those described above, have a direct impact on the band structure of the resulting material as illustrated in Figure 1.2. First principles calculations determine that the valence band maximum (VBM) in lead halide perovskites ($APbX_3$) is dominated by contributions from lead s and halide p antibonding states, whereas the conduction band minimum (CBM) is derived from poorly overlapped lead p and halide s orbitals. Due to the poor orbital overlap between the lead p and halide s orbitals the conduction band is relatively unaffected by chemical modifications of the halide or A-site cation species.[39-41] Thus, changes in bandgap energy that accompany chemical modification are primarily due to energy shifts of the valence band. For example, when iodide ions are substituted for

bromide ions orbital overlap between the lead p and halide s increases causing destabilization of the valence band.[41] As a result, the VBM shifts to higher energy (closer to the CBM) and the bandgap energy is reduced. Accordingly, the change in energy from $MAPbBr_3$ (panel B) to $MAPbI_3$ (panel A) is $\Delta E_{bg} = -0.68\ eV$. Alternatively, because the A-site cation doesn't directly contribute to bonding, changes in bandgap energy upon substitution result only from structural deformations of the lattice to accommodate a change in volume.[39, 41-42] Specifically, the octahedra tilt and cause a mild reduction of the Pb-X orbital overlap and as a result, the valence band energy is reduced. Consequently, a slight bandgap increase is observed ($\Delta E_{bg} = +0.07\ eV$) from $MAPbBr_3$ to $CsPbBr_3$ (panel C).

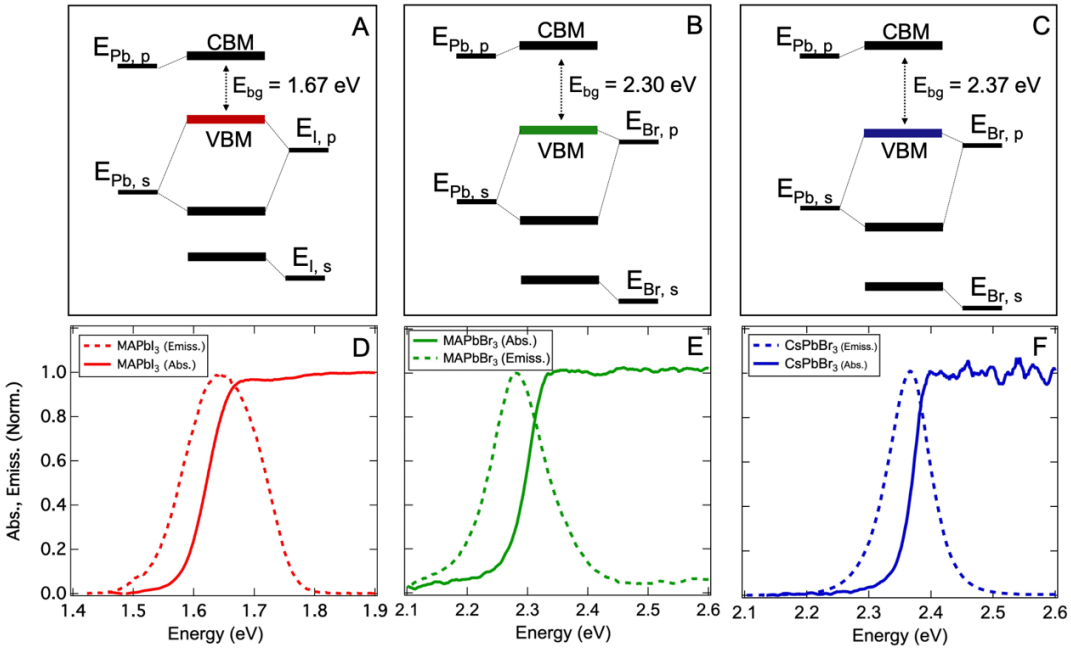

Figure 1.2. Bandgap tuning in LHPs. Diagrams of valence band shifting upon chemical substitution are shown in panels (A), (B) and (C), with the corresponding emission spectra (dashed lines) and absorption spectra (solid lines) collected from $MAPbI_3$, $MAPbBr_3$ and $CsPbBr_3$ perovskite thin films shown in panels (D), (E) and (F), respectively.

Bandgap tuning, combined with low non-radiative recombination rates, long carrier lifetimes and photoconversion efficiencies >23% (>25% for tandem LHP-Si cells as reported by NREL) have led to rapid innovation of LHP based technologies.[43] Further, with photoconversion efficiencies comparable to Si (~28%), several companies are beginning to invest in the commercial production of both tandem perovskite-silicon and perovskite modules.[44] The efficacy of LHPs as photovoltaics comes despite anisotropic lattice strain,[22] sub-grain boundaries,[45] surface defects,[46] and other non-uniformities resulting from simple solution processing techniques. So, while the commercial success of LHP devices remain to be seen, this class of material present a unique opportunity to study the role of structural and chemical heterogeneity in determining excited state carrier behavior in disordered materials. We explore the impact of various chemical modifications on LHP transport and recombination kinetics in Chapters 2 and 3.

1.3 Ultrafast Pump-Probe Microscopy

The foremost investigative tool used for this research is ultrafast pump-probe microscopy. Pump-probe microscopy (PPM) is a third-order (sample interacts once with the probe and twice with the pump) nonlinear spectroscopic technique used to study excited state dynamics of nano- and micro-scale materials. Simply put, PPM utilizes two pulses of different energies; a pump which creates an excited state population in the material, and a probe which monitors the spatial and temporal evolution of the photogenerated excited-state density via changes in the detected probe intensity.[47]

For semiconductors, the excited-state population is comprised of free electrons and holes, which we collectively refer to as free carriers, and excitons, which are

coulombically bound electron-hole pairs. The presence of an excited state population changes the material's dielectric function ($\hat{\varepsilon} = \varepsilon_r' + i\varepsilon_r''$).[48-52] The dielectric function is related to the complex index of refraction by Equation 1:

$$\hat{\varepsilon} = \hat{n}^2 = (n + ik)^2 \qquad (1)$$

where n is the refractive index and k is extinction coefficient. Free-carrier contributions to changes in the dielectric function are commonly described using the Drude model which treats the carriers as an electron-hole plasma, or small mobile particles interacting with large and relatively immobile, lattice ions.[53] When carriers are injected into a material (i.e. the material is photoexcited) the material's dielectric is reduced by an amount proportional to the density of free charges. In the limit that the probe energy is far below the material bandgap, k approaches 0 and photoinduced changes in the refractive index can be reduced to the real part of the complex refractive index function ($\varepsilon = n^2$). The relationship between photogenerated carrier density (N) and change in refractive index (Δn) can then be described by the following equation:

$$\Delta n = -\frac{Nq^2\tau^2}{2m^* n_0 \varepsilon_0 (1 + \omega^2\tau^2)} \qquad (2)$$

where q is the fundamental charge of an electron, τ is the mean carrier scattering time, m^* is the optical mass of the carrier, n_0 is the ground state refractive index of the material, ε_0 is the static permittivity and ω is the angular frequency of the probe pulse.[48, 52, 54-56] Since the change in reflectance scales with Δn, a convenient observable is the pump induced change in the reflected probe light $\left(\frac{\Delta R}{R} = \left(\frac{4\,\Delta n\,(1+\Delta n * n_0 - {n_0}^2}{(n_0-1)^2(1-\Delta n+n_0)^2}\right)\right)$.

Experiments designed to detect changes in the reflected probe light are referred to as

transient reflectivity (TR) experiments. Given Equation 2, the detected TR signal will be directly proportional to the density of photoexcited carriers providing a convenient way to track carriers as they move and recombine in the material.

Instrumentation

The primary excitation source for our homebuilt pump-probe microscope is a mode-locked Ti:Sapphire oscillator (80 MHz, ~70 fs) with a fundamental that is tunable from 690-1040 nm. The fundamental beam from the oscillator is split via a 50:50 beam splitter (b/s) into two separate lines, the pump and probe, which are modulated via acousto-optic modulators (AOMs) at 4 MHz and 8 MHz, respectively. Modulating the pump and probe at different frequencies enables lock-in detection of pump-induced changes in the probe intensity. To control the temporal and spatial coordinates of the probe relative to the pump, the probe is first directed onto a delay stage then coupled onto galvanometer mirrors (GV). The pump is coupled into either a continuum generating photonic crystal fiber (PCF) or Beta barium borate crystal (BBO) to tune the pump to a wavelength appropriate for the bandgap of the material under investigation. The pump and probe beams are then recombined and sent through a 4f lens system and focused via a 100x objective onto the sample, which is mounted onto a piezoelectric x, y translation stage. It is possible to place a second set of galvanometer mirrors and 4f lens system after the two beams are recombined to achieve spatial control of the pump and probe independently, rather than using an x,y translation stage. For transient reflectivity measurements, as diagramed in Figure 1.3, pump-induced changes in the reflected probe intensity are detected using a balanced photodiode and lock-in amplifier.

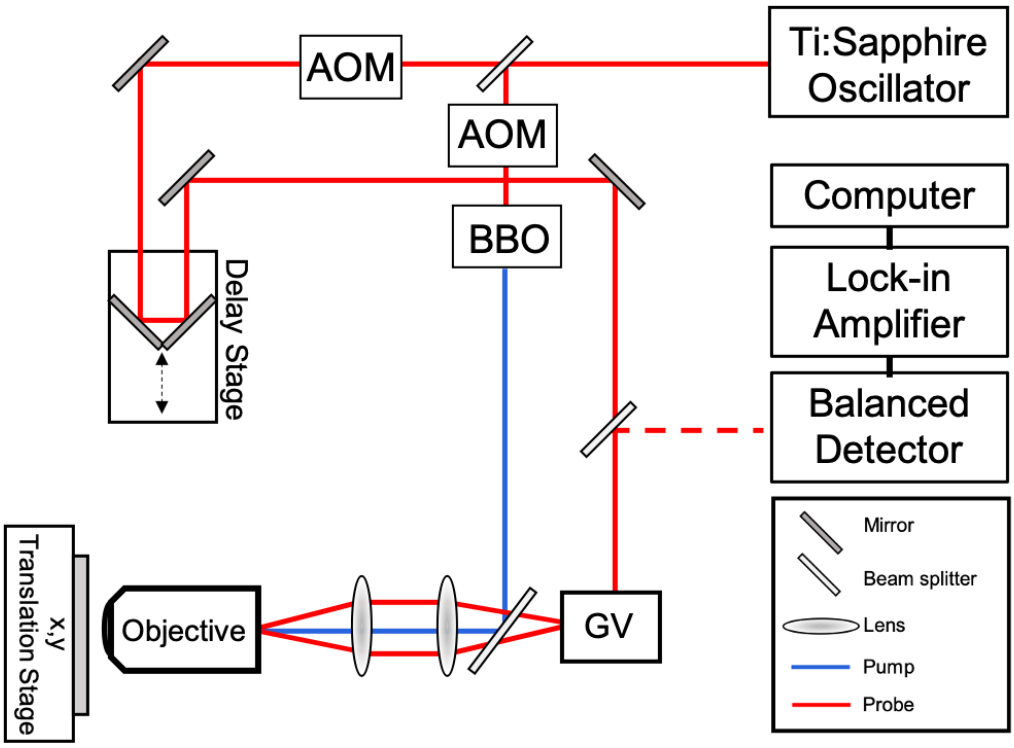

Figure 1.3. Diagram of a pump-probe microscope in reflective geometry. The fundamental out of the laser (red) is split into two lines. The probe (red) and the pump (blue). The probe beam is aligned onto a delay stage and then coupled onto a first set of galvanometer mirrors. Subsequently, the probe is recombined with the pump via a dichroic beam splitter and the two beams are coupled onto a second set of galvanometer mirrors and then directed onto the back aperture of a 100x objective. Pump-induced changes in the reflected probe beam are detected using a balanced photodiode and lock-in amplifier.

Measurements

The homebuilt pump-probe microscope described above is configured such that three types of measurements can be collected: decay kinetics, spatially overlapped images, and spatially separated images. Each measurement benefits from the sub-micron spatial resolution and sub-picosecond temporal resolution of the instrument to provides a direct probe of the ultrafast photophysical processes in single crystalline domains. While the diagram below illustrates a reflective geometry, each measurement can also be performed such that the transmitted probe light is detected.

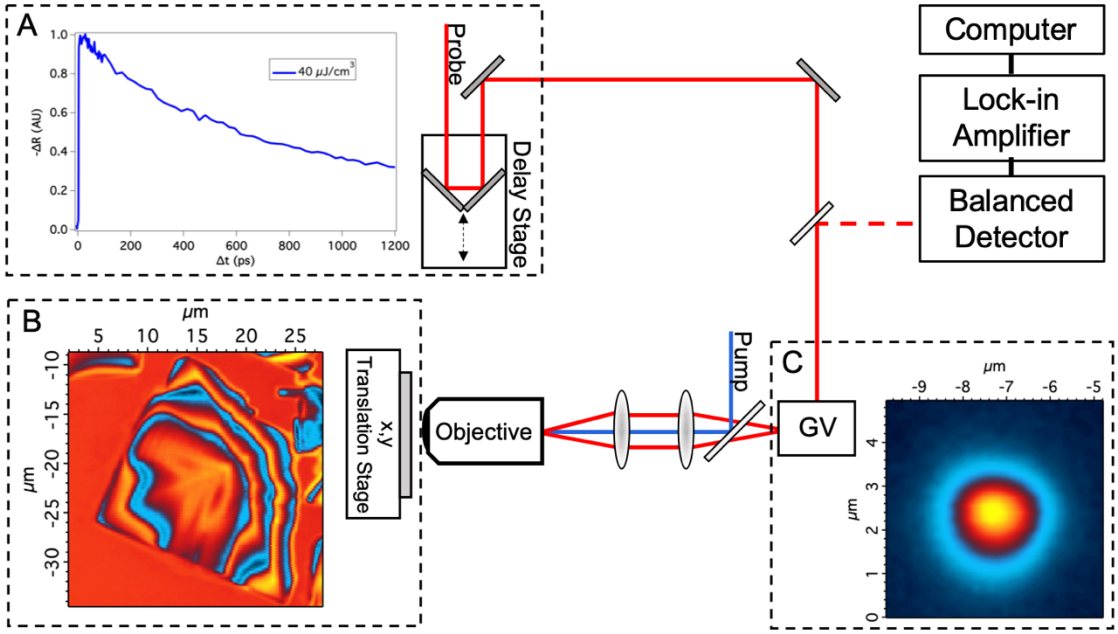

Figure 1.4. Pump-probe experimental measurements. (A) Kinetics trace collected by spatially overlapping the pump and probe beams while increasing their relative time delay via a translation stage. (B) Spatially overlapped pump-probe image taken by raster scanning a domain beneath the spatially overlapped pump and probe beams at a fixed temporal delay (t = 0ps). (C) Spatially separated pump-probe image taken by raster scanning the probe beam over the stationary, localized excitation at a fixed temporal delay (t = 1ps).

Power Dependent Decay Kinetics. Decay kinetics are collected by spatially overlapping the pump and probe beams while varying them temporally via a translation stage. By collecting a set of kinetics measurements at increasing pump-fluences and then globally fitting the data to the rate equation given by Equation 3, it is possible to determine the mechanism of carrier recombination which dominate excited state relaxation.

$$\frac{\partial N[t]}{\partial t} = -k_1 \cdot N[t] - k_2 \cdot N[t]^2 - k_3 \cdot N[t]^3 \qquad (3)$$

Equation 3 includes terms for first order (trap-mediated), bimolecular, and third order (Auger) processes. Trap-mediated recombination is a two-step process whereby a mobile carrier is immobilized at a lower energy state (trap) and then, in a second step, recombines with an oppositely charged carrier.[57-59] When carrier excitation densities are in excess of traps the concentration of trapped carriers is nearly constant and thus the mechanism follows pseudo-first-order kinetics.[59-60] Bimolecular recombination is second-order and commonly describes the process of an electron and hole radiatively recombining across the bandgap. Third-order Auger recombination occurs when two carriers (an electron and hole) recombine and the energy is transferred to a third carrier. If the third carrier is an electron, the gained energy will push it higher into the conduction band. If instead the third carrier is a hole, the gained energy will push it deeper into the valence band.[57-58, 61] Illustrations of first, second and third order recombination mechanisms are shown in Figure 1.5. Recombination kinetics of different LHP species are discussed in Chapters 2 and 3.

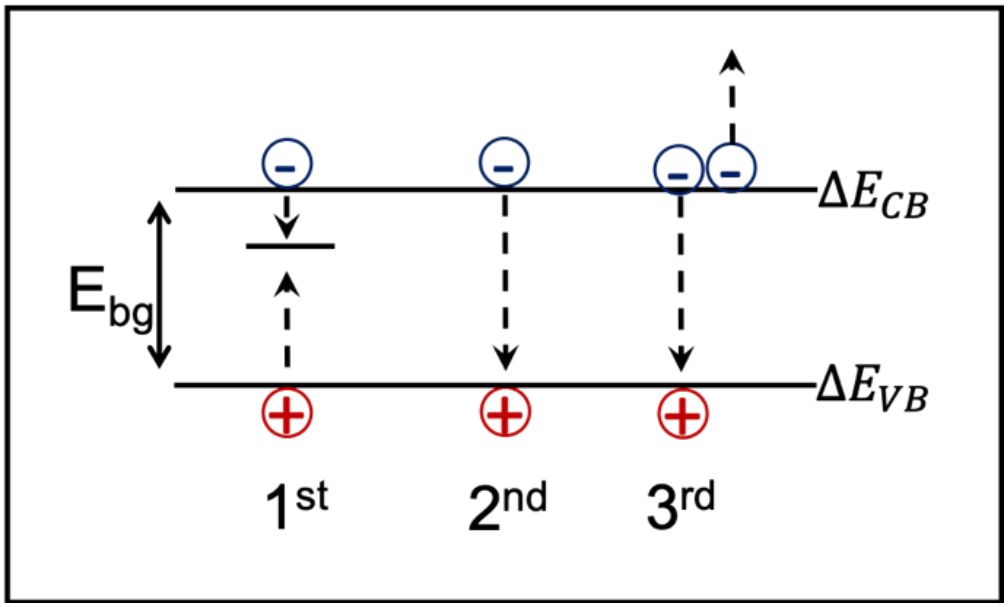

Figure 1.5. Carrier recombination. A diagram illustrating three types of mechanisms by which carriers recombine. From left to right: trap-mediated recombination is a two-step process which follows pseudo-first-order kinetics. Bimolecular recombination is second order and typically involves an electron and hole recombining radiatively across the bandgap. Auger recombination is third order and involves two carriers recombining and transferring the resultant energy to a third carrier.

Spatially Overlapped Imaging. Spatially overlapped pump-probe images are collected by raster scanning (either by using a piezoelectric x,y stage or galvanometer mirrors) spatially overlapped pump and probe beams at a fixed temporal delay. Spatial resolution of the resulting images is determined by the product of the pump and probe point spread functions (Figure 1.6). The distinct fringe pattern shown in Figure 1.4(B) is a consequence of Fabry-Perot interference of the probe light in the cavity formed between the air-perovskite interface and the perovskite-glass interface. Spatially overlapped images collected at increasing pump-probe time delays can be used to build a spatiotemporal map of the excited state across individual domains.

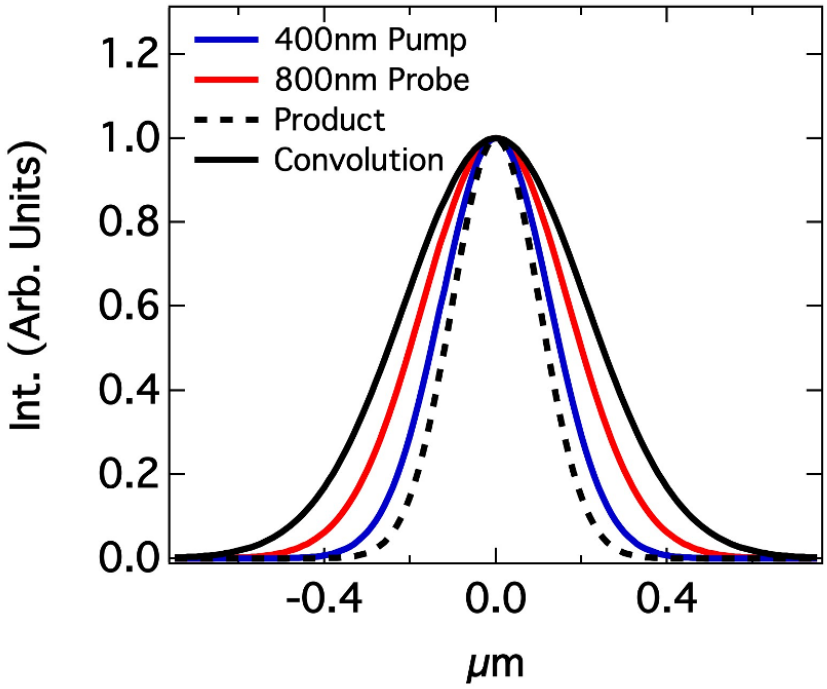

Figure 1.6. Diagram of the product and convolution of two Gaussian point spread functions. The product (black dashed line) of a 400 nm probe point spread function (blue) and an 800 nm probe point spread function (red) will result in spatial response with a reduced width relative to the pump or probe. Comparatively, a convolution (black solid line) of the two Gaussian point spread functions produces a spatial profile that is broadened relative to either the pump or the probe.

Spatially Separated Imaging. Spatially separated pump-probe images are used to determine the rate at which photoexcited charge carriers move through a material. Images are collected by spatially scanning the probe beam over the fixed pump volume at a series of delay times using galvanometer mirrors. Typically, profiles of the time dependent images are obtained by integrating the spatially separated images along either axes (vertical or horizontal). The resulting profiles represent a double convolution of the pump point spread function, the diffusion equation ($exp[-r^2/(4\ D_c\ t)]/\sqrt{4\ \pi\ D_c\ t}$), and the probe point spread function. In the limit that the pump and probe point spread functions

are both Gaussian shaped, each profile can be fit with a Gaussian distribution to obtain a delay-dependent full width at half maximum (FWHM), given by Equation 4.

$$\beta(\Delta t) = \sqrt{\beta(t_0)^2 + 16\ln(2)\, D_c \cdot (\Delta t - t_0)} \qquad (4)$$

where $\beta(t_0)^2$ is the square of the FWHM of the normalized excited state distribution profile when $\Delta t = 0ps$ and D_c is the ambipolar diffusion constant. Under conditions of diffusive motion, a plot of $\Delta\beta^2 = \beta(\Delta t)^2 - \beta(t0)^2$ versus Δt produces a linear trend and the slope is proportional to the diffusion constant D_c of the material. The diffusion coefficient (D) is proportional to the more commonly used parameterization of transport, mobility (μ), by the Einstein equation ($D = \frac{\mu k_B T}{q}$).

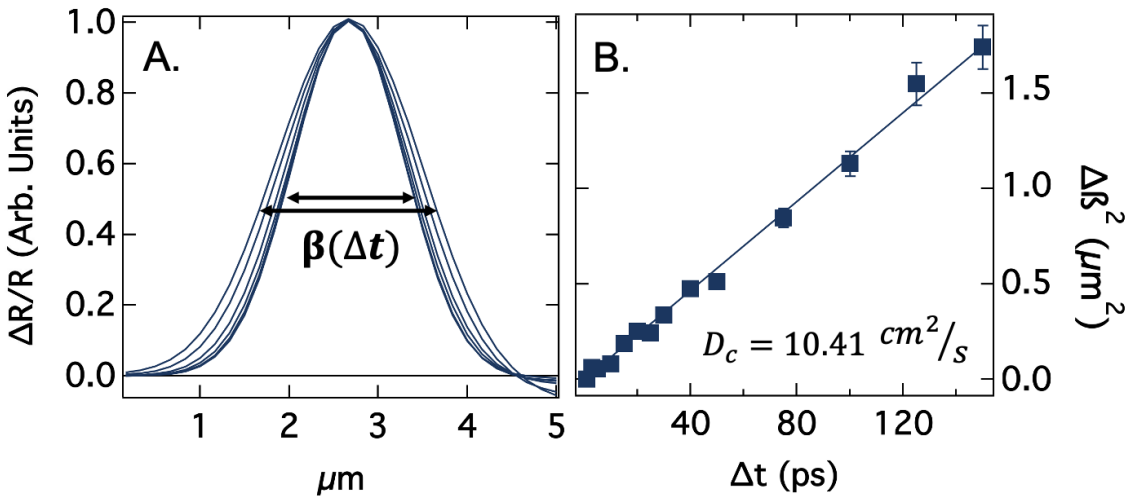

Figure 1.7. Measuring diffusivity coefficients. (A) Excited state carrier distribution profiles obtained from spatially separated images collected at increasing time delays. Panel (A) illustrates the time dependent change in FWHM ($\Delta\beta^2$) associated with the spatially evolving carrier distribution. Panel (B) shows a plot of $\Delta\beta^2$ vs. Δt. The slope of the fit line is proportional to the diffusion coefficient.

As researchers try to better understand charge transport in novel materials, particularly those fabricated by solution processing techniques, pump-probe microscopy has become an increasingly important tool for measuring excited state transport. Owing to its intrinsically high spatial resolution, pump-probe microscopy is advantageous over the multitude of other methods capable of measuring carrier transport because it has the capability to resolve structural heterogeneities.[62] However, the method for extracting diffusivities described above, which is nearly universal practice, cannot accurately treat non-Gaussian point spread functions. Beam aberrations due to the sample or imaging optics, which cause the point spread function to deviate from Gaussian, can lead to incorrectly measured diffusion coefficients. Therefore, to circumvent the limitations of a Gaussian fitting regime, we developed a new approach for analysis of spatially separated images which uses a numerical convolution of the Green's function solution to the diffusion equation with the experimentally determined point spread function. Our aim in developing this technique is to advance the field of ultrafast microscopy by providing a more robust method for determining diffusion coefficients from transport data. Our numerical convolution fit method is discussed in detail in Chapter 5.

CHAPTER TWO

ULTRAFAST EXCITED-STATE TRANSPORT AND DECAY DYNAMICS IN CESIUM LEAD MIXED HALIDE PEROVSKITES

Contributions of Authors and Co-Authors

Manuscript in Chapter 2

Author: Casey L. Kennedy (Hickey)

Contributions: Synthesized and characterized all samples. Collected and analyzed all ultrafast microscopy data. Assisted in writing and editing the manuscript.

Author: Andrew H. Hill

Contributions: Provided valuable feedback on early drafts of the manuscript.

Author: Eric S. Massaro

Contributions: Provided valuable feedback on early drafts of the manuscript.

Author: Erik M. Grumstrup

Contributions: Assisted with analysis and editing of the manuscript for final submission.

Manuscript Information

Casey L. Kennedy, Andrew H. Hill, Eric S. Massaro, Erik M. Grumstrup

ACS Energy Letters

Status of Manuscript:
____Prepared for submission to a peer-reviewed journal
____ Officially submitted to a peer-review journal
____ Accepted by a peer-reviewed journal
_X__ Published in a peer-reviewed journal

ACS Publications
Issue: 7
DOI: 10.1021/acsenergylett.7b00257

2.1 Introduction

The recent resurgence of research interest in lead halide perovskites has revealed a promising array of photo-physical properties and inspired the development of high-performance photovoltaic cells, light-emitting diodes, and laser technologies.[63] While photoconversion efficiencies greater than 22% have been demonstrated for hybrid organic-inorganic perovskites (HOIPs),[64] the materials suffer from thermal and chemical instability. One route toward improving material stability is by substitution of the volatile organic moiety with a cesium cation.[65] Like the HOIP analogues, nanocrystal-line $CsPbX_3$ perovskites exhibit favorable photophysical properties including bright photoluminescence and a tunable band gap through the visible spectrum.[66-67] In the bulk, $CsPbI_3$ forms a non-perovskite insulator at room temperature. However, partial substitution of I for Br results in a mixed halide perovskite that is compositionally robust with respect to both heat and humidity and shows no evidence of halide migration.[65, 68-69] Computational studies suggest that charge transport and optical properties are unaffected upon exchange of the organic moiety with an inorganic Cs cation;[70] however, outside of a few spectroscopic studies of nanocrystals, there is little work investigating the ultrafast photophysics of the Cs-based perovskites.[71-72]

In this Letter, we report measurements of both recombination dynamics and transport properties of individual $CsPbI_2Br$ microcrystals using ultrafast pump-probe microscopy. The high spatial resolution of the technique provides a direct probe of the spatial and temporal relaxation dynamics in individual domains. Our results show that in contrast to methylammonium lead tri-iodide ($MAPbI_3$) perovskites, which exhibit

bimolecular recombination at higher excitation densities, Auger recombination is the dominant nonlinear recombination mechanism in $CsPbI_2Br$. In addition, by directly imaging the spatial evolution of the photogenerated excited state, we find ambipolar mobilities that are nearly an order of magnitude lower than those of $MAPbI_3$ at comparable pump excitation densities.

2.2 Results and Discussion

Low-coverage thin-films were prepared by spin-casting a precursor solution of 0.4 M CsBr and 0.4 M PbI_2 in DMSO onto a glass substrate. The films were subsequently annealed in a saturated DMSO atmosphere on a 65 °C hot plate for 1 h. While morphological variation exists on the film, our spectroscopic studies focused on the faceted, crystalline structures shown in the widefield scanning electron microscopy (SEM) image shown in Figure 2.1(A). Panel B of Figure 2.1 shows the absorption spectrum of a single $CsPbI_2Br$ domain collected with an optical microscope. A fit to the spectrum using the Elliot model[55, 73-74] convolved with a hyperbolic secant line shape (full width at half-maximum of 76.5 ± 1.0 meV) recovers a band gap energy of 1.97 ± 0.01 eV and an exciton binding energy of 10.0 ± 0.5 meV. The fit deviates from the spectrum at higher energies because of band nonparabolicity and higher lying states which are not included in the model. We note that because the absorption spectrum reflects only an induced polarization, the binding energy recovered from the fit does not necessarily reflect the binding energy of an incoherent exciton population.[75-76] Also presented in Figure 2.1(B) is the (ensemble) steady-state photoluminescence spectrum, collected after photoexcitation at 2.50 eV.

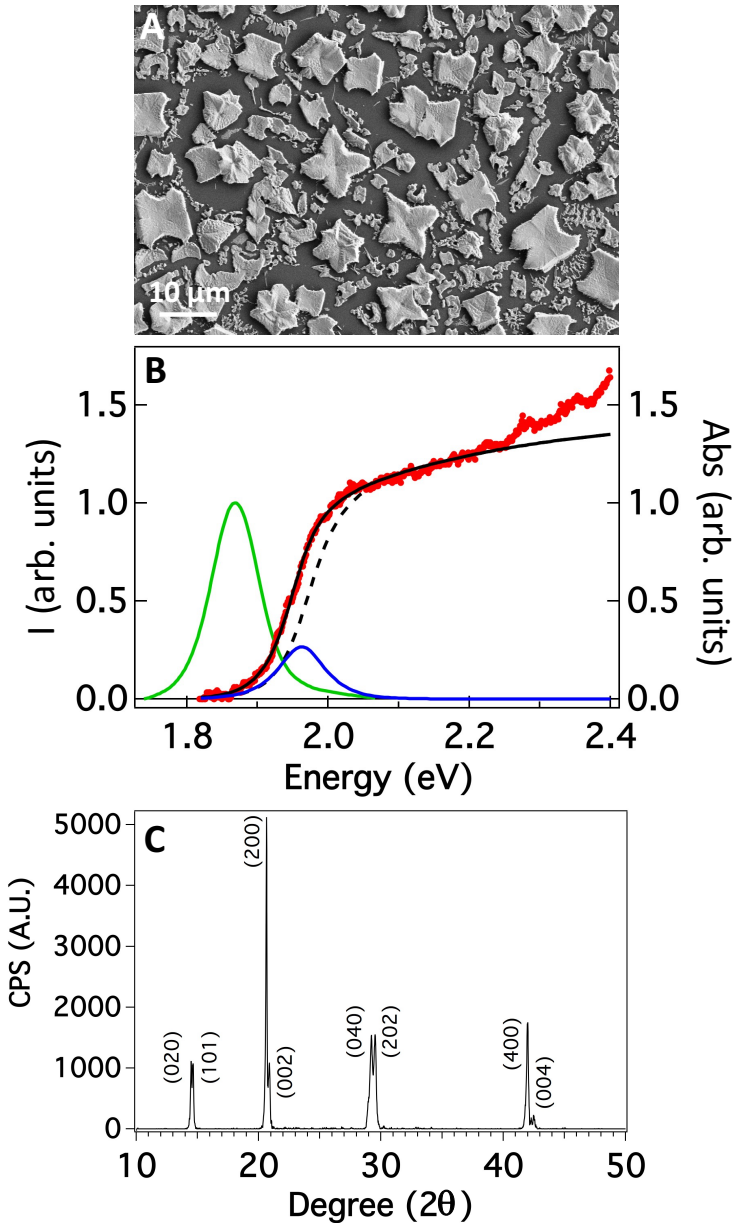

Figure 2.1. $CsPbI_2Br$ perovskite thin films. (A) SEM image of the low-coverage film produced via solvent annealing. (B) Absorption (red circles) and emission (green solid line) spectra of perovskite thin films. The emission spectrum is peaked at 1.87 eV. The black solid line shows a fit of the experimental absorption spectrum using the Elliot model comprising excitonic (blue solid line) and continuum (black dashed line) contributions. (C) Powder X-ray diffraction (XRD) pattern showing highly crystalline thin films with orthorhombic geometry.

The XRD pattern of the thin film is shown in Figure 2.1(C). The diffraction peaks are assigned based on a comparison with the published pattern for $CsPbBr_3$ (see Table A1 of Appendix A), accounting for an expected volume increase in the unit cell associated with substitution of the relatively larger iodine ions.[77] The orthorhombic unit cell has lattice parameters a = 8.60 Å, b = 12.21 Å, and c = 8.50 Å, which correspond to a ~ 4% increase along all three unit cell axes relative to $CsPbBr_3$.

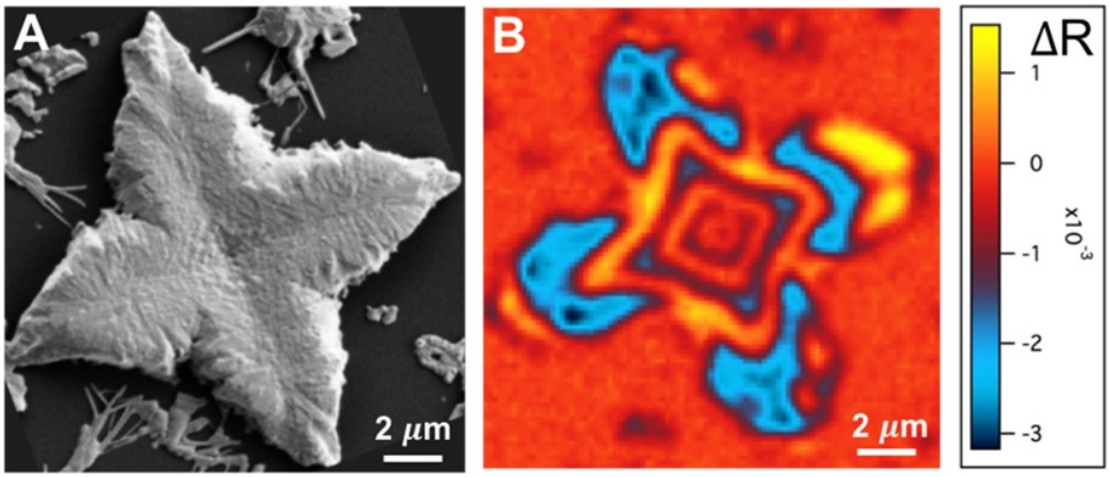

Figure 2.2. Faceted $CsPbI_2Br$ perovskite domain. (A) SEM image and (B) the corresponding transient reflectivity image collected at a pump−probe delay of 0 ps. The distinct fringe pattern reflects shifting of probe beam Fabry−Perot resonances upon photoexcitation.

A SEM image of a single $CsPbI_2Br$ domain is shown in Figure 2.2(A). A survey with SEM and atomic force microscopy (AFM, see Figure A2 of Appendix A) shows the domains are, on average, 10 μm in length and increase in thickness from ~0.8 μm at the center to ~1.3 μm along the edges. The morphology of the domain gives rise to the distinct fringe pattern seen in the corresponding transient reflectivity (TR) image shown in Figure 2.2(B). The TR image is collected by scanning the domain beneath spatially and temporally (Δt = 0 ps) overlapped pump (2.25 eV) and probe (1.55 eV) beams (see

Appendix A for instrumentation details). Because the microscope has a spatial resolution of ~350 nm (determined by the product of the pump and probe point spread functions), and the probe energy is well below the band gap energy, the reflected probe intensity is primarily determined by the position of the probe beam Fabry-Perot resonances in the perovskite domain. Photoexcitation causes a transient decrease in the refractive index of the material that is proportional to the excited-state population density, shifting the probe Fabry-Perot mode positions to thicker regions of the domain.[52, 56] As a result the TR response, which reflects the difference between the equilibrium and photoexcited mode position, provides a sensitive probe of the excited-state dynamics.

Figure 2.3 shows representative TR decay dynamics from a second $CsPbI_2Br$ domain. In panel A, we show power-dependent kinetics collected from the circled location on the domain in Figure 2.3(B). The probe energy (1.55 eV) is well below the emission spectrum (peaked at 1.87 eV), so the material response largely stems from pump-induced changes in reflectivity. As shown in the inset of Figure 2.3(A), the initial TR signal amplitude ($-\Delta R0$, $\Delta t = 0$ ps) is linearly proportional to pump fluence over the full range we measured, from 33 to 460 μJ/cm^2. However, at fluences greater than 65 μJ/cm^2, the recombination dynamics become faster, indicating that first-order processes are insufficient to describe the observed kinetics. To model the power-dependent decay kinetics, we used the rate equation given by Equation 1, which includes terms accounting for first-order, bimolecular, and Auger recombination mechanisms.

$$\frac{\partial N[t]}{\partial t} = -k_1 \cdot N[t] - k_2 \cdot N[t]^2 - k_3 \cdot N[t]^3 \qquad (1)$$

Global fits to the power-dependent decay kinetics collected from five individual $CsPbI_2Br$ domains were performed using excitation densities calculated by averaging over the 1/e width of the Gaussian pump pulse and the 1/α absorption depth ($\alpha = 2\ \mu m^{-1}$; see Appendix A). The three shared rate constants were the only fitted parameters. For all five domains, the second-order rate constant, k_2, was found to have negligible amplitude (zero within error, see Table A2 of Appendix A), suggesting that the bimolecular, direct recombination mechanism is not relevant in the decay dynamics of these materials.

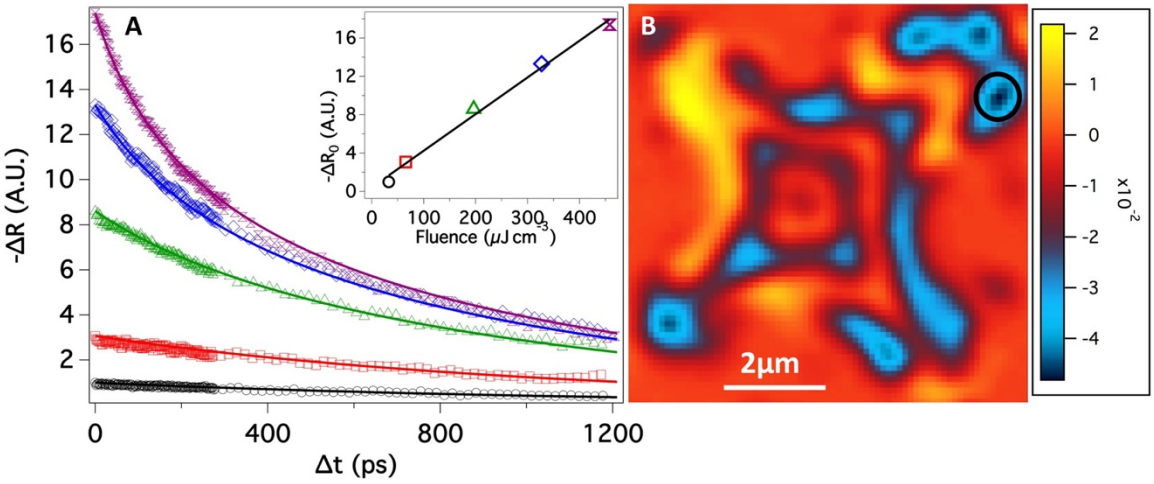

Figure 2.3. Power-dependent TR kinetics of a single $CsPbI_2Br$ domain. (A) The circle, square, triangle, diamond, and hourglass markers correspond to kinetics data collected at increasing fluences. The kinetics traces are scaled to the (normalized) lowest fluence kinetics trace. Solid lines correspond to fits of the data to the first- and third-order terms in Eq. 1. The inset shows that $-\Delta R$ at $\Delta t = 0$ ps scales linearly with pump fluence, i.e., the initial signal amplitude doubles if the pump power is doubled. Excitation densities were calculated based on a measured absorption coefficient (see the Supporting Information) of 2 μm^{-1} and range from 1.25×10^{18} cm^{-3} (33 $\mu J/cm^2$) to 1.75×10^{19} cm^{-3} (460 $\mu J/ cm^2$). A global fit to the kinetics in panel A yielded $k_1 = 8.65\ (\pm 0.14) \times 10^8\ s^{-1}$ and an Auger coefficient (k_3) of $5.6\ (\pm 0.1) \times 10^{-30}$ cm^6/s. (B) TR image of the domain from which the kinetics shown in panel A were collected, with a black circle indicating the location of measurement.

The kinetics shown in Figure 2.3 suggest that recombination in Cs-based perovskites differs substantially from that of the $MAPbI_3$ perovskite under typical

excitation densities. In $MAPbI_3$, the dominant recombination mechanism in the absence of surface recombination is a second-order, direct process where an electron and hole recombine across the band gap.[78-79] First order (Shockley−Read−Hall, SRH) lifetimes in $MAPbI_3$ are on the order of 10^1−10^2 ns.[73, 80] In contrast, the five individual domains we investigated exhibited first-order kinetics with lifetimes between 0.98 and 1.87 ns. Time correlated single photon counting (TCSPC, see Appendix A) performed on a $CsPbI_2Br$ thin film (2.25 eV excitation, 1.87 eV detection) shows a biexponential photoluminescence decay with a short lifetime of 444 ± 31 ps (0.75) and a long lifetime of 6.16 ± 0.13 ns (0.25). Although it is difficult to compare ensemble and single structure measurements, the close correspondence between the majority (fast) component in TR and TCSPC is consistent with a low PL quantum yield, suggesting that the ∼1 ns decay lifetime of the $CsPbI_2Br$ domains is largely determined by trap-mediated nonradiative (SRH) recombination.

Kinetics collected on each of the five domains at higher excitation densities showed modest Auger coefficients between 3.3×10^{-30} and 1.5×10^{-28} cm^6/s. This range of Auger coefficients is smaller than, but still comparable to those found in Cs-based perovskite nanocrystals (3×10^{-28} to $4 \times 10^{-27} cm^6/s$),[71] perhaps reflecting a stronger Coulomb interaction in quantum-confined particles. The observation that Auger recombination dominates over radiative recombination in $CsPbI_2Br$ is somewhat surprising, given that Auger proceeds via a three-particle interaction, whereas radiative recombination is a two-particle (electron and hole) process. We note, however, that the rapid first-order SRH decay may dominate bimolecular recombination in these materials

at lower fluences, and the Auger term becomes relevant only because of its n^3 scaling. Furthermore, the probability of each decay pathway is subject to both energy and momentum conservation, restrictions which may favor the Auger process depending on the material band structure and whether the Auger process is trap-mediated.[26, 61, 81] Finally, we note that at low temperatures (<160 K), $MAPbI_3$ adopts an orthorhombic phase like room-temperature $CsPbI_2Br$. Under these low-temperature (orthorhombic phase) conditions, the decay dynamics of $MAPbI_3$ are faster than those collected at room temperature, with Auger recombination dominating over second-order processes.[57, 82] Taken together, our results indicate that the dominant recombination mechanisms change significantly upon substitution of the A-site cation in lead halide perovskites, supporting conclusions that cation reorientation may play an important role in the carrier dynamics of $MAPbI_3$.[83-84] However, further comparative studies of the recombination dynamics in HOIPs and all-inorganic perovskites, particularly those that resolve the full transient spectra, will be valuable for refining an understanding of recombination in this class of materials.

We next turn to characterizing the transport properties of individual $CsPbI_2Br$ perovskite domains. To do so, we directly image the spatial evolution of the excited state using spatially separated pump-probe microscopy. For these measurements, the pump beam is positioned at a fixed location on an individual $CsPbI_2Br$ domain while the probe beam is spatially scanned over the field of view at a series of delay times. The resultant Δt-dependent images reflect the spatial and temporal evolution of the excited state. Figure 2.4(A) shows a representative set of spatially separated images, collected from an

individual perovskite domain at pump-probe delay times of 0, 200, and 800ps. The profiles shown in Figure 2.4(B) (obtained by integrating the images along the horizontal axis, see Appendix A) increase in width because of the diffusive motion of the excited states from a region of high excitation density to the surrounding low-density region. A fit to each profile with a Gaussian distribution (solid line, Figure 2.4(B)) provides a delay-dependent full width at half-maximum (fwhm), given by Equation 2:

$$\beta(\Delta t) = \sqrt{\beta(t_0)^2 + 16\ln(2)\, D_c \cdot (\Delta t - t_0)} \qquad (2)$$

where $\beta(t0)^2$ is the square of the fwhm of the normalized excited-state distribution profile when $\Delta t = 0$ ps and D_c is the ambipolar diffusion constant.[85]

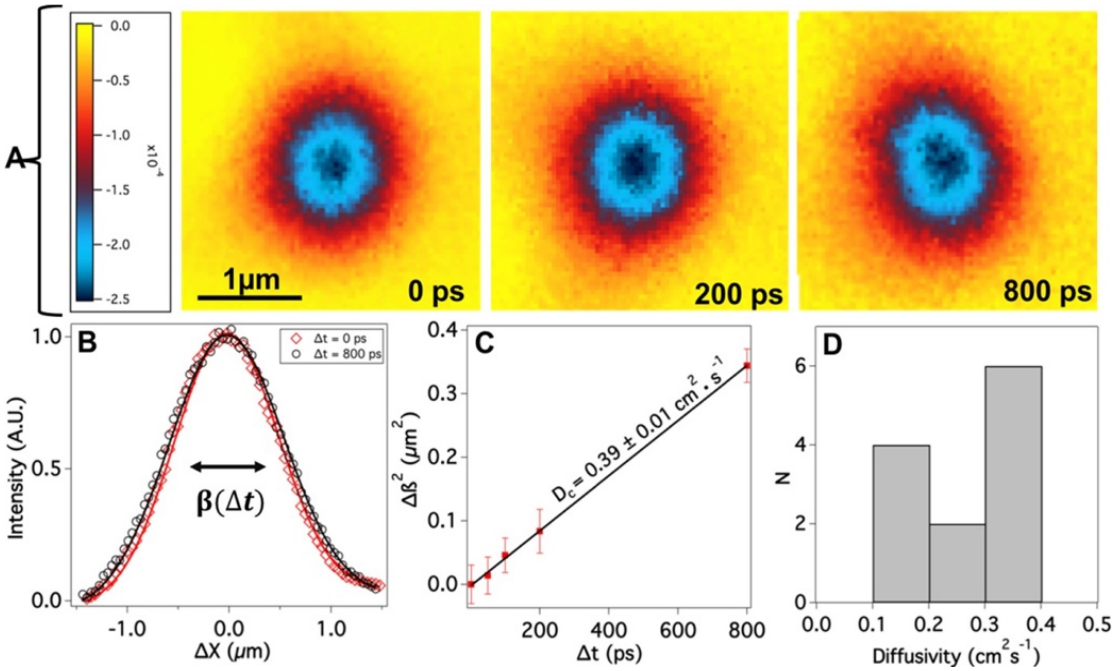

Figure 2.4. Spatially separated TR data for determination of $CsPbI_2Br$ diffusion constant. (A) Spatially separated TR images at Δt = 0, 200, and 800 ps. (B) Excited-state distribution profiles for Δt = 0 ps (red diamonds) and Δt = 800 ps (black circles). The solid lines show Gaussian fits to the data. (C) Plot of $\Delta\beta^2$ vs Δt: slope is proportional to the diffusion constant, and error bars correspond to 90% confidence intervals. (D) Histogram of diffusion constants measured for 12 individual domains.

Under conditions of diffusive motion, a plot of $\Delta\beta^2 = \beta(\Delta t)^2 - \beta(t0)^2$ versus Δt produces a linear trend, whose slope is proportional to the diffusion constant (D_c) of the material (Figure 2.4(C)). For the data presented in panels A and B, the diffusion constant recovered is 0.39 cm^2/s, which can be related to the more commonly referenced ambipolar charge carrier mobility through the Einstein relation ($\mu_A = D_c q/kT$, 15 cm^2/Vs). Measurements performed on 11 additional individual domains revealed similar values for the diffusion constants. Figure 2.4(D) summarizes the distribution of D_c values found, ranging between 0.13 and 0.39 cm^2/s (5 and 15 cm^2/Vs). All measurements were performed in a regime where Auger recombination does not contribute to the observed recombination kinetics, i.e., at fluences below 65 $\mu J/cm^2$. We note that while it is not clear to what extent the overall signal intensity in our measurements arises from excitons versus free carriers, exciton diffusivity is expected to be closely comparable to ambipolar carrier diffusion under our experimental conditions.[86]

It is surprising that the ambipolar mobility of $CsPbI_2Br$ is significantly lower than in, for example $MAPbI_3$,[85] particularly in light of recent results that suggest the MA moieties rearrange around charge carriers to form large polarons.[84] Under conventional theories of carrier transport in semiconductors, polaron formation should strongly reduce mobility.[54] Because Cs^+ does not form a dipole, carriers in $CsPbI_2Br$ ought to exhibit higher mobilities, in contrast to our results. While we are not aware of any reports of carrier mobilities in the mixed halide, bulk $CsPbI_2Br$ perovskite, electron and hole mobilities derived from photoconductivity measurements of $CsPbBr_3$ were reported to be over 1000 cm^2/V s, a value nearly 2 orders of magnitude higher than what we find.[77] One

possible reason for the apparent reduction in mobility is the difference in halide composition. A comparison of mixed halide formamidinium lead halide perovskites ($FAPbBr_yI_{(3-y)}$) using terahertz photoconductivity showed decreased mobility for the mixed halide case (y = 0.6−1.5) relative to neat samples (y = 3 or 0).[26] While similar effects may be relevant to the Cs-based perovskites, only a 5- to 10-fold decrease in mobility was observed in the mixed halide formamidinium perovskites, suggesting other factors are likely at play. Scattering from grain boundaries and twin boundaries in the microcrystals may also contribute to the unexpectedly low mobility. Polarized light microscopy of the films we studied (See Appendix A) shows the microcrystals are birefringent and composed of several well-ordered grains, arranged symmetrically around the center of each microcrystal. While we cannot completely rule out scattering due to the domain interfaces, we expect that if the diffusing excited state encountered a grain boundary with significantly reduced mobility, subdiffusive behavior would be observed, i.e., plots like that shown in Figure 2.4(C) would exhibit nonlinear behavior. Our data showed no indication that the diffusing excited states encountered low-mobility domain boundaries during their spatial evolution. Nevertheless, to confidently establish whether grain and twin boundaries impede transport, we are currently working to fabricate larger single crystal domains (10 μm × 10 μm) so that diffusion dynamics can be imaged far from any lattice defects. A final possible cause of the reduced mobility in $CsPbBrI_2$ is interaction of charge carriers with trap sites in the lattice. The transient kinetics collected with TR and TCSPC suggest that recombination proceeds primarily via a trap-mediated process. Carrier trapping can impact transport as well. If either electrons or holes are

trapped in the lattice (and thus exhibit lower mobility than free carriers), space charge effects will reduce the overall ambipolar transport of the photogenerated carrier cloud depending on the depth of the trap sites and the intrinsic mobility of the carriers.[87-88] While we have recently shown that trapping plays a minimal role in $MAPbI_3$ transport because of the high static dielectric and the short intrinsic carrier scattering time,[85] there may be significant differences in material properties, e.g., the static dielectric constant, that enhance the impact of trap sites in Cs-based perovskite carrier transport (and recombination) relative to the organic-inorganic analogues. Temperature dependent transport measurements should provide further insight into the role of trap sites and their impact on carrier mobility in these materials.

2.3 Conclusion

In summary, we have characterized the ultrafast recombination dynamics and excited-state diffusion in individual $CsPbI_2Br$ perovskite microcrystals using pump-probe microscopy. We find that trap-mediated (first-order) recombination dominates at low fluences, with Auger recombination becoming increasingly important as the excitation density increases. By direct imaging of the excited-state spatial evolution, we find an average diffusivity of $D_c = 0.27$ cm^2/s, nearly a factor of 10 lower than in $MAPbI_3$. The distinct differences in recombination dynamics and mobilities highlight the need for further comparative studies of cesium lead halide perovskites and organic-inorganic hybrid perovskites to establish a fundamental understanding of the structural and chemical parameters that impact perovskite photophysical properties.

CHAPTER THREE

SCREENING LINKS TRANSPORT AND RECOMBINATION MECHANISMS IN LEAD HALIDE PEROVSKITES

Contributions of Authors and Co-Authors

Manuscript in Chapter 3

Author: Casey L. Kennedy (Hickey)

Contributions: Synthesized and characterized $CsPbBr_3$ and $MAPbBr_3$ samples. Collected and analyzed ultrafast microscopy data on $CsPbBr_3$ and $MAPbBr_3$ samples. Assisted in writing and editing the manuscript.

Author: Andrew H. Hill

Contributions: Synthesized and characterized $MAPbI_3$ samples. Collected and analyzed ultrafast microscopy data on $MAPbI_3$ samples. Provided valuable feedback on early drafts of the manuscript.

Author: Erik M. Grumstrup

Contributions: Assisted with analysis and editing of the manuscript for final submission.

Manuscript Information

Casey L. Kennedy, Andrew H. Hill, Erik M. Grumstrup

The Journal of Physical Chemistry C

Status of Manuscript:
____Prepared for submission to a peer-reviewed journal
____ Officially submitted to a peer-review journal
____ Accepted by a peer-reviewed journal
_X__ Published in a peer-reviewed journal

ACS Publications
Issue: 123
DOI: 10.1021/acs.jpcc.9b03235

3.1 Introduction

A decade of intense research efforts have established lead halide perovskites (LHPs) as promising candidates for low-cost photovoltaics and other optoelectronic applications. However, the unusual material properties characteristic of LHPs have so far prevented a comprehensive understanding of the photophysical parameters which determine performance in device applications.[89-91] In particular, the roles played by extensive dynamic disorder at room temperature, the unusually low-frequency and highly anharmonic lattice modes, and the extent of polaron formation remain poorly understood, especially with respect to how these phenomena influence band-edge charge carrier transport and recombination at room temperature.[92-93]

In a crystalline material at carrier densities relevant to a photovoltaic device, charged impurity scattering and carrier-phonon scattering impose fundamental limits on the intrinsic charge mobility.[94-95] Scattering processes, either between two charged centers (carrier-carrier or impurity scattering) or between a charge carrier and the surrounding lattice (carrier-phonon scattering), are determined by Coulomb coupling.[53] Therefore, the effective dielectric function that mediates the Coulomb potential is a key parameter influencing transport. It is typical to consider the static dielectric in this context. For example, the well-known Debye screened potential, which accounts for screening of a fixed charge by the polarization of its surroundings, is given by, $V(r) = q\ Exp[-r/\lambda_D]/(4\pi\varepsilon_0\varepsilon_s r)$, with the Debye length $\lambda_D = \sqrt{\varepsilon_0\varepsilon_s kT/nq^2}$, n the carrier density, kT the thermal energy, ε_0 the permittivity of vacuum, and ε_s the relative static dielectric. The Debye screened potential strictly holds only in the low frequency and low

spatial variation limit (small wavevector). However, when these limits cannot be assumed, the full momentum- and frequency-dependent dielectric function, which is *reduced* relative to the static dielectric, must be considered.[96] The frequency-dependent dielectric function can be considered as a sum of low- and high- frequency contributions. In polar semiconductors, the low-frequency contributions arise from lattice polarization as well as (in some cases, like the LHPs[97]) ion mobility, leading to strong screening in the true static limit.[98] In the high frequency limit, electron polarization is the only contribution to screening since nuclear degrees of freedom respond too slowly.

Under conditions of quasiequilibrium transport, such as in an operating solar cell or after photoexcitation with a laser, the question arises as to what the relevant dielectric is that determines screening for the mobile carriers. On one hand, LHPs are a polar semiconductor so it is reasonable to expect lattice polarization to play some role in determining the effective screening length. On the other hand, it is well-established that the lattice modes in LHPs are unusually low frequency for an inorganic semiconductor. For example in $MAPbI_3$, optical phonons are resonant near 1-4 Thz.[99] Thus, vibrational motion is far slower than the characteristic motion of the electrons. An estimate of the thermal charge carrier velocity, ($\mathrm{v}_{th} = \sqrt{\frac{3k_BT}{m^*}}$, $m^* = 0.25\ m_e$ for $MAPbI_3$), is $\mathrm{v}_{th} \approx 2.3 \times 10^7\ {}^{cm}/_{s}$, which yields a characteristic frequency of motion (across a unit cell) of 285 Thz. While a classical argument, the disparity in frequencies between electronic and nuclear degrees of freedom suggests that the low-frequency motion of the lattice may not be entirely effective in its ability to shield the highly mobile charge carriers from other charged centers in the lattice.[100] It is therefore plausible that the mobile charges in the

lattice are instead screened by an effective dielectric that is intermediate between the high and low frequency limits.

To test this hypothesis, we have utilized transient absorption microscopy to directly measure the ambipolar diffusion constants of several LHPs as a function of excitation density. We find the effective dielectric for band-edge mobile charges is a factor of 2-10 lower than previously reported values for the static dielectric in both cesium lead tribromide ($CsPbBr_3$) and methylammonium lead tribromide ($MAPbBr_3$). These findings are corroborated by a study of the power-dependent recombination kinetics, which finds that nonlinear recombination onsets earlier and scales more strongly with excitation density in the lead bromide perovskites relative to $MAPbI_3$. Together, these results indicate that the relevant dielectric for photogenerated charge carriers is an intermediate value between the low and high frequency limits, and that screening is strongly influenced by halide composition via differences in electronic polarizability.

3.2 Methods

We employ a simple solution processing technique, which utilizes spin-coating and solvent annealing, to produce low-coverage lead halide perovskite thin-films (Appendix B). This approach produces well-resolved crystalline domains, but like all solution-processing techniques, intrinsically introduces structural heterogeneity (polycrystallinity, grain boundaries, etc.) into the resulting thin film. Therefore, in an effort to probe properties representative of the bulk, we utilize ultrafast pump-probe microscopy (PPM) to directly measure the ambipolar (both electron and hole) diffusion

and decay dynamics in individual microcrystalline domains. Our homebuilt microscope has been described in detail elsewhere.[101]

Photoexcitation by the pump (2.9 eV for $CsPbBr_3$ and 3.1 eV for $MAPbBr_3$) causes a transient decrease in the refractive index of the material at the probe energy of 1.55 eV. The band gaps of $CsPbBr_3$ and $MAPbBr_3$ are ~ 2.37 eV and ~ 2.30 eV, respectively (Appendix B). The measured change in probe reflectivity is proportional to the photogenerated charge carrier density ($-\Delta R \propto n[t]$),[101-102] and is linear with respect to excitation density over the range of excitation densities used in these experiments (Appendix B).

To determine the ambipolar diffusion coefficient, D_A, the spatial evolution of pump-excited charge carriers is directly imaged with a spatially scanned probe beam for a series of increasing pump-probe delay times. Changes in the width of the carrier distribution can be analytically related to the diffusion coefficient of the charge carriers (Appendix B). To determine the dependence of D_A on carrier density, a series of diffusion measurements are taken over a range of excitation fluences. Carrier densities are calculated by averaging over the $1/e^2$ width of the Gaussian pump spot (300nm, measured by imaging a known diameter SiC nanowire and deconvolving the beam diameter) and the $1/\alpha$ absorption depth (α = 9 μm^{-1} at 425 nm for $CsPbBr_3$ and 400 nm for $MAPbBr_3$ (Appendix B)). Power-dependent carrier recombination dynamics were measured by spatially overlapping the pump and probe pulses and collecting transient reflectivity kinetics over an 800 ps delay stage.

3.3 Results and Discussion

We first measure D_A, which reflects the average of a material's electron and hole transport characteristics and is dependent on the mean scattering rate (k_{eff}), and the average effective mass of the charge carriers (m^*),

$$D_A = k_B T / m^* k_{eff} \quad (1)$$

where $k_B T$ is the thermal energy. Figure 3.1 shows the distribution of D_A found for 42 individual $CsPbBr_3$ (Fig. 3.1B) and 13 individual $MAPbBr_3$ (Fig. 3.1D) domains. Although unconfirmed, the variation in measured diffusivities is likely a consequence of differences in the local lattice disorder or trap density. On average, the measured ambipolar diffusivity is similar in $CsPbBr_3$ ($D_A = 1.3\ cm^2/s$) and $MAPbBr_3$ ($D_A = 1.5\ cm^2/s$) perovskites. The diffusion coefficient of an electron or hole ($D_{e/h}$) is related to the mobility through the Einstein relation, $\mu_{e/h} = D_{e/h} q / k_B T$, with q the fundamental charge. The mean scattering rate is a phenomenological term which quantifies the summed scattering rates from various physical phenomena in the material. For this work, we consider $k_{eff} = k_i + k_{cc}$, which describes the effective rate as a sum of intrinsic (phonon and defect) scattering processes (k_i) and a carrier-carrier scattering rate (k_{cc}), which becomes increasingly important as excitation density increases.

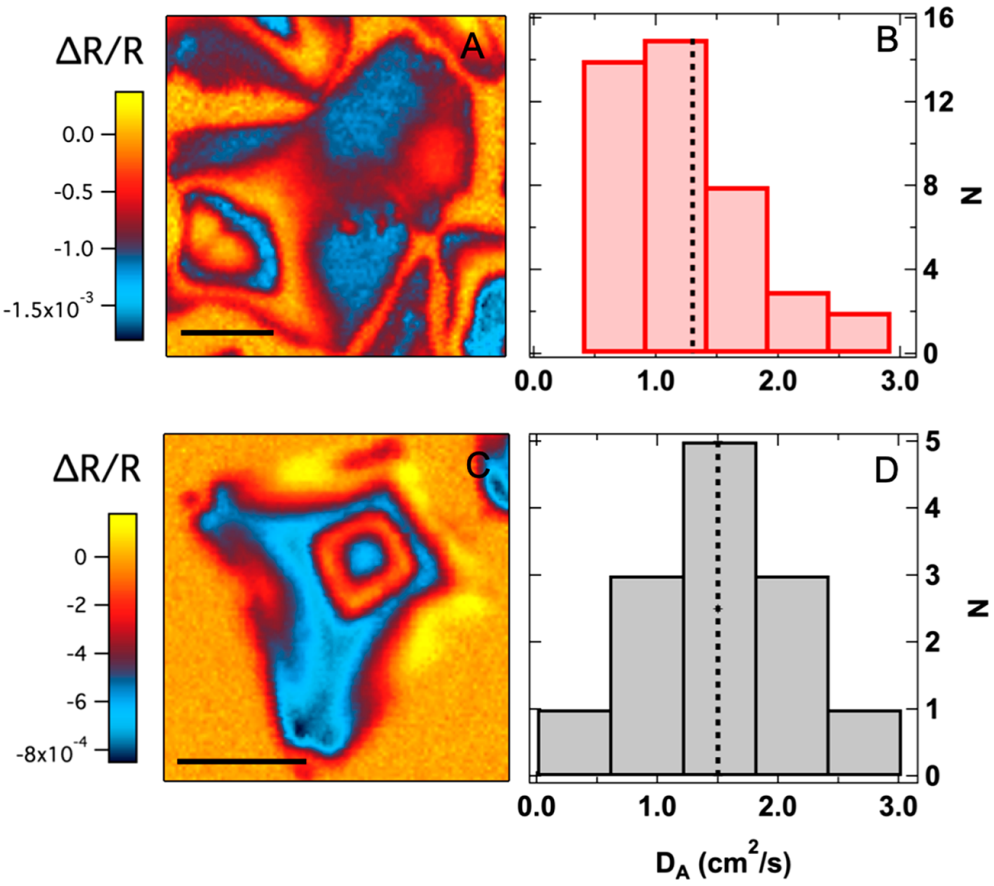

Figure 3.1. Ambipolar diffusivity measured on $CsPbBr_3$ and $MAPbBr_3$ perovskites. Spatially overlapped transient reflectivity images of single $CsPbBr_3$ (A) and $MAPbBr_3$ (C) domains collected at $\Delta t = 1\ ps$. The black scale bars each correspond to a length of 4 µm. Panels (B) and (D) illustrate the distribution of ambipolar diffusion coefficients (D_A) measured on several individual $CsPbBr_3$ and $MAPbBr_3$ domains, respectively. An average diffusivity of $D_A = 1.3\ cm^2/s$ was found for $CsPbBr_3$ (panel B, black line) and $D_A = 1.5\ cm^2/s$ for $MAPbBr_3$ (panel D, black line).

To find the scattering rates from the diffusion measurements, we assume an effective mass that is an average of previously reported values: $m_{e/h} = 2\mu = 0.25$ where $\mu = \frac{m_e m_h}{m_e + m_h}$ is the reduced mass (see Table B1 for values and citations). Note that while this value falls roughly in the middle of the values reported for all three LHPs, deviations

from this average value in specific reports have a negligible influence on our determined parameters within the error of our measurements.

Figures 3.2(A) and 3.2(B) show carrier-carrier scattering rates determined by pump-fluence dependent diffusion measurements collected on individual microcrystals of $CsPbBr_3$ and $MAPbBr_3$. Panel C shows previously reported results collected from $MAPbI_3$ individual domains.[85] Because the intrinsic scattering rate varies from domain to domain, we show only the term arising from carrier-carrier scattering, $k_{cc} = k_{eff} - k_i$. As can be seen in panels A and B, at carrier densities > 10^{18} cm^{-3}, the rates of carrier-carrier scattering increase significantly for both $CsPbBr_3$ and $MAPbBr_3$ perovskites. The carrier-carrier scattering rate can be described by Equation 2:

$$k_{cc} = \left(12\sqrt{2}\pi^{3/2} n^{-1} \varepsilon_r{}^2 \varepsilon_0{}^2 q^{-4} \mu^{1/2} \frac{(k_B T)^{3/2}}{\mathrm{Log}[1+256\pi^2 \varepsilon_r{}^2 \varepsilon_0{}^2 n^{-2/3} q^{-4} k_B{}^2 T^2]}\right)^{-1} \quad (2)$$

where n is the carrier density, ε_r is the relative permittivity, and ε_0 is the vacuum permittivity.[85, 103] Global fits of the carrier-carrier scattering rate (Eq. 2) across two data sets for $CsPbBr_3$ (Fig. 3.2(A)) and three data sets for $MAPbBr_3$ (Fig. 3.2(B)) yield relative dielectric constants of $\varepsilon_r = 11.53 \pm 2.23$ and $\varepsilon_r = 13.01 \pm 1.76$, respectively. The fits are indicated by the black solid lines in panels A and B. For $CsPbBr_3$ (panel A) and $MAPbBr_3$ (panel B), the red dashed lines indicate the predicted behavior using Eq. 2 under the assumption the optical dielectric (ε_∞) screens charge carriers. The blue dashed line indicates the modeled behavior if the static dielectric (ε_s) is the relevant value. In both cases, chosen values are based on measured indices of refraction[100] and ε_s values are taken from previous reports,[14, 19] although we note that there is some variation in reported values for the static dielectric in all three materials. These differences (22 to > 10^3 for

$CsPbBr_3$,[14, 19] 20 to 50 for $MAPbBr_3$,[14, 19, 104] and >70 for $MAPbI_3$[14, 97, 105-106]) are likely due to a number of factors including sample morphology, measurement technique, and the lower frequency limit measured. Regardless, the fit determined values for the effective dielectric in $MAPbBr_3$ and $CsPbBr_3$ fall between the reported optical and static dielectric constants ($\varepsilon_\infty < \varepsilon_r < \varepsilon_s$).

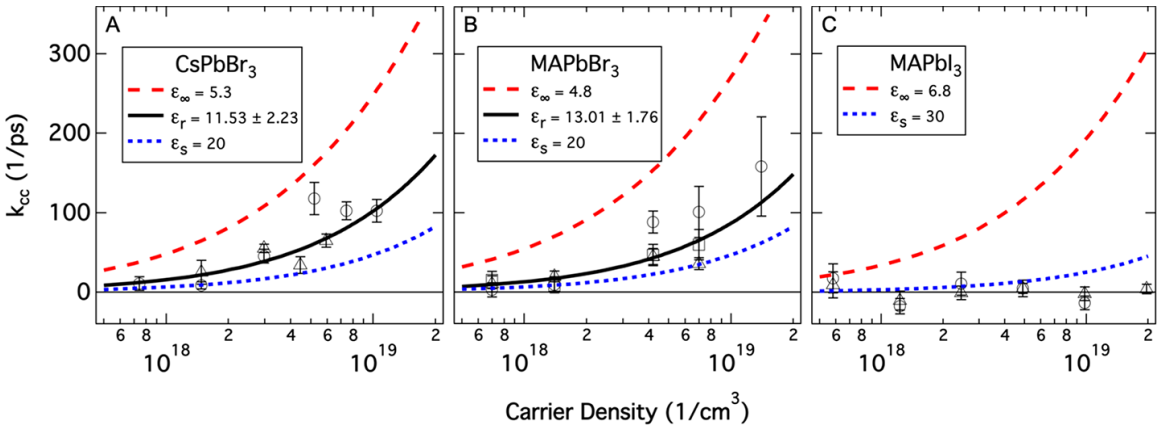

Figure 3.2. Excitation-fluence dependent transport in lead halide perovskites. Panels (A), (B) & (C) show plots of k_{cc} vs carrier density collected over a range of 5×10^{17} to 2×10^{19} for $CsPbBr_3$ (two data sets, black circles and triangles), $MAPbBr_3$ (three data sets, black circles, triangles and squares), and $MAPbI_3$ (two data sets, black circles and triangles), respectively. A global fit of the data sets in panels (A) and (B) to Eq. 2 (solid black traces) yields relative dielectric values of $\varepsilon_r = 11.53 \pm 2.23$ and $\varepsilon_r = 13.01 \pm 1.76$ for $CsPbBr_3$ and $MAPbBr_3$, respectively. The red and blue dashed lines in panels (A) and (B) illustrate Eq. 2 assuming the optical dielectric ($\varepsilon_\infty = 5.3$ for $CsPbbr_3$ and $\varepsilon_\infty = 4.8$ for $MAPbBr_3$) and static dielectric ($\varepsilon_s = 20$ for both $CsPbbr_3$ and $MAPbBr_3$), respectively. The measured k_{cc} rates shown in panel (C) are insensitive to changes in carrier density. The red and blue dashed lines illustrate expected density-dependent diffusion behavior (Eq. 2) assuming the optical ($\varepsilon_\infty = 6.8$) and static dielectric ($\varepsilon_s = 30$), respectively. Error bars shown in (A, B, C) correspond to one standard deviation.

Although greater carrier-carrier scattering with increasing excitation density is apparent in $CsPbBr_3$ and $MAPbBr_3$, the measured diffusion constants for $MAPbI_3$ (panel C) are insensitive to changes in carrier density. This behavior is reproduced by Eq. 2 if $\varepsilon_r > 30$, (blue dashed line, panel C) as we have previously reported.[85] For comparison,

we also show the expected carrier-carrier scattering rate for $MAPbI_3$ assuming an optical dielectric (red dashed line) of $\varepsilon_\infty = 6.8$. While the observed carrier-carrier scattering rate in $MAPbI_3$ clearly does not follow the trend predicted by the optical dielectric, it would not be surprising if the effective dielectric in this system is also an intermediate value between the optical and static limits. As noted above, reported values for the static dielectric in $MAPbI_3$ range between 70 and 130, suggesting this may be true, however our measurements are insensitive to changes in the diffusion coefficient in this regime, so we can only determine a lower limit to ε_r.

It is worth noting at this point three technical limitation that suggest the dielectric values we report are in fact overestimates of the effective dielectric. The first is that at higher excitation densities, nonlinear recombination begins to influence the transient kinetics (see below), producing faster decay in the middle of the photoexcited volume relative to the edges. It is well-known that such effects result in *apparently* larger diffusion coefficients than the true low-fluence value.[85, 107] While it is, in principle, possible to include such effects in a model which simultaneously tracks diffusion and nonlinear recombination, we have found the fits to be of poor quality, with high levels of covariance between the coefficients that parameterize the population decay (which depends on excitation density) and the spatial evolution (which also depends on excitation density). We have therefore elected to analyze the data assuming the simplest possible (density-independent) recombination model. Based on simple continuum models (Appendix B), we estimate the error introduced by this effect is approximately 15% in the measured carrier-carrier scattering rate at the highest fluences. Second, both

recombination and diffusion contribute to a reduction in average carrier density with increasing pump-probe delay time. This decrease in carrier density implies that the mean carrier-carrier scattering rate will also decrease as a function of delay time. To mitigate the effects of the time-dependent excitation density, we measure diffusion only at early delay times (0 - 300 ps). Under these conditions, we estimate the excitation density varies by at most a factor of two, causing a decrease in the determined k_{cc} that lies within experimental uncertainty. The third factor that may depreciate our reported effective dielectric value is that at excitation densities $\gtrsim 5 \times 10^{18}$, deviations from the carrier-carrier scattering model occur because the photogenerated carriers begin to fill states with greater kinetic energy than the band edge states, i.e. the quasi Fermi level is raised. This effect is especially noticeable in Figure 3.2(C) (and in Ref. 51), where the model deviates from the data at high excitation densities. Without detailed calculations that accurately account for the band edge density of states, it is difficult to know the extent to which this factor influences our measurements. However, given the optical response is linear even at densities as high as 5×10^{19} cm^{-3} and that such effects become apparent only at densities near 2×10^{19} cm^{-3} in $MAPbI_3$, we estimate such band filling effects are within the error of our measurement. Regardless, all three contributions will serve to decrease the apparent carrier-carrier scattering rate (that is, they increase the measured diffusion coefficient), and reduce the fit-determined effective dielectric.

The diffusion measurements presented in Fig. 3.1 and Fig. 3.2 strongly suggest that halide composition is of greater importance to carrier transport in lead halide perovskites than cation composition. The two bromide perovskites, $CsPbBr_3$ and

$MAPbBr_3$, have similar low carrier density diffusion coefficients averaged over 42 and 13 individual domains ($D_i \approx 1.3\, cm^2/s$ for $CsPbBr_3$ and $D_i \approx 1.5\, cm^2/s$ for $MAPbBr_3$). Furthermore, the effective dielectric constants for the two lead bromide perovskites are, within error, the same (~11-13). On the other hand, while $MAPbI_3$ has a closely comparable average intrinsic diffusivity of $D_i \approx 1.2\, cm^2/s$[85, 97], the effective dielectric is at least a factor of 2 - 3 larger than its bromide analogue. This difference in dielectric screening is likely a consequence of the increased polarizability of the bound iodide electrons in $MAPbI_3$ relative to those in $CsPbBr_3$ and $MAPbBr_3$.

Like carrier-carrier scattering, nonlinear recombination (2nd order and Auger) mechanisms are also contingent on pairwise interactions between charge carriers in the lattice. It therefore stands to reason that a larger effective dielectric in $MAPbI_3$ relative to the bromide analogues should also be manifest in the recombination dynamics. Specifically, it would be expected that nonlinear recombination in lead iodide perovskites ought to scale less strongly with carrier density because screening is enhanced relative to $MAPbBr_3$ and $CsPbBr_3$. To probe this relationship, we measured decay kinetics in each LHP for a series of increasing excitation fluences. Panels A, B, and C of Figure 3.3 show representative decay kinetics spanning an order of magnitude difference in excitation density for $MAPbBr_3$, $CsPbBr_3$, and $MAPbI_3$, respectively.

Because the magnitude of ΔR is proportional to the population of photoexcited charge carriers, any observed change in ΔR over time reflects the number of carriers that have recombined. At low-carrier densities, the decay in the transient reflection kinetics is due to recombination via first order-processes (trap-mediated). As excitation density is

increased, a difference between low fluence and high fluence kinetics therefore represents the fraction of carriers recombining via nonlinear processes. This fraction of the population (i.e. the fraction of carriers recombining via second and third order processes) is illustrated by the shaded areas in panels A, B and C of Figure 3.3 Over an order of magnitude, the fraction of carriers recombining via higher order processes is much greater ($2.5 - 5\times$) in $MAPbBr_3$ and $CsPbBr_3$ than in $MAPbI_3$. Panel D of Figure 3.3 shows the relative change in ΔR at $\Delta t = 600$ ps over a range of excitation densities that bridge the transition from a power independent regime (with kinetics characterized by linear recombination) to one that is dominated by nonlinear recombination. At the lowest fluences, the kinetics are power independent, and so the difference, $\Delta\Delta R = 0$. However, as pump fluence is increased, nonlinear recombination has a greater relative contribution to the decay kinetics for $MAPbBr_3$ and $CsPbBr_3$ than in $MAPbI_3$. Note that $\Delta\Delta R$ values shown in panel D are normalized to the low-fluence amplitude for each perovskite system at $\Delta t = 600$ ps. Differences in the low-fluence decay rate between $MAPbI_3$ and the bromide analogues have a minimal effect on the carrier dependence of $\Delta\Delta R_{Norm}$ (Appendix B).

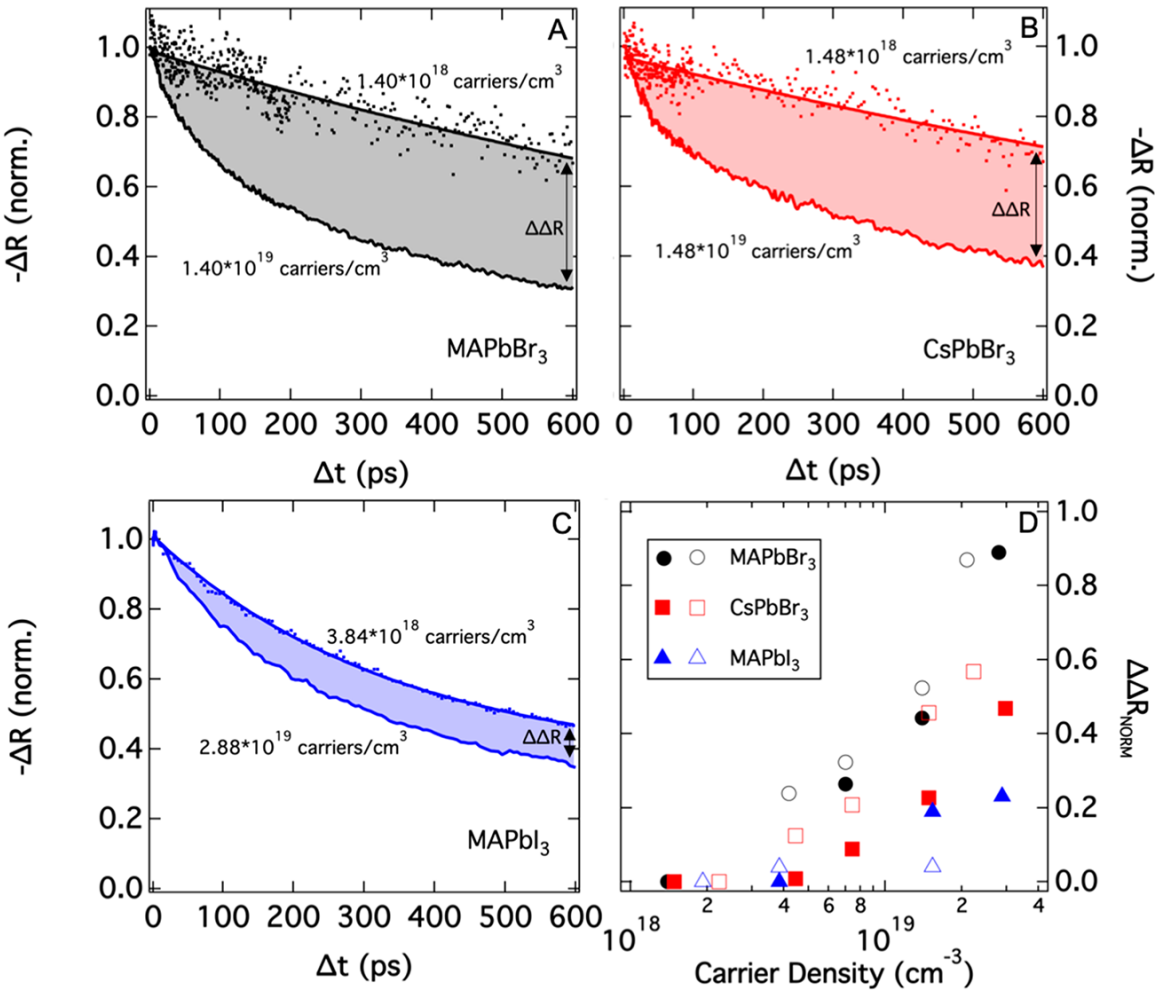

Figure 3.3. Excitation-fluence dependent transient reflectivity kinetics. Panels (A), (B) and (C) show kinetics collected on $MAPbBr_3$, $CsPbBr_3$, and $MAPbI_3$, respectively. The top trace in each panel shows $-\Delta R$ vs Δt collected in a low fluence regime where charge carrier recombination is primarily occurring via first-order, trap mediated processes. The bottom traces show transient reflectivity kinetics taken at high fluences where second- and third-order processes strongly contribute. The shaded area in each panel therefore represent the portion of free-carriers recombining via second and third order processes. Panel (D) shows a plot of $\Delta\Delta R_{NORM}$ vs. carrier density for two data sets collected on each of the perovskite species.

The relatively greater importance of nonlinear recombination in the lead bromide perovskites over $MAPbI_3$ is consistent with the power dependence observed in the diffusion coefficients. For $MAPbI_3$, the large effective dielectric efficiently screens

charge carriers from one another, reducing the effects of carrier-carrier scattering on the diffusion coefficient. This same screening mechanism limits nonlinear recombination. On the other hand, charge carriers in the lead bromide perovskites are less effectively screened. As a result, carrier-carrier interactions are more prevalent at intermediate excitation densities. While it is a simplification of the competing scattering processes and many-body effects occurring in these dynamical materials, a comparison of the Coulomb interaction energy of two point charges ($V(r) = -\frac{q^2}{4\pi\epsilon_r\epsilon_0 r}$) in the bromide and iodide perovskites provides some insight into the correlation between diffusivity and the recombination kinetics. For an effective dielectric of ~ 12 as in $MAPbBr_3$ and $CsPbBr_3$, the pair-wise interaction energy exceeds k_BT when the excitation density rises above ~ 2.3×10^{18} cm^{-3}. For an effective dielectric of ~ 30 as in $MAPbI_3$, the Coulomb energy exceeds k_BT only for excitation densities greater than ~ 3.6×10^{19} cm^{-3}. Comparison of these characteristic carrier densities to the trends observed in Figures 3.2 and 3.3 reveals that the many body effects which limit diffusion or enhance recombination begin to "turn on" only once the respective critical density is reached.

The results described above allow a number of important conclusions to be drawn. First, the value at which the critical density for enhanced recombination is reached in $MAPbBr_3$ is similar to $CsPbBr_3$. The similarity suggests that the A-site cation plays relatively little role in screening charge carriers in the lattice, at least while they occupy band edge states after cooling from their initial photoexcited energies. On the other hand, the significant difference in effective dielectric between $MAPbI_3$ and $MAPbBr_3$ highlights the importance of halide composition in determining screening

efficacy. Our results suggest that bromide LHPs will be far more susceptible to scattering and recombination events near lattice defects and impurities, perhaps explaining the wider range of ambipolar diffusion coefficients measured in $CsPbBr_3$ ($0.4 – 2.67 cm^2/s$, Fig. 3.1(B)) and $MAPbBr_3$ ($0.1 – 2.92 cm^2/s$, Fig. 3.1(D)) compared to $MAPbI_3$ ($0.74 – 1.77 cm^2/s$).[85] Future experiments exploring the correlation between local defect density and measured ambipolar diffusivity will help test this hypothesis. Finally, our observation that charge carriers are more effectively screened in $MAPbI_3$ than in $MAPbBr_3$ and $CsPbBr_3$ has important implications for the design of photovoltaic devices. A screening mechanism which shields Coulomb interactions between two charge carriers will also serve to shield charge carriers from charged impurities or structural defects in the lattice. Therefore, even at carrier densities relevant to photovoltaic devices ($\sim 10^{16} cm^{-3}$), charge transport in $MAPbI_3$ is likely to be less influenced by fluctuations in the local defect density compared to $CsPbBr_3$ or $MAPbBr_3$ perovskites.

3.4 Conclusion

We have presented excitation-fluence dependent transport and decay dynamics data for individual $CsPbBr_3$, $MAPbBr_3$, and $MAPbI_3$ perovskite domains. From the power dependent diffusion coefficients, we find the dielectric constants relevant to photoexcited charge carriers in $CsPbBr_3$ and $MAPbBr_3$ perovskites ($\varepsilon_r = 11.53 \pm 2.23$ for $CsPbBr_3$ and $\varepsilon_r = 13.01 \pm 1.76$ for and $MAPbBr_3$) are intermediate between the high and low frequency limits. These results strongly suggest that low frequency contributions to the static dielectric are ineffective screening mechanisms for the rapidly moving

mobile charges at room temperature. A comparison of density-dependent recombination and transport between $MAPbI_3$ and $MAPbBr_3$ (or equivalently $CsPbBr_3$) highlights the critical role halide chemistry plays in determining the screening ability of the materials. Practically, this suggests charge carriers in $MAPbI_3$ are more tolerant of lattice defects relative to $CsPbBr_3$ and $MAPbBr_3$ perovskites.

CHAPTER FOUR

DIRECT CORRELATION OF CHARGE CARRIER TRANSPORT TO LOCAL CRYSTAL QUALITY IN LEAD HALIDE PEROVSKITES

Contributions of Authors and Co-Authors

Manuscript in Chapter 4

Author: Casey L. Hickey

Contributions: Synthesized and characterized all samples. Collected and analyzed all ultrafast microscopy and EBSD data. Assisted in writing and editing the manuscript.

Author: Erik M. Grumstrup

Contributions: Assisted with analysis and editing of the manuscript for final submission.

Manuscript Information

Casey L. Hickey and Erik M. Grumstrup

Nano Letters

Status of Manuscript:
____ Prepared for submission to a peer-reviewed journal
_X_ Officially submitted to a peer-review journal
____ Accepted by a peer-reviewed journal
____ Published in a peer-reviewed journal

Date Submitted: March 24, 2020

4.1 Introduction

Functional materials produced using solution processing techniques offer a compelling route toward the fabrication of low cost, high-performance optoelectronic and electronic devices. While promising, solution processing can intrinsically introduce structural heterogeneities, particularly for cases in which material morphologies are determined by kinetically controlled approaches like spin or drop casting.[108-112] Understanding the impact of such structural heterogeneities on a material's functional properties remains an experimental challenge, even while their importance is increasingly evident. For example, in solution processed organic thin films, variation in excited state response and relaxation rates have been linked to mesoscale structural defects.[20-21] Structural defects introduced during fabrication have been linked to both reduced stability and photoconversion efficiency (PCE) in thin-film lead halide perovskite (LHP) photovoltaics.[46, 108, 113] Another piece of evidence, albeit more circumstantial, can be found with the LHP $CsPbBr_3$, where the range of reported charge carrier mobilities spans more than two orders of magnitude (20 - 4500 cm^2/Vs).[15-18] While some of this variability likely stems from different measurement techniques, sample-to-sample differences cannot be overlooked. In fact, in our own lab, we have observed an order of magnitude difference in the ambipolar diffusion coefficient from grain to grain on a single $CsPbBr_3$ thin-film.[114]

In LHPs, the impact of microscopic structural defects has been probed using a number of experimental approaches. Ensemble and device-level characterization techniques have been used to study the effects of grain boundaries, polycrystallinity, and

chemical modification via sample comparisons and careful modeling.[115-117] However, the macroscopic probe volume of these techniques requires that heterogeneity be treated only in an average way. A number of groups have therefore elected to use microscopic probes of LHP photophysics to provide insight on, for example, charge carrier transport across grain boundaries and grain-to-grain anisotropy in excited state dynamics.[118-120] In general, these works have relied on correlating spectroscopic observables to mesoscopic structural features like grain boundaries, which can be detected in an optical microscope. Similar efforts have utilized micro X-ray diffraction in combination with photoluminescence microscopy to correlate excited state lifetime with structural variation in polycrystalline thin films.[121]

Thus, while it is now well understood that the polycrystallinity of LHP thin films gives rise to variation in excited state functional behavior, knowledge of the specific nanoscale structural factors that influence the functional properties of LHPs is still lacking. Here we utilize electron backscattering diffraction (EBSD), which provides an atomic-level measure of the local crystalline order, along with pump-probe microscopy (PPM) to directly correlate ambipolar charge carrier transport to the local crystal quality on an individual single crystal $CsPbBr_3$ domain. We develop an analysis approach that provides a relative measure of the local crystal quality, and by measuring the diffusion coefficient in those locations, reveal that nanoscale structural defects play a significant role in determining the upper limit of charge transport in $CsPbBr_3$. Importantly, the defects are not the mesoscopic defects (grain boundaries) that have been earlier linked to reduced transport rates, but rather nanoscale lattice defects, likely anisotropic strain or

point defects, that are only detectable using measurement techniques sensitive to the local atomic spacing.

4.2 Results and Discussion

The results we present below were collected on a single $CsPbBr_3$ domain from a low-coverage thin film fabricated on gold coated, quartz substrate. The domain pictured in Figure 4.1, which is approximately 14 μm × 50 μm, is representative of much of the film. A scanning electron micrograph (SEM) shown in panel (a) suggests that the domain has a smooth surface with no obvious structural defects. Panels (b) and (c) show reflectivity (R) and transient reflectivity (ΔR/R) images, respectively, collected on a homebuilt pump-probe microscope. Transient reflectivity images are collected by scanning the spatially overlapped pump (400nm) and probe (800nm) beams at a set pump-probe delay time ($\Delta t = 1\ ps$) and measuring the pump-induced change in probe reflectivity. For the sub-bandgap probe light used here, the ΔR/R intensity is directly proportional to the photoexcited population density ($-\frac{\Delta R}{R} \propto n[t]$).[122] The distinct positive and negative fringes seen in the R and ΔR/R image are a consequence of Fabry-Perot interference of the probe light in the cavity formed by top and bottom interfaces of the $CsPbBr_3$ domain. Photoexcitation causes a change in the material dielectric function, which shifts the mode position. The R image can be interpreted qualitatively in terms of a topological map; thus, the low spatial frequency of the fringes indicates the domain is gently sloped. A rough estimate based on the index of refraction of $CsPbBr_3$ (n ~ 2.3)[114]

indicates that the thickness difference, Δh, between the neighboring maximum and minimum reflectivity (yellow and blue) fringes is ~ 90 nm ($\Delta h = \lambda_{probe}/4n$).[123]

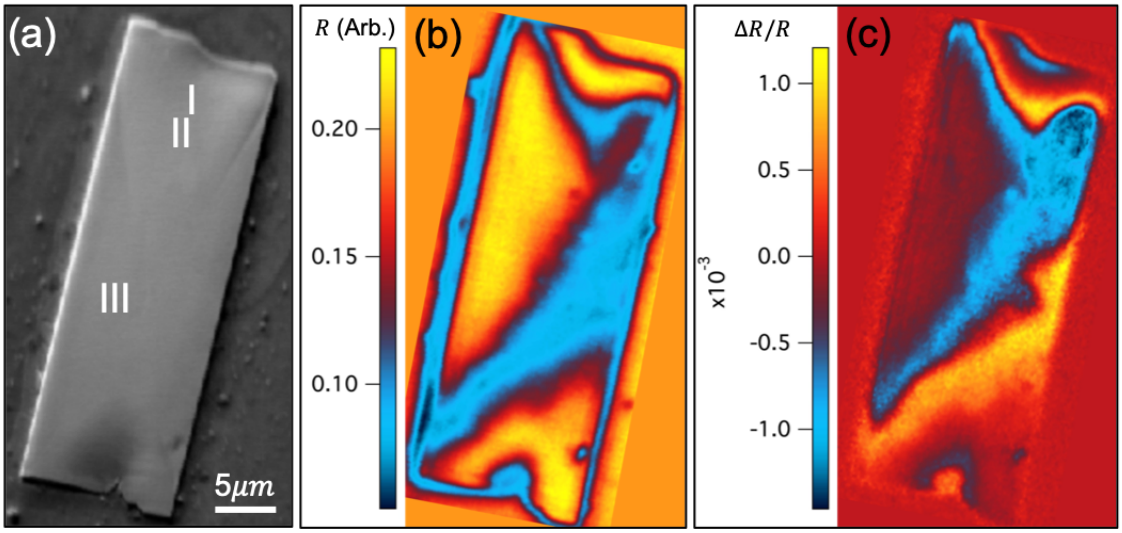

Figure 4.1. High resolution images of a single crystalline $CsPbBr_3$ perovskite. Panel (a) shows a SEM of a single crystalline $CsPbBr_3$ perovskite. Panels (b) and (c) show corresponding spatially overlapped reflectivity and transient reflectivity images, respectively, collected at $\Delta t = 1ps$.

We measured the local ambipolar diffusivity in nine different locations on the domain displayed in Figure 4.1 by spatially scanning the probe beam over the expanding photogenerated charge carrier density. By collecting profiles at a series of increasing pump-probe delay times, the radially averaged diffusion coefficients can be determined. Note that while we measure the ambipolar diffusion coefficient (D) the Einstein relation can be used to express D in terms of the electron and hole mobilities (μ_n/μ_p), $D = \frac{k_B T}{q}\left(\frac{1}{\mu_n} + \frac{1}{\mu_p}\right)^{-1}$. Figure 4.2(a) shows representative profiles from Δt = 1 ps (black) to Δt = 200 ps (blue) at two locations (I and II) marked on Figure 4.1(a). To extract the diffusion coefficient, time-dependent profiles are fit to a numerical convolution of the

experimental point spread function with the Green's function solution to the diffusion equation.[124] Figure 4.2(b) shows a histogram of the diffusion coefficients measured from nine separate locations on the domain. The smallest value measured was 0.60 cm^2/s and the largest was 2.61 cm^2/s. These values compare favorably with the highest reported mobilities of charges in $CsPbBr_3$ perovskites.[15, 18, 114]

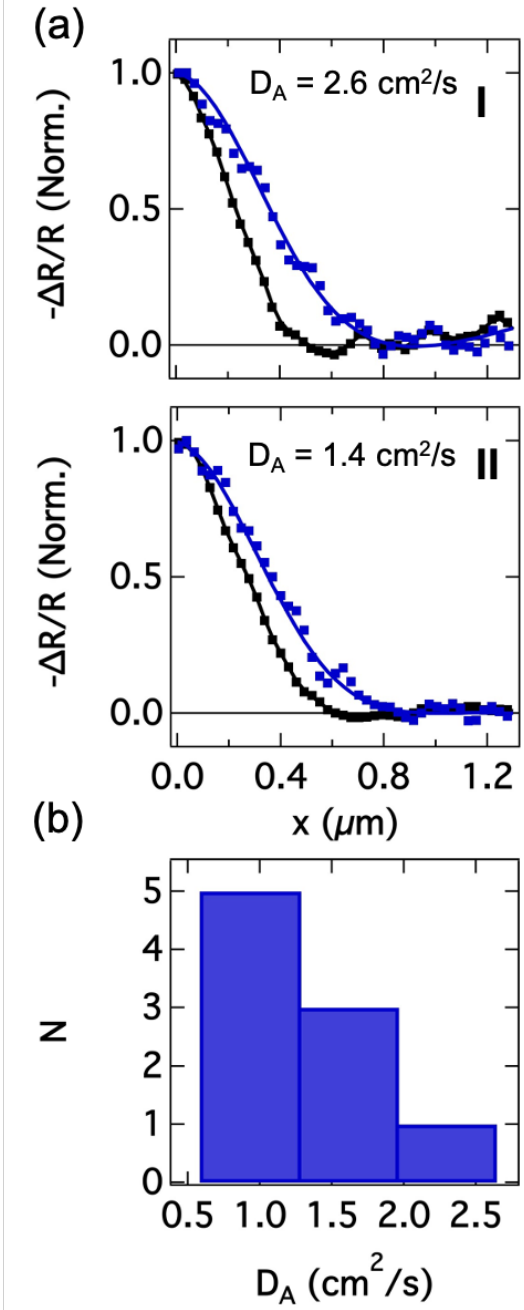

Figure 4.2. Radially averaged diffusivity measurements. Diffusivity measurements were collected from nine separate locations on the domain shown in Figure 4.1. (a) Representative profiles (dots) and fits (solid lines) of spatially separated TR data collected at Δt = 1 ps (black) and Δt = 200 ps (blue) from two of the nine location are shown in plots I and II. (b) Histogram of the nine ambipolar diffusion coefficients (D_A) measured from the domain shown in Figure 4.1.

The wide variation in observed diffusion coefficients suggests that some form of intra-domain heterogeneity strongly impacts charge transport rates. To establish the source of heterogeneity, we performed EBSD analysis of the same domain. As shown in Figure 4.3, the EBSD patterns can be used to extract the local crystal orientation by fitting the pattern collected from each location to a reference pattern.[125] An example fit is shown on the averaged EBSD pattern displayed in Figure 4.3(b), which was collected from the $0.56\ \mu m^2$ area indicated in white on Figure 4.3(a). The orientation map shown in Figure 4.3(c) was constructed by applying fits to each EBSD pattern collected across the domain. A uniform color designation suggests that domain is single crystal, with the [001] direction oriented orthogonally to the substrate. Note the single pixel variations in orientation that can be seen in Figure 4.3(c) are attributed to instrument noise, as confirmed by visual comparison of patterns collected from the noise pixels with adjacent pixels that fit as a [001] orientation. The absence of grain boundaries in both the orientation map and SEM suggests that the structural heterogeneity contributing to variance in transport measurements arises from a more subtle source of structural disorder than polycrystallinity.

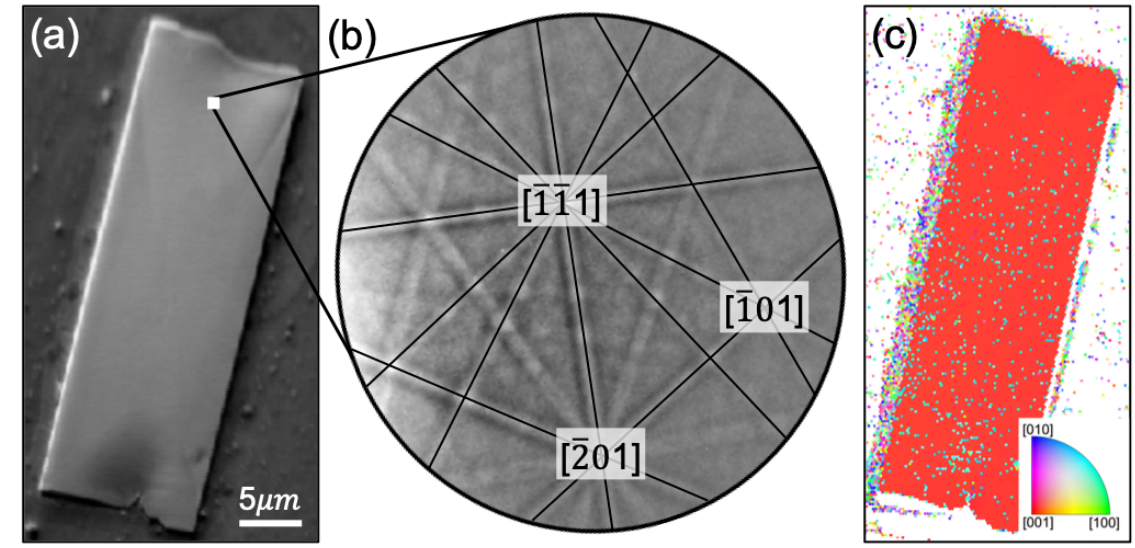

Figure 4.3. Orientation map of a single crystal $CsPbBr_3$ domain. Panel (a) reproduces the SEM of the single crystalline $CsPbBr_3$ perovskite shown in Figure 4.1. Panel (b) shows an EBSD pattern and corresponding fit with the $[\bar{1}\bar{1}1]$, $[\bar{2}01]$ and $[\bar{1}01]$ directions identified. Panel (c) shows the corresponding orientation map of the domain imaged in panel (a). In this case, red indicates that the crystal's [001] direction (c-axis) is orthogonal to the substrate.

To understand how subtle distortions of the crystal structure may be influencing excited state transport, we turned to EBSD pattern contrast. Local perturbations in crystal structure (anisotropic strain, vacancies, polycrystallinity) will result in an EBSD pattern with reduced contrast relative to a uniform single-crystal diffracting volume.[126-128] A common metric for quantifying diffraction pattern contrast is image quality (IQ), often calculated using the Hough transform method.[126] Here we have elected to use a generalized form of the Hough transform, called a Radon transform, which reduces undesirable artifacts caused by irregular pixel sampling.[129-130] Figure 4.4 illustrates the Radon transform we implemented to analyze the EBSD patterns in the LHP domain

discussed above. The three EBSD patterns shown in Figure 4.4(a) were collected from locations marked I, II, and III in Figure 4.1(a). Application of the Radon transform, followed by a median filter (to remove the low frequency background) and a minimum intensity threshold, yields the plots shown in Figure 4.4(b). Peaks in Radon space indicate the angle (θ) and center distance (x') of lines detected in the respective diffraction pattern. For the same minimum threshold value, the number of peaks decreases from location I to III, reflecting the smaller number of diffraction lines in the EBSD patterns that rise above the background level. Application of the inverse Radon transform yields the reconstructed patterns shown in Figure 4.4(c). While in all cases the reconstructed patterns illustrate good agreement between the lines picked out by the Radon transform and those that appear in the original diffraction patterns, the difference in contrast between the three is clearly captured by the algorithm. Image quality values (IQ_{RT}) are calculated by finding the average Radon space intensities. In accordance with the level of contrast present in each EBSD pattern, we measure IQ_{RT} values of 5.39, 2.63 and 0.63 for areas I, II and III, respectively.

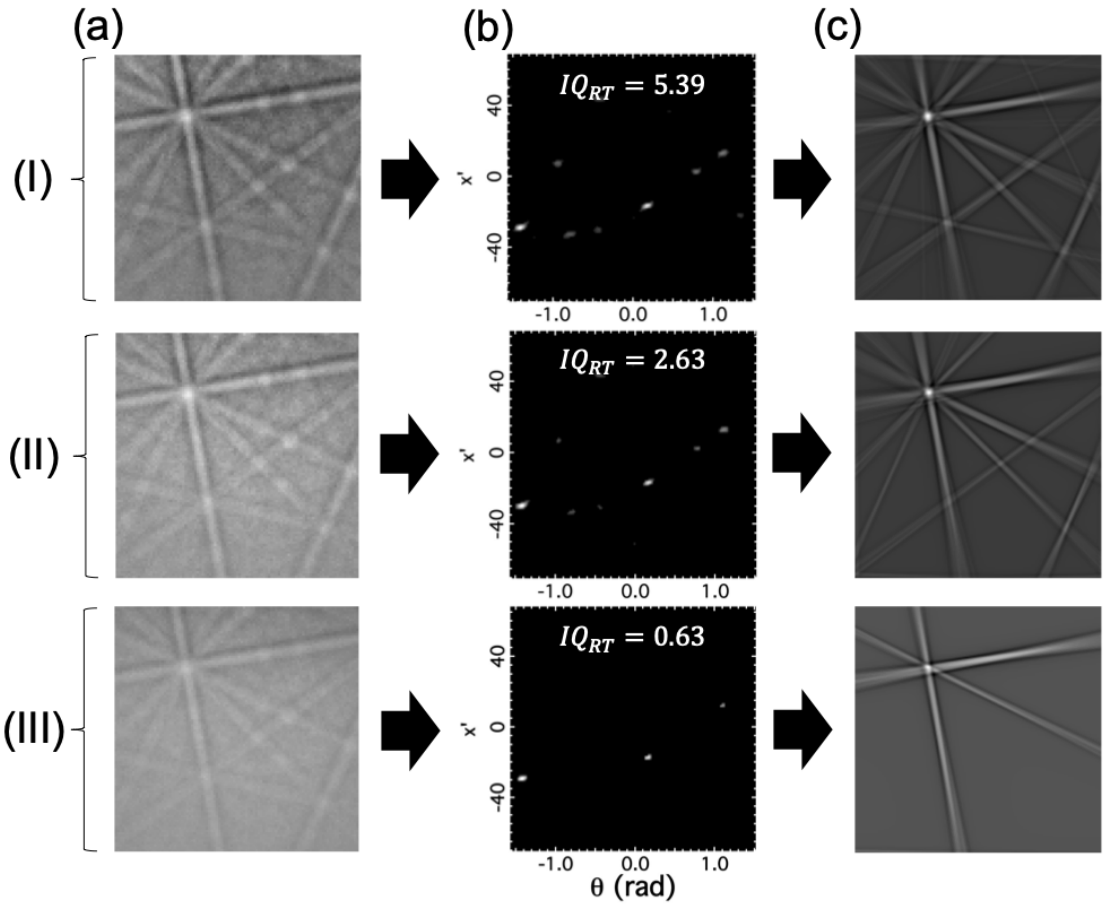

Figure 4.4. Image quality analysis of a single crystal $CsPbBr_3$ perovskite. Column (a) shows three EBSD patterns with decreasing levels of contrast (I, II and III). The corresponding Radon transform of each pattern is shown in column (b). IQ_{RT} values measured for I, II, and III are 5.39, 2.23, and 0.63, respectively. (c) The reconstructed diffraction patterns obtained by inverse Radon transform show good agreement with the original pattern.

To understand how the variation in lattice quality impacts charge transport, we numerically calculated IQ_{RT} for each of the 30,055 EBSD patterns we collected from the $CsPbBr_3$ domain. Figure 4.5(a) shows the resultant IQ_{RT} map, which represents high crystal quality (as determined by the magnitude of the IQ_{RT} value) as warmer colors and low crystal quality as cold colors. The bulk of the domain is dominated by moderate IQ_{RT}

values (light blue, ~3) with regions of reduced quality (dark blue, ~0.5) distributed throughout, and high IQ_{RT} regions (yellow, ~9) located within 5 μm of the top edge. While the IQ map only provides a relative measure of the crystal quality, the differences in diffraction pattern contrast strongly suggests that nanoscale variations in crystal structure are present even in a single crystal structure. When the nine ambipolar diffusion coefficients measured on the domain are plotted vs. the co-located average IQ_{RT} value (In Figure 4.5(b)), a clear correlation between the two measurements is found.

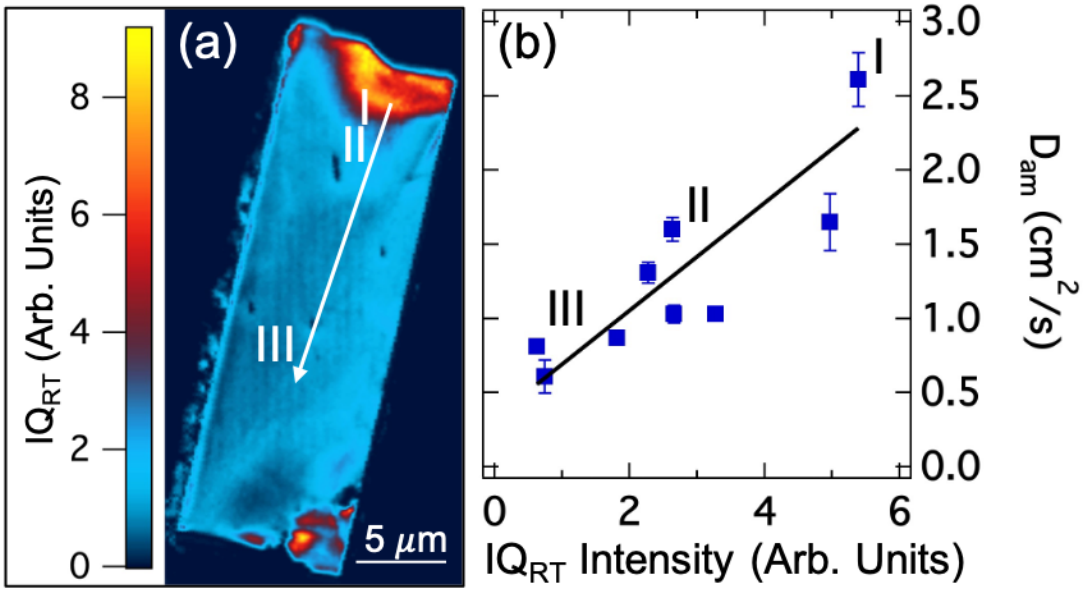

Figure 4.5. Correlation between image quality and ambipolar diffusivity. Panel (a) shows an IQ_{RT} map of the domain shown in Figures 4.1-4.3. IQ_{RT} measurements across the domain range from 0 to 9.2, with mostly moderate values (~3) throughout the bulk of the domain. (b) Measured diffusion coefficient vs. average IQ_{RT} for nine locations on the LHP domain. The IQ_{RT} values, which range from 0.63 to 5.39, are determined by averaging over a 0.56 μm^2 area in same nine locations in which diffusivity measurements were collected. Error bars correspond to one standard deviation. The black solid line is a guide to the eye.

The positive correlation between D_A and IQ_{RT} is strong evidence that local crystal quality plays an important role in determining charge carrier transport in $CsPbBr_3$. As

indicated in Fig. 4.3, the domain is single crystalline and therefore grain boundaries and other mesoscale defects can be ruled out as impeding transport. Instead, the reduced diffusion coefficients must relate to the periodicity of the lattice through which the charge carriers are transported. While it is difficult at present to identify the specific morphological defects that gives rise to reduced charge carrier mobility and reduced diffraction pattern contrast, the most likely candidate is anisotropic lattice strain, caused by, perhaps, a mismatch of thermal expansion coefficients upon cooling.[121, 131-132]

In the band picture of charge carrier transport, disruption of the periodicity of the lattice will reduce the mean scattering time of charge carriers, reducing the observed mobility. It may also be that point defects (vacancies and interstitials) or dislocations formed during the fabrication process give rise to lower energy, more strongly localized states that act as trap sites. In either case, our results suggest that structural disorder is manifest not only as mesoscopic structural defects (wrinkling, grain boundaries, etc.), for which the impacts on performance have been well documented,[108-109, 131, 133] but also as nanoscale disruptions of the lattice periodicity. These nanoscale defects strongly influence charge carrier transport while remaining undetectable unless local structural probes are employed.

4.3 Conclusion

In conclusion, we have coupled EBSD and ultrafast microscopy to directly correlate microscopic crystal quality to local charge carrier transport in a single crystal $CsPbBr_3$ domain. We find the ambipolar diffusion coefficient is reduced in regions of lower crystal quality, varying by nearly an order of magnitude across a single crystal

domain. Our results highlight not only the importance of crystal quality on device performance and stability, but also the critical need for correlative microscopy techniques in determining the impact of subtle defects on functional properties of nanoscale materials.

4.4 Experimental Methods

Low-coverage $CsPbBr_3$ thin films are produced using a solution processing technique which employs drop-casting and annealing steps. Specifically, 25 μL of CsBr (0.023 M) and $PbBr_2$ (0.023 M) precursors dissolved in DMSO are drop cast onto gold coated quartz substrates. Immediately after drop casting, the substrate is transferred onto a hotplate and annealed at 45°C overnight in a DMSO saturated atmosphere.

Transient reflectivity measurements were carried out using a homebuilt ultrafast pump-probe microscope. The primary excitation source is a Ti:sapphire laser that emits 70 fs pulses at 80 MHz and has a tunable range of 690 nm to 1040 nm. For the experiments described in this manuscript, the fundamental at 800 nm was split via a beam splitter into pump and probe lines. The probe beam is aligned onto a translation stage and coupled onto galvanometer mirrors to achieve temporal and spatial separation, respectively, relative to the pump beam. The pump is frequency doubled using a beta barium borate (BBO) crystal and recombined with the probe using a 50:50 beam splitter. The two beams are focused onto the sample using a 0.90 NA microscope objective, and the reflected probe signal is detected using a balanced photodiode coupled to a lock-in amplifier.[122]

Transport data was collected by spatially scanning the probe beam over the expanding photogenerated excited state density at increasing pump-probe time delays. Sets of spatially separated images were then used to determine radially averaged diffusion coefficients by fitting angle-resolved profiles to a numerical convolution (NC) of the experimentally-determined point spread function (measured at $\Delta t = 1\ ps$) with the Green's function solution to the diffusion equation $\left(K(r;t) = \frac{exp[-r^2/(4\ D_c\ t)]}{\sqrt{4\ \pi\ D_c\ t}}\right)$. Radial profiles at angle ϕ are obtained by first rotating the 2D signal profile by $-\phi$ radians (with appropriate interpolation), and then integrating along the columns. The resulting 1D profile is fit while only weighting data points on the right side of the profile. The reported diffusion coefficients are an average of 8 angle-resolved fits performed at intervals of $\pi/4$.[124]

EBSD patterns were collected using a Physical Electronics 710 scanning Auger nanoprobe with a 20keV electron beam. Patterns were collected on a 250 nm square sampling grid. A commercial computer software (EDAX's TEAM) was used to fit each diffraction pattern to a user-defined reference pattern[125], constructed from structure data obtained on the Crystallographic Open Database (COD) for orthorhombic $CsPbBr_3$ ($a = 8.207\text{Å}, b = 8.255\text{Å}, c = 11.759\text{Å}$).[134-140]

To determine IQ_{RT} values for collected EBSD patterns, a Mathematica script was written to perform the Radon transform and apply a median filter (radius of 5 pixels) to remove low-frequency background from the Radon space image. After a minimum threshold of the Radon space image (at 12% of the global intensity maximum), IQ_{RT} values were calculated by finding the average Radon space intensity.

CHAPTER FIVE

A REDUCED ARTIFACT APPROACH FOR DETERMINING DIFFUSION COEFFICIENTS IN TIME-RESOLVED MICROSCOPY

Contributions of Authors and Co-Authors

Manuscript in Chapter 5

Author: Casey L. Hickey

Contributions: Synthesized and characterized all samples. Collected and analyzed all ultrafast microscopy data assisted in data modeling. Assisted in writing and editing manuscript.

Author: Erik M. Grumstrup

Contributions: Assisted with data modeling and analysis as well as editing of the manuscript for final submission.

Manuscript Information

Casey L. Hickey and Erik M. Grumstrup

Journal of Physical Chemistry C

Status of Manuscript:
____Prepared for submission to a peer-reviewed journal
_X__ Officially submitted to a peer-review journal
____ Accepted by a peer-reviewed journal
____ Published in a peer-reviewed journal

Date Submitted: March 15, 2020

5.1 Introduction

Diffusion coefficient measurements are a critical component of the work presented in the previous three chapters. While such approaches are increasingly utilized to characterize diffusion in a variety of systems,[17, 141-143] we have often noticed that the point spread function is not an ideal Gaussian. To understand what effect non-ideality has on the determined diffusivity value, we have compared the traditional Gaussian approach against a newly developed approach which accounts for the experimentally determined point spread function.

Ultrafast microscopy has emerged as a versatile method for characterizing excited state behavior of charge carriers in semiconducting materials. One particularly powerful capability of the technique is direct imaging of excited state spatial evolution on sub-micron length scales and sub-picosecond time scales.[62, 144-146] By photoexciting a spatially confined excited state population and optically imaging its subsequent spatial evolution, ultrafast microscopy provides the ability to probe excited state transport in a contact-free manner in the bulk [29, 147-151] and on nanoscale objects.[28, 152-153] The excellent spatial resolution of the technique also provides a means to measure transport in proximity to localized structural or chemical defects so that their impact on bulk properties can be directly probed.[27, 120, 154-155]

Because the optical configurations of ultrafast microscopes vary from instrument to instrument, the effective point spread function that is convolved with the light-matter interaction of interest varies for each practitioner. Although some authors have accounted for sample or instrument specific variability in the point spread function,[150] it is far more

prevalent to analyze excited state transport data assuming a Gaussian model when fitting the evolving excited state distribution. In the limit of perfectly Gaussian beams, fits with a Gaussian model will clearly recover the correct diffusion coefficient. However, from an experimental perspective, it is often impractical to completely eliminate non-idealities in the point spread function due to, for example, minor wavefront distortion or spherical aberrations.[156] As we show below, even subtle deviations from Gaussian beam profiles can cause significant error in the determined diffusion coefficient. To circumvent the limitations presented by the Gaussian model, we propose a simple alternative approach which instead relies on numerical convolution of the Green's function solution to the diffusion equation with the experimentally determined point spread function. We demonstrate that this approach provides more accurate diffusion coefficients, especially in the case of anisotropic diffusion and non-Gaussian shaped beams.

5.2 Methods

Photoexcitation with a focused laser produces a highly localized distribution of excited states. In the absence of a potential gradient and on time scales much longer than the mean scattering time of these excited states (i.e. when the excited state population has thermalized), the population (P_{ex}) spatially evolves according to the diffusion equation, which, with a spatially invariant diffusion coefficient (D_c), is given by (in 1D):

$$\frac{\partial P_{ex}}{\partial t} = D_c \frac{\partial^2 P_{ex}}{\partial r^2}. \qquad \text{(Eq. 1)}$$

The well-known solution to the diffusion equation for a point (delta function) source at $t = 0$ is the Green's function,[157]

$$K(r;t) = \frac{exp[-r^2/(4\,D_c\,t)]}{\sqrt{4\,\pi\,D_c\,t}}. \quad \text{(Eq. 2)}$$

If excited state generation scales linearly with pump intensity, the excited state density at a time Δt after photoexcitation is given by the convolution of the diffusion kernel, $K(r;\Delta t)$, with the spatial profile of the pump pulse intensity, $I_{pu}(r)$,

$$P_{ex}(r,\Delta t) \propto I_{pu}(r) \otimes exp[-r^2/(4\,D_c\,\Delta t)] \quad \text{(Eq. 3)}$$

Expressed in this way, the spatial evolution of excited state density can be interpreted as follows: At $\Delta t = 0$, the pump pulse creates a distribution of localized excited states, with a probability determined by the pump intensity at a given location. Each delta function source evolves according to Eq. 2 to produce a Gaussian-broadened new distribution. The overall excited state density is given by the sum over each (now broadened) distribution, yielding $P_{ex}(r,\Delta t)$. Note that, for this manuscript, we are neglecting excited state decay, which is generally accounted for by additional terms in Eq. 1 that describe linear and nonlinear decay mechanisms. For cases in which nonlinear decay is relevant, coupling between excited state decay and transport can significantly influence experimental measurements.[158] However, for cases where excited state decay is independent of the population density (typically low photoexcitation densities), the excited state decay is decoupled from transport, allowing us to neglect it for clarity.

To determine a diffusion coefficient with time resolved microscopy, P_{ex} is imaged by scanning a focused probe over the field of view of the microscope or, alternatively by using wide-field illumination in combination with a two-dimensional detector.[29, 151] Mathematically, this operation corresponds to a spatial convolution of the excitation density and the probe beam spatial profile (or equivalently, the point spread function of

the microscope). Thus, the spatially- and temporally-dependent excited state signal is given by:

$$I(r,\Delta t) \propto \mathrm{I_{pr}(r)} \otimes I_{pu}(r) \otimes K(r;\Delta t). \qquad \text{(Eq. 4)}$$

If the pump and probe spatial profiles are Gaussian in shape, the convolution can be performed analytically, yielding a signal that is also a Gaussian,

$$I(r,\Delta t) \propto \exp\left(\frac{-r^2}{2\sigma_0^2+4D_c\Delta t}\right) = \exp\left(\frac{-r^2}{2{\gamma_{\Delta t}}^2}\right). \qquad \text{(Eq. 5)}$$

Here, $\sigma_0 = \left(\sigma_{pu}^2 + \sigma_{pr}^2\right)^{1/2}$ is the time-independent standard deviation of the pump-probe spatial convolution, typically measured at a delay time before the excited state has undergone any spatial evolution. Thus, by simply measuring the delay-dependent standard deviation ($\gamma_{\Delta t}$) of the expanding signal profiles, the diffusion coefficient can be determined.

$$D_c = \frac{\gamma_{\Delta t}^2 - \sigma_0^2}{2\Delta t}. \qquad \text{(Eq. 6)}$$

An advantage of this approach is that the ability to measure small diffusion coefficients (or equivalently, small diffusion lengths) is not determined by spatial resolution, but rather by the minimum resolvable differences in signal profile width, which is determined by the signal to noise level of the measurement.

While the assumption of Gaussian pump and probe spatial profiles allows a closed form expression for fitting signal profiles, it can, as we show below, lead to significant error in the experimentally determined diffusion coefficient. The error arises from non-Gaussian beam profiles, which can be introduced through a number of aberration sources which result in beam spots that are distorted from their ideal spatial distribution. Even in

the case that deviations from Gaussian are subtle and the convolved pump-probe point spread function appears to be high quality, error can be introduced by fitting with a Gaussian model.

An alternative to assuming a Gaussian pump-probe spatial profile is to instead use the true, non-analytic profile, as experimentally measured. The convolution operation is associative, and therefore, from Eq. 4,

$$I(r,\Delta t) \propto \left[\mathrm{I_{pr}(r)} \otimes I_{pu}(r)\right] \otimes K(r;\Delta t). \qquad \text{(Eq. 7)}$$

The term in brackets is the time-independent convolution of the pump and probe beams, which, in a practical sense, can be measured experimentally at $\Delta t = 0$. We refer to this quantity as the effective point spread function (PSF) as it is a time-independent measure of the spatial resolution of this class of measurements. The Green's function kernel is analytic and well-defined at a given pump-probe delay time. Thus, rather than assuming a Gaussian function throughout, the numerical convolution represented by Eq. 7 ought to produce the exact profile of the time-dependent signal, even in the limit of a complex shaped effective PSF.

5.3 Results and Discussion

To determine the efficacy of the numerical convolution (NC) fit, we compare it to the commonly utilized Gaussian fitting analysis on modeled data designed to illustrate three common experimental scenarios. In all cases, we used a Kinetic Monte Carlo (KMC) approach to model the two-dimensional diffusive motion of excited state particles. Each fitting algorithm is used to determine the radial diffusion coefficient for

16 angles about the center of the 2D signal profile. An example signal profile is shown in Figure 5.1(A). For both fitting routines, the signal profile is rotated to the angle normal, integrated, and then fit while weighting only one side of the modeled data. For example, to determine the diffusion along the π/4 vector direction, the image is rotated by -π/4 and integrated along the columns. The resultant 1-dimensional data set is then fit while weighting data points only on the right side of the profile.

In Figure 5.1(A-C) we compare the Gaussian fit and NC approaches for an initial excited state distribution given by $\left[\mathrm{I_{pr}(r)}\otimes I_{pu}(r)\right] = \exp\left(\frac{-r^2}{2\sigma_0^2}\right);\ \sigma_0 = 0.64\ \mu m$. Not surprisingly, for an initial Gaussian distribution, both fits accurately determine the isotropic modeled diffusion coefficient, $D_A = 1.95\ cm^2/s$ (panel B). Panel C shows representative fits of each model (NC in red and Gaussian in blue) to the simulated data in the π/4 direction. Negligible residuals, plotted below panel C, illustrate the ability of each model to accurately capture a Gaussian effective PSF.

Figure 5.1(D-E) shows a similar analysis, except the effective PSF is now given by a sum of Gaussians, $\left[\mathrm{I_{pr}(r)}\otimes I_{pu}(r)\right] = \exp\left(\frac{-r^2}{2\sigma_{0,1}^2}\right) + 0.03\exp\left(\frac{-r^2}{2\sigma_{0,2}^2}\right);\ \sigma_{0,1} = 0.64\ \mu m, \sigma_{0,2} = 1.60\ \mu m$. We highlight that the second Gaussian term has only 3% relative amplitude but is much broader, effectively increasing the amplitude of the wings in the initial distribution. Surprisingly, the fitting methods extract substantially different diffusion coefficients. As shown in panel E, the Gaussian fit determines, on average, a value of $D_A = 2.11 \pm 0.02\ cm^2/s$, which represents an approximately 8% overestimation of the true diffusion coefficient. Comparatively, the NC fit determines an

average diffusivity of $D_A = 1.92 \pm 0.04\ cm^2/s$. A plot of the residuals, shown below panel F, suggests the Gaussian fit does not capture the tail of the modeled distribution.

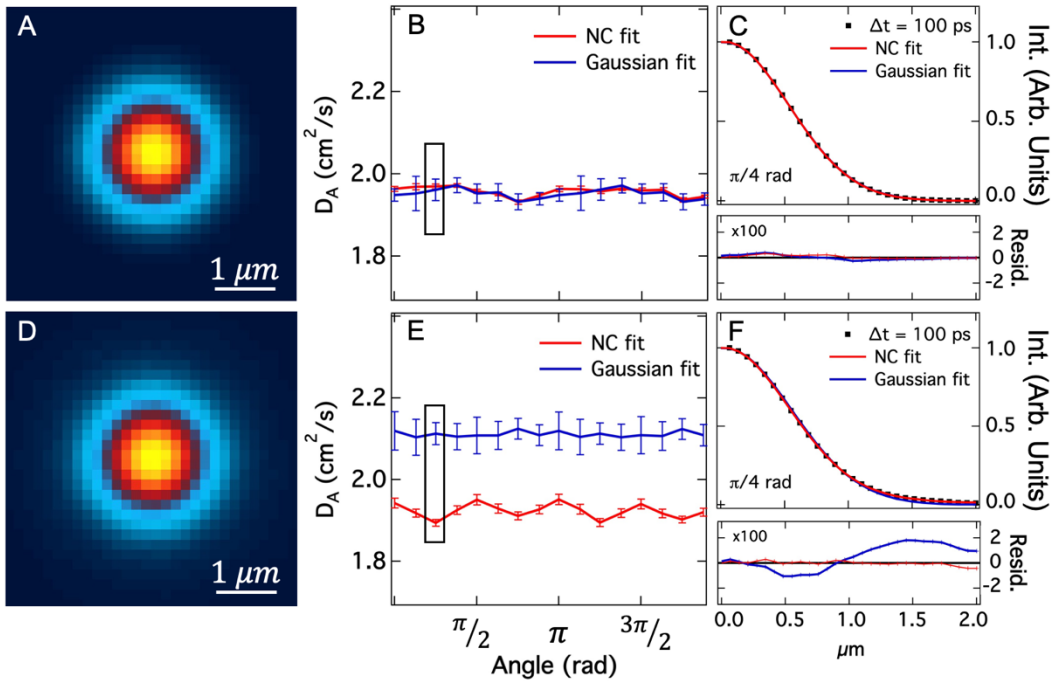

Figure 5.1. Diffusion modeled on Gaussian and near-Gaussian PSFs. Gaussian (panel A) and near-Gaussian (panel D, see text for functional form) initial distributions. Panels (B) and (E) shows the ambipolar diffusion coefficient for 16 radial direction as determined by NC (red) and Gaussian (blue) fits for the two initial distributions. In the case of a Gaussian PSF (panel B), both the NC and Gaussian fits accurately determine the modeled diffusivity ($D_A = 1.96 \pm 0.02\ cm^2/s$ and $1.95 \pm 0.02\ cm^2/s$, respectively). Representative fits to the modeled distribution at $\pi/4$ radians when $\Delta t = 100\ ps$ are shown in panel (C). Panel (E) shows that for a near-Gaussian distribution, the Gaussian fit, on average, overestimates the true diffusivity by 8% ($D_A = 2.11 \pm 0.02\ cm^2/s$), while the NC fit only deviates by 1.5% ($D_A = 1.92 \pm 0.04\ cm^2/s$). Corresponding fits along $\pi/4$ for $\Delta t = 100\ ps$ are shown in panel (F). The residual plot shows the Gaussian fit overestimates the values of the distribution near the top of the profile and underestimates it near the tail compared to the NC fit, which accurately captures the entire shape of the profile.

It is worth noting that the Gaussian fit can be substantially improved by, for example, weighting the data points in the fit by their relative amplitude or by cropping the image to eliminate the low signal data points. In either case, the effect is to reduce importance of the low signal regions in the fitting routine. If these procedures are followed, one can force the Gaussian fit to retrieve the correct diffusion coefficient. On the other hand, the NC approach retrieves the correct diffusion coefficient without any human input or weighting, which in our view makes it a more robust approach.

While the near-Gaussian of Fig. 5.1(D-F) illustrates the importance of low-amplitude deviations from Gaussian, it is not a realistic representation of aberrations encountered in practice. To explore the effects of these often-anisotropic aberrations, we next modeled diffusion, again using KMC generated data, except with initial conditions determined by two experimentally-collected PSFs. These profiles, $\left[\mathrm{I_{pr}(r)}\otimes I_{pu}(r)\right]$, shown in panels (A) and (B) of Figure 5.2, were collected on a pristine Si (111) wafer. Panel (A) shows a typical effective PSF with minor aberrations and panel (B) shows an effective PSF with obvious aberrations caused by reflection of the pump off of a warped dichroic beamsplitter. Figure 5.2(B) shows the angle-resolved diffusion coefficients determined by each method for the profile in panel A. The NC and Gaussian fits measure average diffusion coefficient values of $D_A = 1.85 \pm 0.19\ cm^2/s$ and $D_A = 1.99 \pm 0.29\ cm^2/s$, respectively. While the traditional Gaussian method only overestimated the value by ~2%, a greater concern is that the error of the fit increases to nearly 15% along the $3\pi/2$ direction. The deviation stems from the large amplitude tail shown in panel C. As can be seen in the residual plot, the Gaussian model is clearly a poor fit along this

direction, leading to the significant overestimation of the diffusion coefficient in the $3\pi/2$ direction. In contrast, despite the anisotropic PSF, the NC approach recovers a nearly isotropic diffusion coefficient that is quantitatively correct within error.

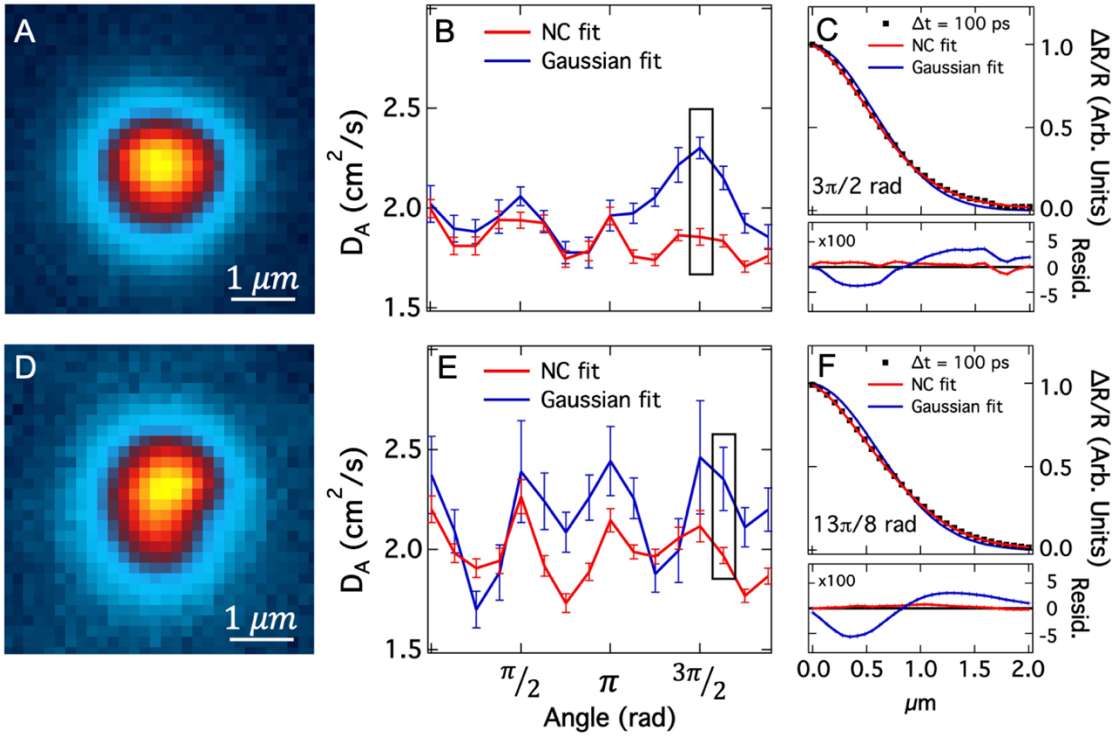

Figure 5.2. Diffusion modeled on experimentally collected PSFs. Excited state diffusion was simulated for a typical (A) and a strongly distorted (D) PSF. Panels (B) and (E) show angular resolved diffusion coefficients determined by both models for the typical and distorted PSFs, respectively. In the case of the typical PSF, the NC fit determines an average diffusion coefficient of $D_A = 1.85 \pm 0.19\ cm^2/s$ and the Gaussian determines $D_A = 1.99 \pm 0.29\ cm^2/s$. In the case of the distorted PSF, the NC fit determines an average diffusion coefficient of $D_A = 1.98 \pm 0.29\ cm^2/s$ and the Gaussian approach determines $D_A = 2.18 \pm 0.44\ cm^2/s$. Panels (C) and (F) show representative PSF profiles and corresponding NC (red) and Gaussian (blue) fits. Residual plots, shown below the respective fits, illustrate that the Gaussian fit systematically overestimates PSF signal values near the top of the profile and underestimates values near the tail.

In the case of the strongly distorted PSF shown in panel D, the error associated with a Gaussian fit analysis is significantly increased. As can be seen in panel E, the

average diffusion coefficient determined by the Gaussian fit is $D_A = 2.18 \pm 0.44\ cm^2$, representing an 11% average error, however, the determined values are highly variable, spanning 1.7 cm²/s at $\pi/4$ to 2.4 cm²/s at $3\pi/2$. It is clear from the profiles and corresponding fits shown in panel F that the failure of the fitting routine derives from a poor fit of a Gaussian to the shape of the experimental PSF, particularly when long tails distort the PSF. Comparatively, the NC method extracts an average $D_A = 1.98 \pm 0.29\ cm^2/s$. While this average value is nearly quantitatively correct, the agreement is due in large part to cancellation of error, as evidenced by the significant variability along different radial components. Nevertheless, the NC approach has less variability than the Gaussian approach, suggesting that it is more robust to artifacts stemming from effective PSFs which strongly deviate from optimal.

A recent area of interest in ultrafast microscopy is imaging transport in the vicinity of defects or across interfaces, where the apparent diffusion rate of an excited state population might be expected to be anisotropic due to potential barriers[154] or anisotropic strain[155, 159-160]. To explore the limits of transport imaging under such circumstances, we compared the Gaussian and NC fitting approaches for cases in which the diffusion coefficient was 10% larger in the $\pi/4$ radial direction, as illustrated in panel A of Figure 5.3. Panel B compares the normalized 2D integrated profile along $\pi/4$ at $\Delta t = 0\ ps$ and $\Delta t = 250\ ps$. While subtle, the increased probability of a hop along $\pi/4$, as parameterized in the KMC model, is visible as a slight asymmetric broadening. Panel C shows the angle-resolved diffusion coefficients. The solid black curve shows the theoretical diffusion coefficient based on the cosine projection of the asymmetric hop

rate. Both fitting methods exhibit some variability due to the asymmetric effective PSF, but the NC fit reproduces the expected angular dependence more accurately. The failure of the Gaussian fit is particularly visible near $3\pi/2$, where the determined diffusion coefficient substantially deviates from the modeled value due to relatively large amplitude wings in the effective PSF. While the NC fitting approach is not error-free, it is, on average, more robust against artifacts caused by non-ideal effective PSFs.

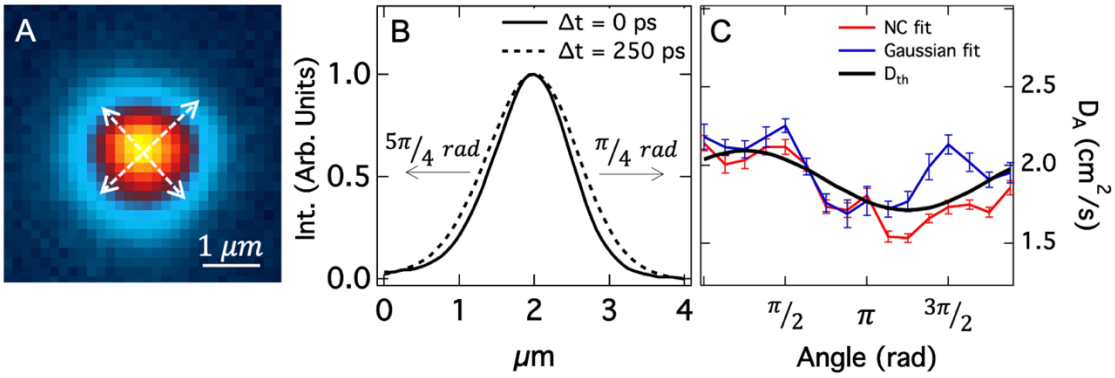

Figure 5.3. Modeled anisotropic diffusion. Excited state diffusion was simulated for the 2D effective PSF shown in panel (A) with the KMC model parameterized for a 10% greater hopping rate in the $\pi/4$ radial direction. Integrated profiles illustrating asymmetrical expansion of the carrier distribution are shown in panel (B). The profile for $\Delta t = 250\ ps$, is subtly broadened in the $\pi/4$ direction. The red and blue traces in panel (C) show angular resolved diffusion coefficients measured using the NC and Gaussian fits, respectively. The black solid line shows the theoretical diffusion coefficient obtained by projecting the asymmetric hopping rate along each radial coordinate. The Gaussian fit deviates significantly near $3\pi/2$ because of long tails in the effective PSF.

5.4 Conclusion

In conclusion we have presented a comparison of the gaussian and numerical convolution approaches to fitting transport data from a time-resolved microscope. The numerical convolution approach uses the experimentally measured effective point spread function which is convolved with the Green's function solution to the diffusion equation. Because the NC approach relies on an experimental measurement, it is somewhat sensitive to noise. However, we note that the effective PSF is measured at early times after photoexcitation, when signal to noise ratios are highest. Most importantly, by performing a numerical convolution in the fitting routine, non-ideal effective PSFs, which reflect the beam aberrations induced by the imaging system, are automatically accounted for, reducing artifacts in experimentally-determined diffusion coefficients.

CHAPTER SIX

CONCLUSIONS AND FUTURE DIRECTIONS

6.1 Future Work

Although the research in this dissertation presents progress in characterizing the excited state transport and recombination dynamics in LHPs, there remain outstanding questions related to the impact of chemical and structural heterogeneity on LHP photophysics. Specifically, the future aims of this research are to determine (*1) the impact of mixed-halide compositions on the behavior of photoexcited charge carriers, (2) how observed twin boundaries affect excited state recombination dynamics and carrier transport in LHPs and (3) what is the cause of observed anisotropic diffusion in $CsPbBr_3$ perovskites.*

Mixed Halides

A desirable method for fine-tuning the bandgap of LHPs is to mix the halide composition. However, as described in Chapters 2 and 3, halide chemistry plays an integral role in determining the behavior of photoexcited charge carriers in lead halide perovskites. As an additional example, Figure 6.1 shows the average diffusion coefficient measured for three different $CsPbBr_xI_{(3-x)}$ perovskites (blue squares) as a function of x. We measure D_{avg} values of 0.3, 0.8 and 1.3 cm^2/s for x = 1, 2, and 3, respectively. It should be noted that $CsPbI_3$ (x = 0) is not stable at room temperature and thus the diffusion coefficient cannot be measure for that particular species. However, as shown in Chapter 3, the cation does not play a significant role in determining diffusivity in LHPs.

Therefore, we can assume the diffusion coefficient when x = 0 is similar to that of $MAPbI_3$ (red squares, $D_{avg} = 1.25$ cm^2/s) and conclude that LHPs with mixed-halide compositions (0 < x < 3) have reduced mobilities relative to LHPs with pure halide compositions (x = 0 and x = 3).

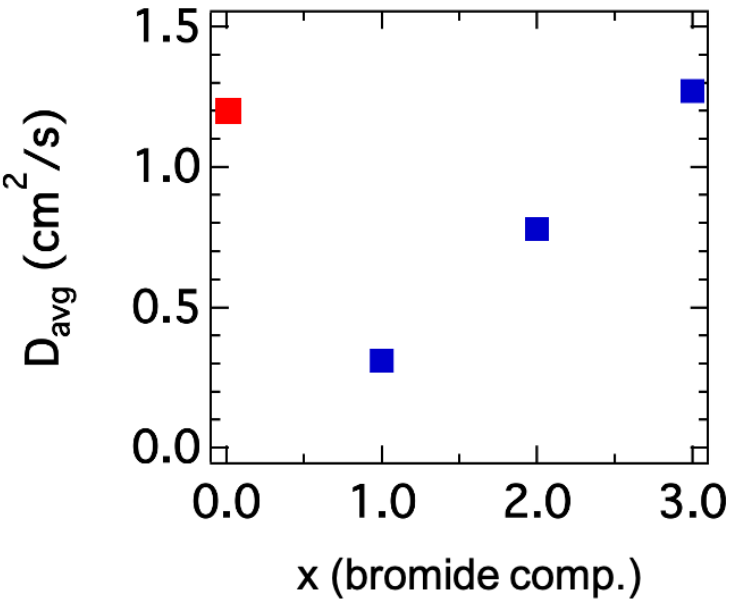

Figure 6.1. Diffusion in cesium lead mixed halide perovskites. Diffusion coefficients were measured for three different $CsPbBr_xI_{(3-x)}$ perovskite species (blue squares). We observe an average diffusion coefficient of 0.3 cm^2/s, 0.8 cm^2/s and 1.3 cm^2/s when x = 1, 2 and 3, respectively. The red square represents the average diffusion coefficient (1.25 cm^2/s) measured for $MAPbI_3$.

It is unknown if reduced mobilities observed in mixed halide perovskites are due to disorder in the energetic or structural landscape of the material. Given the sensitivity of perovskite band structure to changes in halide composition, it is plausible that fluctuations in halide energy density throughout a mixed-halide lattice would impact carrier transport. However, if energetic disorder, like that which drives alloy scattering,

was the only reason for reduced transport we would expect the reduction in mobility between x = 0 or 3 and x=1.5 to be less than 10%.[161-162] Alternatively, because halide ions distribute stochastically throughout the lattice (XRD patterns show isotropic contraction of the lattice) it is possible that structural heterogeneity is driving reduced transport in mixed halide perovskites. The results presented in Chapter 4 show that even in the case of single crystalline domains, subtle fluctuations in lattice structure impedes transport of photogenerated charge carriers. Thus, it is reasonable to predict that for mixed-halide perovskites, inhomogeneous distribution of the halides will cause disorder in the lattice structure such that transport will be reduced relative to pure halide species. If structural disorder is responsible for reduced mobilities in mixed halide perovskites, we would expect locally measured lattice quality to scale inversely with carrier mobility. Further, because distribution of the differently sized ions is heterogenous, we would expect random fluctuations in lattice parameters which can also be detected using EBSD.

Twin Boundaries

For birefringent LHP species (i.e. species which adopt a tetragonal or orthorhombic lattice geometry like $MAPbI_3$, $CsPbI_2Br$, $CsPbIBr_2$ and $CsPbBr_3$) polarized light microscopy (PLM) experiments have determined that solution processing techniques lead to the formation of twin boundaries within the crystallites. Panels (A) and (B) of Figure 6.2 show a SEM and corresponding PLM image of an individual $CsPbBr_3$ perovskites, respectively. To confirm the observed twins, we collected a series of PLM images and measured the transmittance as a function of polarization angle on both sides of the proposed twin boundary which is identified by the dashed lines in panels (A) and

(B). As shown in panel (C), the intensity on the left (blue) and right (red) sides of the boundary are ~30 degrees out of phase with one another and indicate twinning is indeed occurring.

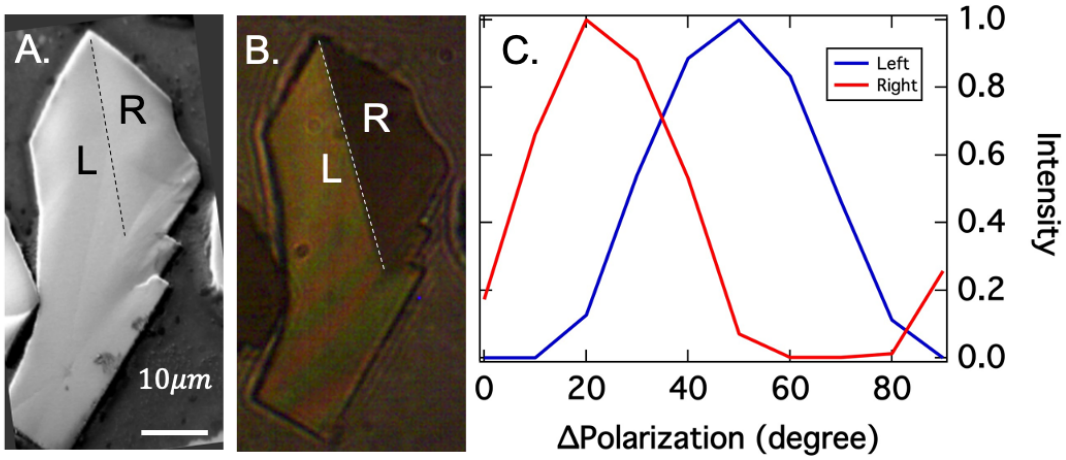

Figure 6.2. Twinning in $CsPbBr_3$ perovskites. Panels (A) and (B) show SEM and PLM images of an individual $CsPbBr_3$ domain, respectively. Panel (C) shows a plot of intensity as a function of polarization angle measured from the left (blue) and right (red) sides of the domain and indicate a 30-degree phase difference between the two twins.

Twin interfaces are considered to be a type of grain boundary, but their impact on solar cells is poorly understood.[163] Grain boundaries are typically considered to be defect rich interfaces which are known to be detrimental to photovoltaic device performance.[164] However, twin boundaries are coherent interfaces which require lattice periodicity to be preserved.[164] In CdTe solar cells, twin boundaries have actually been shown to improve performance by providing an efficient channel for transport.[163] Given the present knowledge gap, exploiting the spatial resolution enabled by ultrafast microscopy to explore carrier transport across twin boundaries in LHPs would be beneficial to the photovoltaic community. A simple experiment to deduce twin boundary effects would

include first confirming the existence of a twin, either by PLM or EBSD, then systematically measuring diffusion as a function of distance across the boundary. In principle, if carrier transport is impacted by the presence of a twin interface, a spike or dip in the measured diffusivity would occur at the location of the boundary. However, since twin-interfaces are atomically thin, a change in diffusivity may be subtle and difficult to resolve.

Anisotropic Diffusion

The ability to capture asymmetric evolution of the excited state carrier density is important to fully understanding carrier transport in materials. Using the NC fit method described in Chapter 5, we see previously unobserved anisotropic diffusion in $CsPbBr_3$ perovskite microcrystals. Figure 6.3(A) shows a scanning electron micrograph (SEM) of an individual $CsPbBr_3$ domain taken with a scanning Auger nanoprobe. A corresponding PPM image of the same domain is shown in panel (B). Spatially separated PPM data was collected from the areas indicated by red and black circles in panels (A) and (B). The diffusion coefficients, as measured using the NC fit, are plotted as function of radial direction in panel (C). In both cases, diffusion is observed to be fastest ($D_A = 1.41 \pm 0.03\ cm^2/s$ and $D_A = 1.46 \pm 0.06\ cm^2/s$ for the red and black areas, respectively) in the $^{7\pi}/_{4}$ direction.

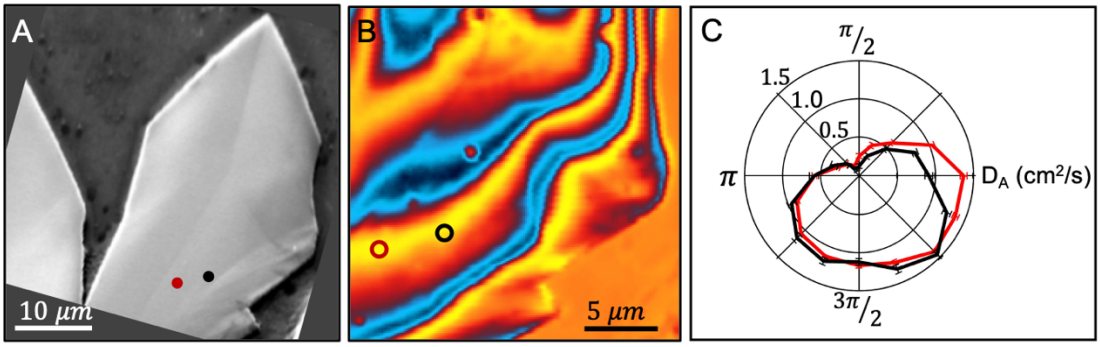

Figure 6.3. Anisotropic diffusion in $CsPbBr_3$ perovskites. Panel (A) shows a SEM of an individual $CsPbBr_3$ domain, and the corresponding PPM image in panel (B). The red and black traces in panel (C) correspond to diffusion data collected from the areas indicated by red and black circles in panels (A) and (B). As shown in (C), diffusion is fastest in the $^{7\pi}/_{4}$ direction. We measure $D_A = 1.41 \pm 0.03\ cm^2/s$ and $D_A = 1.46 \pm 0.06\ cm^2/s$ for the red and black areas, respectively.

Although the exact cause of anisotropic diffusion shown in Figure 6.3 is unknown, it is possible that lattice strain is lowering the bandgap such that charges are preferentially moving towards the edge of the domain. Similar effects occur when tensile and compressive strain (i.e. bending) is applied to inorganic semiconducting nanowires.[155, 159-160] Alternatively, surface recombination may be occurring at higher rates in the $^{3\pi}/_{4}$ direction and as a consequence diffusion appears to be faster in the $^{7\pi}/_{4}$ direction. Importantly, Figure 6.3(C) shows that diffusion goes to zero in the $^{5\pi}/_{8}$ direction and suggests the presence of a hard barrier in the lattice. Therefore, to investigate this matter further, it will be important to couple spatially resolved transport measurements with careful characterization of the lattice, perhaps via EBSD.

6.2 Conclusions

The work presented in this dissertation provides an in-depth characterization of the excited state transport and recombination dynamics which occur in a series of LHP materials. In Chapter 2 we investigated the impact of halide composition on charge transport and recombination dynamics in cesium lead mixed halide perovskites. We found that trap-mediated (first-order) recombination dominates at low fluences, with Auger recombination becoming increasingly important as the excitation density increases. We also measured an average diffusivity nearly 10x lower than that observed in $MAPbI_3$. In Chapter 3 we found that the dielectric constants relevant to photoexcited charge carriers in $CsPbBr_3$ and $MAPbBr_3$ perovskites are intermediate between the high and low frequency limits and that halide chemistry plays an integral role in determining the screening ability of LHPs. In Chapter 4 we determined that solution processing methods can cause subtle lattice defects which act to impede transport and risk going undetected by bulk measurement techniques. Finally, in Chapter 5 we develop a new method of calculating the diffusion coefficient from spatially separated PPM images which doesn't rely on a Gaussian shaped point spread function but rather a numerical convolution of the actual point spread function with the diffusion equation. Our new method has proven to more accurately determine the diffusion coefficient, especially in the case of an anomalous PSF.

REFERENCES CITED

1. Kojima, A.; Teshima, K.; Shirai, Y.; Miyasaka, T., Organometal Halide Perovskites as Visible-Light Sensitizers for Photovoltaic Cells. *J. Am. Chem. Soc.* **2009**, *131*, 6050-6051.

2. Tablero Crespo, C., The Effect of the Halide Anion on the Optical Properties of Lead Halide Perovskites. *Sol. Energy Mater. Sol. Cells* **2019**, *195*, 269-273.

3. Buizza, L. R. V.; Crothers, T. W.; Wang, Z.; Patel, J. B.; Milot, R. L.; Snaith, H. J.; Johnston, M. B.; Herz, L. M., Charge-Carrier Dynamics, Mobilities, and Diffusion Lengths of 2d–3d Hybrid Butylammonium–Cesium–Formamidinium Lead Halide Perovskites. *Adv. Funct. Mater.* **2019**, *29*.

4. Kim, A.; Hee Son, B.; Sik Kim, H.; Hyan Ahn, Y., Direct Measurement of Diffusion Length in Mixed Lead-Halide Perovsktie Films Using Scanning Photocurrent Microscopy. *Curr. Opt. Photonics* **2018**, *2*, 514-518.

5. Rosales, B. A.; Hanrahan, M. P.; Boote, B. W.; Rossini, A. J.; Smith, E. A.; Vela, J., Lead Halide Perovskites: Challenges and Opportunities in Advanced Synthesis and Spectroscopy. *ACS Energy Lett.* **2017**, *2*, 906-914.

6. Jeon, N. J.; Na, H.; Jung, E. H.; Yang, T.-Y.; Lee, Y. G.; Kim, G.; Shin, H.-W.; Il Seok, S.; Lee, J.; Seo, J., A Fluorene-Terminated Hole-Transporting Material for Highly Efficient and Stable Perovskite Solar Cells. *Nat. Energy* **2018**, *3*, 682-689.

7. Song, J.; Li, J.; Li, X.; Xu, L.; Dong, Y.; Zeng, H., Quantum Dot Light-Emitting Diodes Based on Inorganic Perovskite Cesium Lead Halides (Cspbx3). *Adv. Mater.* **2015**, *27*, 7162-7.

8. Xu, L.; Li, J.; Fang, T.; Zhao, Y.; Yuan, S.; Dong, Y.; Song, J., Synthesis of Stable and Phase-Adjustable Cspbbr3@Cs4pbbr6 Nanocrystals Via Novel Anion–Cation Reactions. *Nanoscale* **2019**, *1*, 980-988.

9. Li, X.; Wu, Y.; Zhang, S.; Cai, B.; Gu, Y.; Song, J.; Zeng, H., Cspbx3quantum Dots for Lighting and Displays: Room-Temperature Synthesis, Photoluminescence Superiorities, Underlying Origins and White Light-Emitting Diodes. *Adv. Funct. Mater.* **2016**, *26*, 2435-2445.

10. Xing, J.; Liu, X. F.; Zhang, Q.; Ha, S. T.; Yuan, Y. W.; Shen, C.; Sum, T. C.; Xiong, Q., Vapor Phase Synthesis of Organometal Halide Perovskite Nanowires for Tunable Room-Temperature Nanolasers. *Nano Lett.* **2015**, *15*, 4571-7.

11. Jia, Y.; Kerner, R. A.; Grede, A. J.; Rand, B. P.; Giebink, N. C., Continuous-Wave Lasing in an Organic–Inorganic Lead Halide Perovskite Semiconductor. *Nat. Photonics* **2017**, *11*, 784-788.

12. Shen, K., et al., Enhanced Performance of Zno Nanoparticle Decorated All-Inorganic Cspbbr3 Quantum Dot Photodetectors. *J. Mater. Chem. A* **2019**, *7*, 6134-6142.

13. Miao, J.; Zhang, F., Recent Progress on Highly Sensitive Perovskite Photodetectors. *J. Mater. Chem. C* **2019**, *7*, 1741-1791.

14. Govinda, S., et al., Behavior of Methylammonium Dipoles in Mapbx3 (X = Br and I). *J. Phys. Chem. Lett.* **2017**, *8*, 4113-4121.

15. Miyata, K.; Meggiolaro, D.; Trinh, M. T.; Joshi, P. P.; Mosconi, E.; Jones, S. C.; Angelis, F. D.; Zhu, X.-Y., Large Polarons in Lead Halide Perovskites. *Sci. Adv.* **2017**, *3*.

16. Yettapu, G. R.; Talukdar, D.; Sarkar, S.; Swarnkar, A.; Nag, A.; Ghosh, P.; Mandal, P., Terahertz Conductivity within Colloidal Cspbbr3 Perovskite Nanocrystals: Remarkably High Carrier Mobilities and Large Diffusion Lengths. *Nano Lett.* **2016**, *16*, 4838-4848.

17. Kennedy, C. L.; Hill, A. H.; Grumstrup, E. M., Screening Links Transport and Recombination Mechanisms in Lead Halide Perovskites. *J. Phys. Chem. C* **2019**, *123*, 15827-15833.

18. Zhang, H.; Liu, X.; Dong, J.; Yu, H.; Zhou, C.; Zhang, B.; Xu, Y.; Jie, W., Centimeter-Sized Inorganic Lead Halide Perovskite Cspbbr3 Crystals Grown by an Improved Solution Method. *Cryst. Growth Des.* **2017**, *17*, 6426-6431.

19. Miyata, K.; Meggiolaro, D.; Trinh, M. T.; Joshi, P. P.; Mosconi, E.; Jones, S. C.; Angelis, F. D.; Zhu1, X.-Y., Large Polarons in Lead Halide Perovskites. *Sci. Adv.* **2017**, *3*.

20. Jones, A. C.; Kearns, N. M.; Ho, J. J.; Flach, J. T.; Zanni, M. T., Impact of Non-Equilibrium Molecular Packings on Singlet Fission in Microcrystals Observed Using 2d White-Light Microscopy. *Nat. Chem.* **2020**, *12*, 40-47.

21. Wong, C. Y.; Cotts, B. L.; Wu, H.; Ginsberg, N. S., Exciton Dynamics Reveal Aggregates with Intermolecular Order at Hidden Interfaces in Solution-Cast Organic Semiconducting Films. *Nat. Commun.* **2015**, *6*, 5946.

22. Bush, K. A., et al., Controlling Thin-Film Stress and Wrinkling During Perovskite Film Formation. *ACS Energy Lett.* **2018**, *3*, 1225-1232.

23. Zhu, C., et al., Strain Engineering in Perovskite Solar Cells and Its Impacts on Carrier Dynamics. *Nat. Commun.* **2019**, *10*, 815.

24. Lee, H.; Gaiaschi, S.; Chapon, P.; Tondelier, D.; Bourée, J.-E.; Bonnassieux, Y.; Derycke, V.; Geffroy, B., Effect of Halide Ion Migration on the Electrical Properties of

Methylammonium Lead Tri-Iodide Perovskite Solar Cells. *J. Phys. Chem. C* **2019**, *123*, 17728-17734.

25. Abdi-Jalebi, M., et al., Maximizing and Stabilizing Luminescence from Halide Perovskites with Potassium Passivation. *Nature* **2018**, *555*, 497-501.

26. Rehman, W.; Milot, R. L.; Eperon, G. E.; Wehrenfennig, C.; Boland, J. L.; Snaith, H. J.; Johnston, M. B.; Herz, L. M., Charge-Carrier Dynamics and Mobilities in Formamidinium Lead Mixed-Halide Perovskites. *Adv. Mater.* **2015**, *27*, 7938-44.

27. Grumstrup, E. M.; Gabriel, M. M.; Pinion, C. W.; Parker, J. K.; Cahoon, J. F.; Papanikolas, J. M., Reversible Strain-Induced Electron-Hole Recombination in Silicon Nanowires Observed with Femtosecond Pump-Probe Microscopy. *Nano Lett.* **2014**, *14*, 6287-92.

28. Folie, B. D., et al., Effect of Anisotropic Confinement on Electronic Structure and Dynamics of Band Edge Excitons in Inorganic Perovskite Nanowires. *J. Phys. Chem. A* **2020**.

29. Guo, Z.; Zhou, N.; Williams, O. F.; Hu, J.; You, W.; Moran, A. M., Imaging Carrier Diffusion in Perovskites with a Diffractive Optic-Based Transient Absorption Microscope. *J. Phys. Chem. C* **2018**, *122*, 10650-10656.

30. Watthage, S. C.; Song, Z.; Phillips, A. B.; Heben, M. J., Evolution of Perovskite Solar Cells. In *Perovskite Photovoltaics*, 2018; pp 43-88.

31. Peña, M. A.; Fierro, J. L. G., Chemical Structures and Performances of Perovskite Oxides. *Chem. Rev.* **2001**, *101*, 1981-2017.

32. Ha, S. T.; Su, R.; Xing, J.; Zhang, Q.; Xiong, Q., Metal Halide Perovskite Nanomaterials: Synthesis and Applications. *Chem. Sci.* **2017**, *8*, 2522-2536.

33. Park, H.; Mall, R.; Alharbi, F. H.; Sanvito, S.; Tabet, N.; Bensmail, H.; El-Mellouhi, F., Learn-and-Match Molecular Cations for Perovskites. *J. Phys. Chem. A* **2019**, *123*, 7323-7334.

34. Li, C.; Lu, X.; Ding, W.; Feng, L.; Gao, Y.; Guo, Z., Formability of Abx3 (X = F, Cl, Br, I) Halide Perovskites. *Acta. Crystallogr. B* **2008**, *64*, 702-7.

35. Ji, D.; Feng, S.; Wang, L.; Wang, S.; Na, M.; Zhang, H.; Zhang, C.; Li, X., Regulatory Tolerance and Octahedral Factors by Using Vacancy in Apbi3 Perovskites. *Vacuum* **2019**, *164*, 186-193.

36. McKinnon, N. K.; Reeves, D. C.; Akabas, M. H., 5-Ht3 Receptor Ion Size Selectivity Is a Property of the Transmembrane Channel, Not the Cytoplasmic Vestibule Portals. *J. Gen. Physiol.* **2011**, *138*, 453-66.

37. Green, M. A.; Ho-Baillie, A.; Snaith, H. J., The Emergence of Perovskite Solar Cells. *Nat. Photonics* **2014**, *8*, 506-514.

38. Li, Z.; Yang, M.; Park, J.-S.; Wei, S.-H.; Berry, J. J.; Zhu, K., Stabilizing Perovskite Structures by Tuning Tolerance Factor: Formation of Formamidinium and Cesium Lead Iodide Solid-State Alloys. *Chem. Mater.* **2015**, *28*, 284-292.

39. Prasanna, R.; Gold-Parker, A.; Leijtens, T.; Conings, B.; Babayigit, A.; Boyen, H. G.; Toney, M. F.; McGehee, M. D., Band Gap Tuning Via Lattice Contraction and Octahedral Tilting in Perovskite Materials for Photovoltaics. *J. Am. Chem. Soc.* **2017**, *139*, 11117-11124.

40. Fan, Z.; Sun, K.; Wang, J., Perovskites for Photovoltaics: A Combined Review of Organic–Inorganic Halide Perovskites and Ferroelectric Oxide Perovskites. *J. Mater. Chem. A* **2015**, *3*, 18809-18828.

41. Tao, S.; Schmidt, I.; Brocks, G.; Jiang, J.; Tranca, I.; Meerholz, K.; Olthof, S., Absolute Energy Level Positions in Tin- and Lead-Based Halide Perovskites. *Nat. Commun.* **2019**, *10*, 2560.

42. Lee, J.-H.; Bristowe, N. C.; Lee, J. H.; Lee, S.-H.; Bristowe, P. D.; Cheetham, A. K.; Jang, H. M., Resolving the Physical Origin of Octahedral Tilting in Halide Perovskites. *Chem. Mater.* **2016**, *28*, 4259-4266.

43. Jiang, Q.; Zhao, Y.; Zhang, X.; Yang, X.; Chen, Y.; Chu, Z.; Ye, Q.; Li, X.; Yin, Z.; You, J., Surface Passivation of Perovskite Film for Efficient Solar Cells. *Nat. Photonics* **2019**, *13*, 460-466.

44. Extance, A., Perovskites on Trial. *Nature* **2019**, *570*, 429-432.

45. Li, W.; Yadavalli, S. K.; Lizarazo-Ferro, D.; Chen, M.; Zhou, Y.; Padture, N. P.; Zia, R., Subgrain Special Boundaries in Halide Perovskite Thin Films Restrict Carrier Diffusion. *ACS Energy Lett.* **2018**, *3*, 2669-2670.

46. Akin, S.; Arora, N.; Zakeeruddin, S. M.; Grätzel, M.; Friend, R. H.; Dar, M. I., New Strategies for Defect Passivation in High-Efficiency Perovskite Solar Cells. *Adv. Energy Mater.* **2019**.

47. Huang, L.; Cheng, J.-X., Nonlinear Optical Microscopy of Single Nanostructures. *Annu. Rev. Mater. Res.* **2013**, *43*, 213-236.

48. Bennett, B. R.; Soref, R. A.; Alamo, J. A. D., Carrier-Induced Changes in Refractive Index of Inp, Gaas, and Ingaasp. *IEEE J. Quantum Electron.* **1990**, *26*, 113-122.

49. Waxler, R. M.; Cleek, G. W., The Effect of Temperature and Pressure on the Refractive Index of Some Oxide Glasses. *J. Res. Natl. Inst. Stand. Technol.* **1973**, *77A*, 755-763.

50. Yu, Z. G.; Krishnamurthy, S., Photoexcited-Carrier-Induced Refractive Index Change in Small Bandgap Semiconductors. *J. Opt. Soc. Am.* **2006**, *23*, 2356-2360.

51. Esser, A.; Kütt, W.; Strahnen, M.; Maidorn, G.; Kurz, H., Femtosecond Transient Reflectivity Measurements as a Probe for Process-Induced Defects in Silicon. *Appl. Surf. Sci.* **1990**, *46*, 446-450.

52. Sabbah, A. J.; Riffe, D. M., Femtosecond Pump-Probe Reflectivity Study of Silicon Carrier Dynamics. *Phys. Rev. B* **2002**, *66*, 165217.

53. Lundstrom, M., *Fundamentals of Carrier Transport*; Cambridge University Press: Cambridge, 2000.

54. Elliot, R. J.; Gibson, A. F., *An Introduction to Solid State Physics and Its Applications*; The Macmillan Press Ltd.: United Kingdom, 1974.

55. Elliot, R. J., Intensity of Optical Absorption by Excitons. *Phys. Rev.* **1957**, *108*, 1384-1389.

56. Sabbah, A. J.; Riffe, D. M., Measurement of Silicon Surface Recombination Velocity Using Ultrafast Pump–Probe Reflectivity in the near Infrared. *J. Appl. Phys.* **2000**, *88*, 6954-6956.

57. La, O. V. C., et al., Elucidating the Role of Disorder and Free-Carrier Recombination Kinetics in Ch3nh3pbi3 Perovskite Films. *Nat. Commun.* **2015**, *6*.

58. Leijtens, T.; Eperon, G. E.; Barker, A. J.; Grancini, G.; Zhang, W.; Ball, J. M.; Kandada, A. R. S.; Snaith, H. J.; Petrozza, A., Carrier Trapping and Recombination: The Role of Defect Physics in Enhancing the Open Circuit Voltage of Metal Halide Perovskite Solar Cells. *Energy Environ. Sci.* **2016**, *9*, 3472-3481.

59. Cating, E. E. M.; Pinion, C. W.; Christesen, J. D.; Christie, C. A.; Grumstrup, E. M.; Cahoon, J. F.; Papanikolas, J. M., Probing Intrawire, Interwire, and Diameter-Dependent Variations in Silicon Nanowire Surface Trap Density with Pump-Probe Microscopy. *Nano Lett.* **2017**, *17*, 5956-5961.

60. Steinfeld, J. I.; Francisco, J. S.; Hase, W. L., *Chemical Kinetics and Dynamics*, Second ed.; Prentice-Hall: Upper Saddle River, NJ, 1998.

61. Landsberg, P. T., *Recombination in Semiconductors*; Cambridge University Press: Cambridge, U.K., 1991.

62. Ginsberg, N. S.; Tisdale, W. A., Spatially Resolved Exciton and Charge Transport in Emerging Semiconductors. *Annu. Rev. Phys. Chem.* **2019**.

63. Stoumpos, C. C.; Kanatzidis, M. G., Halide Perovskites: Poor Man's High-Performance Semiconductors. *Adv. Mater.* **2016**, *28*, 5778-93.

64. Green, M. A.; Emery, K.; Hishikawa, Y.; Warta, W.; Dunlop, E. D., Solar Cell Efficiency Tables (Version 48). *Prog. Photovolt.* **2016**, *24*, 905-913.

65. Beal, R. E.; Slotcavage, D. J.; Leijtens, T.; Bowring, A. R.; Belisle, R. A.; Nguyen, W. H.; Burkhard, G. F.; Hoke, E. T.; McGehee, M. D., Cesium Lead Halide Perovskites with Improved Stability for Tandem Solar Cells. *J. Phys. Chem. Lett.* **2016**, *7*, 746-51.

66. Ramasamy, P.; Lim, D. H.; Kim, B.; Lee, S. H.; Lee, M. S.; Lee, J. S., All-Inorganic Cesium Lead Halide Perovskite Nanocrystals for Photodetector Applications. *Chem. Commun.* **2016**, *52*, 2067-70.

67. Lignos, I.; Stavrakis, S.; Nedelcu, G.; Protesescu, L.; deMello, A. J.; Kovalenko, M. V., Synthesis of Cesium Lead Halide Perovskite Nanocrystals in a Droplet-Based Microfluidic Platform: Fast Parametric Space Mapping. *Nano Lett.* **2016**, *16*, 1869-77.

68. Slotcavage, D. J.; Karunadasa, H. I.; McGehee, M. D., Light-Induced Phase Segregation in Halide-Perovskite Absorbers. *ACS Energy Lett.* **2016**, *1*, 1199-1205.

69. Sutton, R. J., et al., Bandgap-Tunable Cesium Lead Halide Perovskites with High Thermal Stability for Efficient Solar Cells. *Adv. Energy Mater.* **2016**, *6*.

70. Berdiyorov, G. R.; Kachmar, A.; El-Mellouhi, F.; Carignano, M. A.; El-Amine Madjet, M., Role of Cations on the Electronic Transport and Optical Properties of Lead-Iodide Perovskites. *J. Phys. Chem. C* **2016**, *120*, 16259-16270.

71. Makarov, N. S.; Guo, S.; Isaienko, O.; Liu, W.; Robel, I.; Klimov, V. I., Spectral and Dynamical Properties of Single Excitons, Biexcitons, and Trions in Cesium-Lead-Halide Perovskite Quantum Dots. *Nano Lett.* **2016**, *16*, 2349-2362.

72. Swarnkar, A.; Marshall, A. R.; Sanehira, E. M.; Chernomordik, B. D.; Moore, D. T.; Christians, J. A.; Chakrabarti, T.; Luther, J. M., Quantum Dot–Induced Phase Stabilization of a-Cspbi3 Perovskite for High-Efficiency Photovoltaics. *Science* **2016**, *354*, 92-95.

73. Yang, Y.; Yang, M.; Li, Z.; Crisp, R.; Zhu, K.; Beard, M. C., Comparison of Recombination Dynamics in Ch3nh3pbbr3 and Ch3nh3pbi3 Perovskite Films: Influence of Exciton Binding Energy. *J. Phys. Chem. Lett.* **2015**, *6*, 4688-4692.

74. Saba, M., et al., Correlated Electron-Hole Plasma in Organometal Perovskites. *Nat. Commun.* **2014**, *5*, 5049.

75. Klingshirn, C. F., *Semiconductor Optics*, 4th ed.; Springer: New York, 2012.

76. Kalt, H.; Hetterich, M., *Optics of Semiconductors and Their Nanostructures*, 1st ed.; Springer-Verlag: Berlin, 2004; Vol. 146.

77. Stoumpos, C. C., et al., Crystal Growth of the Perovskite Semiconductor Cspbbr3: A New Material for High-Energy Radiation Detection. *Cryst. Growth Des.* **2013**, *13*, 2722-2727.

78. Stewart, R. J.; Grieco, C.; Larsen, A. V.; Maier, J. J.; Asbury, J. B., Approaching Bulk Carrier Dynamics in Organo-Halide Perovskite Nanocrystalline Films by Surface Passivation. *J. Phys. Chem. Lett.* **2016**, *7*, 1148-53.

79. Manser, J. S.; Kamat, P. V., Band Filling with Free Charge Carriers in Organometal Halide Perovskites. *Nat. Photonics* **2014**, *8*, 737-743.

80. Zhu, H.; Fu, Y.; Meng, F.; Wu, X.; Gong, Z.; Ding, Q.; Gustafsson, M. V.; Trinh, M. T.; Jin, S.; Zhu, X. Y., Lead Halide Perovskite Nanowire Lasers with Low Lasing Thresholds and High Quality Factors. *Nat. Mater.* **2015**, *14*, 636-42.

81. Milot, R. L.; Eperon, G. E.; Snaith, H. J.; Johnston, M. B.; Herz, L. M., Temperature-Dependent Charge-Carrier Dynamics in Ch3nh3pbi3perovskite Thin Films. *Adv. Funct. Mater.* **2015**, *25*, 6218-6227.

82. Wang, H.; Whittaker-Brooks, L.; Fleming, G. R., Exciton and Free Charge Dynamics of Methylammonium Lead Iodide Perovskites Are Different in the Tetragonal and Orthorhombic Phases. *J. Phys. Chem. C* **2015**, *119*, 19590-19595.

83. Hutter, E. M.; Gelvez-Rueda, M. C.; Osherov, A.; Bulovic, V.; Grozema, F. C.; Stranks, S. D.; Savenije, T. J., Direct-Indirect Character of the Bandgap in Methylammonium Lead Iodide Perovskite. *Nat. Mater.* **2017**, *16*, 115-120.

84. Zhu, H.; Miyata, K.; Fu, Y.; Wang, J.; Joshi, P. P.; Niesner, D.; Williams, K. W.; Jin, S.; Zhu, X.-Y., Screening in Crystalline Liquids Protects Energetic Carriers in Hybrid Perovskites. *Science* **2016**, *353*, 1409-1413.

85. Hill, A. H.; Smyser, K. E.; Kennedy, C. L.; Massaro, E. S.; Grumstrup, E. M., Screened Charge Carrier Transport in Methylammonium Lead Iodide Perovskite Thin Films. *J. Phys. Chem. Lett.* **2017**, *8*, 948-953.

86. Akiyama, H.; Matsusue, T.; Sakaki, H., Carrier Scattering and Excitonic Effects on Electron-Hole-Pair Diffusion in Nondoped and P-Type-Modulation-Doped Gaas/Alxga1-X as Quantum-Well Structures. *Phys. Rev. B* **1994**, *49*, 14523-14530.

87. Ruzicka, B. A.; Zhao, H., Optical Studies of Ballistic Currents in Semiconductors. *Opt. Soc. Am. B* **2012**, *29*, A43−A54.

88. Tiedje, T.; Cebulka, J. M.; Morel, D. L.; Abeles, B., Evidence for Exponential Band Tails in Amorphous Silicon Hydride. *Phys. Rev. Lett.* **1981**, *46*, 1425-1428.

89. Park, N.-G.; Grätzel, M.; Miyasaka, T.; Zhu, K.; Emery, K., Towards Stable and Commercially Available Perovskite Solar Cells. *Nat. Energy* **2016**, *1*.

90. Stranks, S. D.; Snaith, H. J., Metal-Halide Perovskites for Photovoltaic and Light-Emitting Devices. *Nat. Nanotechnol.* **2015**, *10*, 391-402.

91. Ansari, M. I. H.; Qurashi, A.; Nazeeruddin, M. K., Frontiers, Opportunities, and Challenges in Perovskite Solar Cells: A Critical Review. *J. Photoch. Photobio. C* **2018**, *35*, 1-24.

92. Egger, D. A.; Bera, A.; Cahen, D.; Hodes, G.; Kirchartz, T.; Kronik, L.; Lovrincic, R.; Rappe, A. M.; Reichman, D. R.; Yaffe, O., What Remains Unexplained About the Properties of Halide Perovskites? *Adv. Mater.* **2018**, *30*, 1800691.

93. Gallop, N. P.; Selig, O.; Giubertoni, G.; Bakker, H. J.; Rezus, Y. L. A.; Frost, J. M.; Jansen, T. L. C.; Lovrincic, R.; Bakulin, A. A., Rotational Cation Dynamics in Metal Halide Perovskites: Effect on Phonons and Material Properties. *J. Phys. Chem. Lett.* **2018**, *9*, 5987-5997.

94. Richter, J. M.; Branchi, F.; Valduga de Almeida Camargo, F.; Zhao, B.; Friend, R. H.; Cerullo, G.; Deschler, F., Ultrafast Carrier Thermalization in Lead Iodide Perovskite Probed with Two-Dimensional Electronic Spectroscopy. *Nat. Commun.* **2017**, *8*.

95. Heiderhoff, R.; Haeger, T.; Pourdavoud, N.; Hu, T.; Al-Khafaji, M.; Mayer, A.; Chen, Y.; Scheer, H.-C.; Riedl, T., Thermal Conductivity of Methylammonium Lead Halide Perovskite Single Crystals and Thin Films: A Comparative Study. *J. Phys. Chem. C* **2017**, *121*, 28306-28311.

96. Ferry, D. K., *Semiconductors*; Macmillan Publishing Company: New York, NY, 1991.

97. Lin, Q.; Armin, A.; Nagiri, R. C. R.; Burn, P. L.; Meredith, P., Electro-Optics of Perovskite Solar Cells. *Nat. Photonics* **2014**, *9*, 106-112.

98. Jonscher, A. K., Dielectric Relaxation in Solids. *J. Phys. D: Appl. Phys.* **1999**, *32*.

99. Brivio, F.; Frost, J. M.; Skelton, J. M.; Jackson, A. J.; Weber, O. J.; Weller, M. T.; Goñi, A. R.; Leguy, A. M. A.; Barnes, P. R. F.; Walsh, A., Lattice Dynamics and

Vibrational Spectra of the Orthorhombic, Tetragonal, and Cubic Phases of Methylammonium Lead Iodide. *Phys. Rev. B.* **2015**, *92*, 144308.

100. Hill, A. H.; Kennedy, C. L.; Massaro, E. S.; Grumstrup, E. M., Perovskite Carrier Transport: Disentangling the Impacts of Effective Mass and Scattering Time through Microscopic Optical Detection. *J. Phys. Chem. Lett.* **2018**, *9*, 2808-2813.

101. Kennedy, C. L.; Hill, A. H.; Massaro, E. S.; Grumstrup, E. M., Ultrafast Excited-State Transport and Decay Dynamics in Cesium Lead Mixed Halide Perovskites. *ACS Energy Lett.* **2017**, *2*, 1501-1506.

102. Bennett, B. R.; Soref, R. A.; Alamo, J. A. D., Carrier-Induced Change in Refractive Index of Inp, Gaas, and Ingaasp. *IEEE J. Quantum Electron.* **1990**, *26*, 113-121.

103. Li, C.-M.; Sjodin, T.; Dai, H.-L., Photoexcited Carrier Diffusion near a Si□(111) Surface: Non-Negligible Consequence of Carrier-Carrier Scattering. *Phys. Rev. B* **1997**, *56*, 15252-15255.

104. Maji, P.; Ray, A.; Sadhukhan, P.; Chatterjee, S.; Das, S., Study on Charge Transfer Mechanism and Dielectric Relaxation of Cesium Lead Bromide (Cspbbr3). *J. Appl. Phys.* **2018**, *124*, 124102.

105. Anusca, I., et al., Dielectric Response: Answer to Many Questions in the Methylammonium Lead Halide Solar Cell Absorbers. *Adv. Energy Mater.* **2017**, *7*, 1700600.

106. Poglitsch, A.; Weber, D., Dynamic Disorder in Methylammoniumtrihalogenoplumbates (Ii) Observed by Millimeter-Wave Spectroscopy. *J. Chem. Phys.* **1987**, *87*, 6373-6378.

107. Guo, Z.; Wan, Y.; Yang, M.; Snaider, J.; Zhu, K.; Huang, L., Long-Range Hot-Carrier Transport in Hybrid Perovskites Visualized by Ultrafast Microscopy. *Science* **2017**, 59-62.

108. Bush, K. A., et al., Controlling Thin-Film Stress and Wrinkling During Perovskite Film Formation. *ACS Energy Lett.* **2018**, *3*, 1225-1232.

109. Sharenko, A.; Toney, M. F., Relationships between Lead Halide Perovskite Thin-Film Fabrication, Morphology, and Performance in Solar Cells. *J. Am. Chem. Soc.* **2016**, *138*, 463-70.

110. Lee, H.; Jyothi, C.; Baang, S.; Kwon, J.-H.; Bae, J.-H., Influence of Structural Defects in Solution-Processed Inzno Semiconductors on the Electrical Stability of Thin-Film Transistors. *J. Korean Phys. Soc.* **2016**, *69*, 1688-1693.

111. Yuan, Y.; Giri, G.; Ayzner, A. L.; Zoombelt, A. P.; Mannsfeld, S. C.; Chen, J.; Nordlund, D.; Toney, M. F.; Huang, J.; Bao, Z., Ultra-High Mobility Transparent Organic Thin Film Transistors Grown by an Off-Centre Spin-Coating Method. *Nat. Commun.* **2014**, *5*, 3005.

112. Hawash, Z.; Ono, L. K.; Raga, S. R.; Lee, M. V.; Qi, Y., Air-Exposure Induced Dopant Redistribution and Energy Level Shifts in Spin-Coated Spiro-Meotad Films. *Chem. Mater.* **2015**, *27*, 562-569.

113. Zhu, C., et al., Strain Engineering in Perovskite Solar Cells and Its Impacts on Carrier Dynamics. *Nat. Commun.* **2019**, *10*, 815.

114. Kennedy, C. L.; Hill, A. H.; Grumstrup, E. M., Screening Links Transport and Recombination Mechanisms in Lead Halide Perovskites. *J. Phys. Chem. C* **2019**, *123*, 15827-15833.

115. Arias, D. H.; Moore, D. T.; van de Lagemaat, J.; Johnson, J. C., Direct Measurements of Carrier Transport in Polycrystalline Methylammonium Lead Iodide Perovskite Films with Transient Grating Spectroscopy. *J. Phys. Chem. Lett.* **2018**, *9*, 5710-5717.

116. Ščajev, P.; Aleksiejūnas, R.; Terakawa, S.; Qin, C.; Fujihara, T.; Matsushima, T.; Adachi, C.; Juršėnas, S., Anisotropy of Thermal Diffusivity in Lead Halide Perovskite Layers Revealed by Thermal Grating Technique. *J. Phys. Chem. C* **2019**, *123*, 14914-14920.

117. Rehman, W.; McMeekin, D. P.; Patel, J. B.; Milot, R. L.; Johnston, M. B.; Snaith, H. J.; Herz, L. M., Photovoltaic Mixed-Cation Lead Mixed-Halide Perovskites: Links between Crystallinity, Photo-Stability and Electronic Properties. *Energy Environ. Sci.* **2017**, *10*, 361-369.

118. Jiang, X.; Hoffman, J.; Stoumpos, C. C.; Kanatzidis, M. G.; Harel, E., Transient Sub-Band-Gap States at Grain Boundaries of Ch3nh3pbi3 Perovskite Act as Fast Temperature Relaxation Centers. *ACS Energy Lett.* **2019**, *4*, 1741-1747.

119. Snaider, J. M.; Guo, Z.; Wang, T.; Yang, M.; Yuan, L.; Zhu, K.; Huang, L., Ultrafast Imaging of Carrier Transport across Grain Boundaries in Hybrid Perovskite Thin Films. *ACS Energy Lett.* **2018**, *3*, 1402-1408.

120. Delor, M.; Weaver, H. L.; Yu, Q.; Ginsberg, N. S., Imaging Material Functionality through Three-Dimensional Nanoscale Tracking of Energy Flow. *Nat. Mater.* **2020**, *19*, 56-62.

121. Jones, T. W., et al., Lattice Strain Causes Non-Radiative Losses in Halide Perovskites. *Energy Environ. Sci.* **2019**, *12*, 596-606.

122. Kennedy, C. L.; Hill, A. H.; Massaro, E. S.; Grumstrup, E. M., Ultrafast Excited-State Transport and Decay Dynamics in Cesium Lead Mixed Halide Perovskites. *ACS Energy Lett.* **2017**, *2*, 1501-1506.

123. Born, M.; Wolf, E., *Principles of Optics: Electromagnetic Theory of Propagation, Interference and Diffraction of Light* 4th ed.; Pergamon Press: Oxford, 1970.

124. Hickey, C. L.; Grumstrup, E. M., A Reduced Artifact Approach for Determining Diffusion Coefficients in Time-Resolved Microscopy. *J. Phys. Chem. C* **2020**, *submitted for publication*.

125. Britton, T. B.; Jiang, J.; Guo, Y.; Vilalta-Clemente, A.; Wallis, D.; Hansen, L. N.; Winkelmann, A.; Wilkinson, A. J., Tutorial: Crystal Orientations and Ebsd — or Which Way Is Up? *Mater. Charact.* **2016**, *117*, 113-126.

126. Wright, S. I.; Nowell, M. M., Ebsd Image Quality Mapping. *Microsc. Microanal* **2006**, *12*, 72-84.

127. Wu, J.; Wray, P. J.; Garcia, C. I.; Hua, M.; Deardo, A. J., Image Quality Analysis: A New Method of Characterizing Microstructures. *ISIJ Int.* **2005**, *45*, 254-262.

128. Wright, S. I.; Nowell, M. M.; Field, D. P., A Review of Strain Analysis Using Electron Backscatter Diffraction. *Microsc. Microanal* **2011**, *17*, 316-29.

129. Tao, X.; Eades, A., Errors, Artifacts, and Improvements in Ebsd Processing and Mapping. *Microsc. Microanal* **2005**, *11*, 79-87.

130. Deans, S. R., Hough Transform from the Radon Transform. *IEEE T. Pattern Anal* **1981**, *PAMI-3*, 185-188.

131. Brand, V.; Levi, K.; McGehee, M. D.; Dauskardt, R. H., Film Stresses and Electrode Buckling in Organic Solar Cells. *Sol. Energy Mater. Sol. Cells* **2012**, *103*, 80-85.

132. Zhao, J.; Deng, Y.; Wei, H.; Zheng, X.; Yu, Z.; Shao, Y.; Shield, J. E.; Huang, J., Strained Hybrid Perovskite Thin Films and Their Impact on the Intrinsic Stability of Perovskite Solar Cells. *Sci. Adv.* **2017**, *3*.

133. Ball, J. M.; Petrozza, A., Defects in Perovskite-Halides and Their Effects in Solar Cells. *Nat. Energy* **2016**, *1*.

134. Quiros, M.; Grazulis, S.; Girdzijauskaite, S.; Merkys, A.; Vaitkus, A., Using Smiles Strings for the Description of Chemical Connectivity in the Crystallography Open Database. *J. Cheminformatics* **2018**, *10*, 23.

135. Grazulis, S.; Chateigner, D.; Downs, R. T.; Yokochi, A. F.; Quiros, M.; Lutterotti, L.; Manakova, E.; Butkus, J.; Moeck, P.; Le Bail, A., Crystallography Open Database - an Open-Access Collection of Crystal Structures. *J. Appl. Crystallogr.* **2009**, *42*, 726-729.

136. Grazulis, S.; Daskevic, A.; Merkys, A.; Chateigner, D.; Lutterotti, L.; Quiros, M.; Serebryanaya, N. R.; Moeck, P.; Downs, R. T.; Le Bail, A., Crystallography Open Database (Cod): An Open-Access Collection of Crystal Structures and Platform for World-Wide Collaboration. *Nucleic Acids Res.* **2012**, *40*, D420-7.

137. Grazulis, S.; Merkys, A.; Vaitkus, A.; Okulic-Kazarinas, M., Computing Stoichiometric Molecular Composition from Crystal Structures. *J. Appl. Crystallogr.* **2015**, *48*, 85-91.

138. Merkys, A.; Vaitkus, A.; Butkus, J.; Okulic-Kazarinas, M.; Kairys, V.; Grazulis, S., Cod::Cif::Parser: An Error-Correcting Cif Parser for the Perl Language. *J. Appl. Crystallogr.* **2016**, *49*, 292-301.

139. Downs, R. T. H.-W., M., The American Mineralogist Crystal Structure Database. *Am. Mineral* **2003**, *88*, 247-250.

140. Rodova, M.; Brozek, J.; Knizek, K.; Nitsch, K., Phase Transitions in Ternary Caesium Lead Bromide. *J. Therm. Anal. Calorim.* **2003**, *71*, 667-673.

141. Mehl, B. P.; Kirschbrown, J. R.; Gabriel, M. M.; House, R. L.; Papanikolas, J. M., Pump-Probe Microscopy: Spatially Resolved Carrier Dynamics in Zno Rods and the Influence of Optical Cavity Resonator Modes. *J. Phys. Chem. B* **2013**, *117*, 4390-8.

142. Yuan, L.; Chung, T.-F.; Kuc, A.; Wan, Y.; Xu, Y.; Chen, T. P.; Heine, T.; Huang, L., Photocarrier Generation from Interlayer Charge-Transfer Transitions in Ws2-Graphene Heterostructures. *Sci. Adv.* **2018**, *4*, 1-9.

143. Rozenman, G. G.; Akulov, K.; Golombek, A.; Schwartz, T., Long-Range Transport of Organic Exciton-Polaritons Revealed by Ultrafast Microscopy. *ACS Photonics* **2017**, *5*, 105-110.

144. Grumstrup, E. M.; Gabriel, M. M.; Cating, E. E. M.; Van Goethem, E. M.; Papanikolas, J. M., Pump–Probe Microscopy: Visualization and Spectroscopy of Ultrafast Dynamics at the Nanoscale. *Chem. Phys.* **2015**, *458*, 30-40.

145. Zhu, T.; Snaider, J. M.; Yuan, L.; Huang, L., Ultrafast Dynamic Microscopy of Carrier and Exciton Transport. *Annu Rev Phys Chem* **2019**, *70*, 219-244.

146. Zhu, Y.; Cheng, J.-X., Transient Absorption Microscopy: Technological Innovations and Applications in Materials Science and Life Science. *The Journal of Chemical Physics* **2020**, *152*.

147. Grosse, S.; Arnold, R.; vonPlessen, G.; Koch, M.; Feldmann, J.; Axt, V. M.; Kuhn, T.; Rettig, R.; Stolz, W., Relaxation Dynamics of Electron-Hole Pairs Studied by Spatiotemporal Pump and Probe Experiments. *Phys Status Solidi B* **1997**, *204*, 147-150.

148. Yoon, H. W.; Wake, D. R.; Wolfe, J. P.; Morkoc, H., In-Plane Transport of Photoexcited Carriers in Gaas Quantum Wells. *Phys Rev B Condens Matter* **1992**, *46*, 13461-13470.

149. Ruzicka, B. A.; Werake, L. K.; Samassekou, H.; Zhao, H., Ambipolar Diffusion of Photoexcited Carriers in Bulk Gaas. *Applied Physics Letters* **2010**, *97*.

150. Akselrod, G. M.; Prins, F.; Poulikakos, L. V.; Lee, E. M.; Weidman, M. C.; Mork, A. J.; Willard, A. P.; Bulovic, V.; Tisdale, W. A., Subdiffusive Exciton Transport in Quantum Dot Solids. *Nano Lett* **2014**, *14*, 3556-62.

151. Sung, J., et al., Long-Range Ballistic Propagation of Carriers in Methylammonium Lead Iodide Perovskite Thin Films. *Nature Physics* **2019**, *16*, 171-176.

152. Lo, S. S.; Shi, H. Y.; Huang, L. B.; Hartland, G. V., Imaging the Extent of Plasmon Excitation in Au Nanowires Using Pump-Probe Microscopy. *Opt Lett* **2013**, *38*, 1265-1267.

153. Van Goethem, E. M.; Pinion, C. W.; Cating, E. E. M.; Cahoon, J. F.; Papanikolas, J. M., Observation of Phonon Propagation in Germanium Nanowires Using Femtosecond Pump–Probe Microscopy. *ACS Photonics* **2019**, *6*, 2213-2222.

154. Snaider, J. M.; Guo, Z.; Wang, T.; Yang, M.; Yuan, L.; Zhu, K.; Huang, L., Ultrafast Imaging of Carrier Transport across Grain Boundaries in Hybrid Perovskite Thin Films. *ACS Energy Lett.* **2018**, *3*, 1402-1408.

155. Xu, S.; Guo, W.; Du, S.; Loy, M. M.; Wang, N., Piezotronic Effects on the Optical Properties of Zno Nanowires. *Nano Lett.* **2012**, *12*, 5802-7.

156. Gu, M., *Advanced Optical Imaging Theory*; Springer-Verlag Berlin Heidelberg, 2000.

157. Matthews, J.; Walker, R. L., *Mathematical Methods of Physics*, 2 ed.; W.A. Benjamin, Inc.: New York, 1970.

158. Grumstrup, E. M., Spatiotemporal Coupling of Excited State Dynamics in Time-Resolved Microscopies. *Opt Express* **2019**, *27*, 31385 - 31393.

159. Fu, X., et al., Exciton Drift in Semiconductors under Uniform Strain Gradients: Application to Bent Zno Microwires. *ACS nano* **2014**, *8*, 3412-20.

160. Sun, L.; Kim do, H.; Oh, K. H.; Agarwal, R., Strain-Induced Large Exciton Energy Shifts in Buckled Cds Nanowires. *Nano Lett* **2013**, *13*, 3836-42.

161. Ahmad, W.; Khan, J.; Niu, G.; Tang, J., Inorganic Cspbi3perovskite-Based Solar Cells: A Choice for a Tandem Device. *Sol. RRL* **2017**, *1*.

162. Makowski, L.; Glicksman, M., Disorder Scattering in Solid Solutions Iii-V Semiconducting Compounds. *J. Phys. Chem. Solids.* **1973**, *34*, 487-492.

163. Li, H.; Harrison, P.; Wu, J.; Yao, H., Probing the Correlation of Twin Boundaries and Charge Transport of Cdte Solar Cells Using Electron Backscattering Diffraction and Conductive Atomic Force Microscopy. *ACS Appl. Energy Mater.* **2018**, *1*, 3646-3653.

164. Murr, L. E., Planar Defects: Crystal Interfaces. In *Handbook of Materials Structures, Properties, Processing and Performance*, Springer International Publishing: Switzerland, 2015; pp 273-312.

165. Yang, Z., et al., Impact of the Halide Cage on the Electronic Properties of Fully Inorganic Cesium Lead Halide Perovskites. *ACS Energy Lett.* **2017**, *2*, 1621-1627.

166. Kang, Y.; Han, S., Intrinsic Carrier Mobility of Cesium Lead Halide Perovskites. *Phys. Rev. Appl.* **2018**, *10*, 044013.

167. Mosconi, E.; Umari, P.; De Angelis, F., Electronic and Optical Properties of Mapbx3 Perovskites (X = I, Br, Cl): A Unified Dft and Gw Theoretical Analysis. *Phys. Chem.* **2016**, *18*, 27158-27164.

168. Galkowski, K., et al., Determination of the Exciton Binding Energy and Effective Masses for Methylammonium and Formamidinium Lead Tri-Halide Perovskite Semiconductors. *Energy Environ. Sci.* **2016**, *9*, 962-970.

169. Giorgi, G.; Fujisawa, J.; Segawa, H.; Yamashita, K., Small Photocarrier Effective Masses Featuring Ambipolar Transport in Methylammonium Lead Iodide Perovskite: A Density Functional Analysis. *J. Phys. Chem. Lett.* **2013**, *4*, 4213-4216.

APPENDICES

APPENDIX A

SUPPORTING INFORMATION FOR CHAPTER 2

A1. Experimental

A1.1. Materials Synthesis and Thin-Film Fabrication. The precursor solution for the $CsPbI_2Br$ thin-films was prepared by dissolving a 1:1 molar ratio of anhydrous PbI_2 and CsBr salts in DMSO at 65 °C. Due to insolubility of CsBr, the PbI_2 was dissolved first then the CsBr was added. Once dissolved, 200 μL of the $CsPbI_2Br$ solution was spin-casted onto a glass substrate for 20 s at 750 rpm. Immediately after spin-casting, the sample was annealed at 65 °C in a saturated DMSO atmosphere for one hour. Thin film samples used for pump-probe microscopy were covered with a microscope slide, using clear enamel to seal the edges after annealing.

A1.2. Assignment of XRD Peaks. Figure A1 shows the calculated XRD pattern based on published crystallography data for $CsPbBr_3$ in black and the experimental XRD pattern (Cu Kα) taken of fabricated $CsPbI_2Br$ thin films in red.[77] Comparison of the two patterns shows that the fabricated materials adopt an orthorhombic geometry and are highly crystalline. Because iodine has a larger ionic radius than bromine, peaks in the $CsPbI_2Br$ pattern are shifted to lower angles, relative to $CsPbBr_3$.

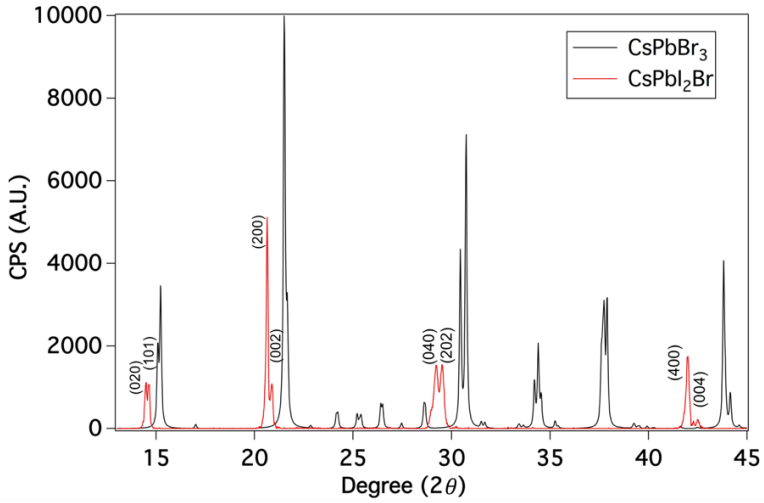

Figure A1. XRD pattern comparison for $CsPbBr_3$ and $CsPbI_2Br$. The black trace corresponds to the calculated XRD pattern based on published crystallography data and the red trace corresponds to the experimental XRD pattern taken of a $CsPbI_2Br$ thin film. Miller indices are indicated next to each experimental peak.

Table A1. XRD peak comparison between $CsPbBr_3$ and $CsPbI_2Br$. The decrease in scattering angle for $CsPbI_2Br$ relative to $CsPbBr_3$ corresponds to a ~4% increase in the lattice along each axis direction.

Miller Index	$CsPbBr_3$ Degree (2θ)[77]	$CsPbI_2Br$ Degree (2θ)
020	15.10	14.48
101	15.22	14.64
200	21.50	20.64
002	21.66	20.88
040	30.44	29.22
202	30.74	29.52
004	43.80	42
400	44.16	42.28

A1.3. $CsPbI_2Br$ Absorption Coefficient. To determine the absorption coefficients of the materials we first collected pump (2.25 eV) transmission images of several single crystalline domains, to calculate extinction at each location on an individual domain (Figure S2 (A)). Next, correlated atomic force micrographs (AFM) were collected to determine the thickness of the domains as shown in Figure S2 (B). Finally, by plotting absorbance vs. thickness, we calculate the absorption coefficient with a linear fit, as shown in Figure S2 (C). This calculation was performed on three different grains. The average absorption coefficient of e = 2 x10-3 nm-1 (2 μm-1) was used for calculating excitation densities (see below).

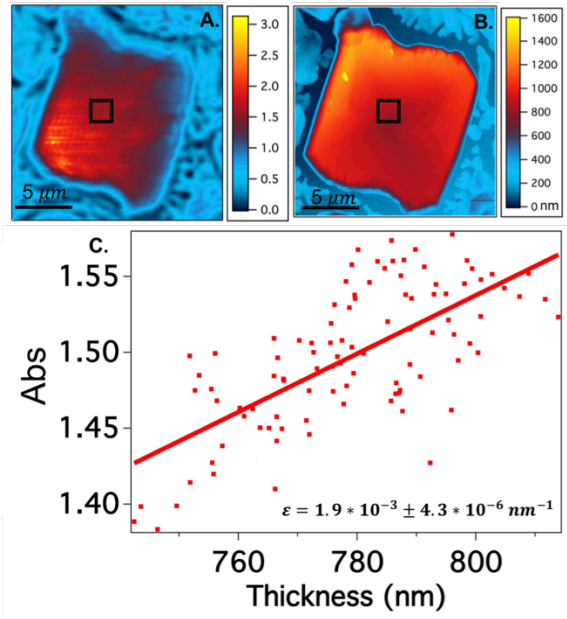

Figure A2. Correlated AFM and pump transmission images for absorption coefficient calculation. (A) Extinction image of a CsPbI2Br domain collected by measuring pump transmission through the domain. The corresponding color scale shows calculated absorption. (B) Corresponding AFM image of the single crystalline domain where the corresponding color scale is in nanometers. (C) Representative plot of absorbance vs thickness of the domain for the area indicated by the black square in images A and B. The slope of the fitted line is the absorption coefficient ($\varepsilon = 2\ \mu m^{-1}$).

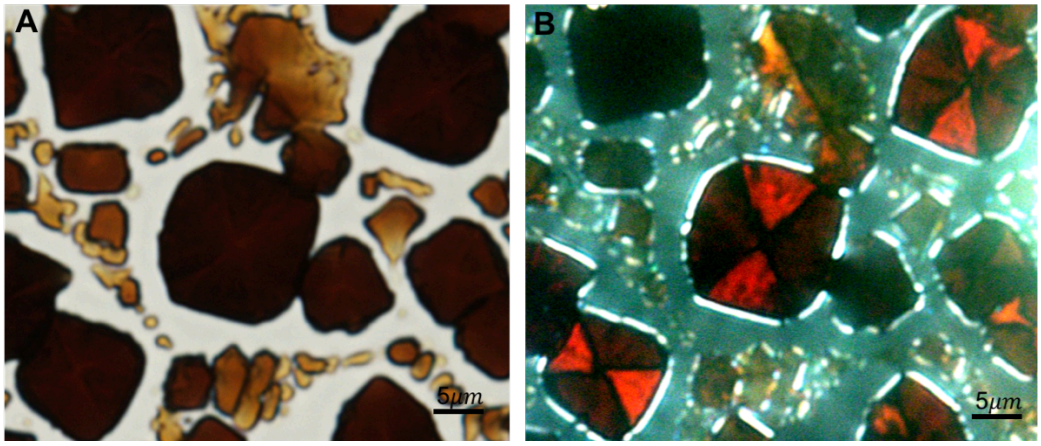

Figure A3. Polarized light microscopy. (A) Bright field image of faceted perovskite domains. (B) Cross polarized image of the same domains as in A, highlighting different crystalline orientations.

A1.4. Microscopy Methods. Pump-probe experiments were carried out using a home-built ultrafast pump-probe microscope. The primary excitation source is a Ti:sapphire laser that emits 70 fs pulses at 80 MHz and has a tunable range of 690 and 1040nm. The fundamental is split via a 50:50 beam splitter (b/s) into two separate lines, the pump and probe. The probe is aligned onto a translation state then coupled onto galvanometer mirrors. The pump is coupled into a photonic crystal fiber (PCF) creating a continuum pump pulse from which the 2.25 eV light is selected with interference filters. Pump and probe are recombined using a 50:50 b/s then focused onto the sample using a 0.90 numerical aperture microscope objective. The substrate is mounted onto a piezoelectric x-y stage, which is used to scan the sample across the pump-probe fields. The reflected probe signal is detected using a balanced photodiode coupled to a lock-in amplifier.

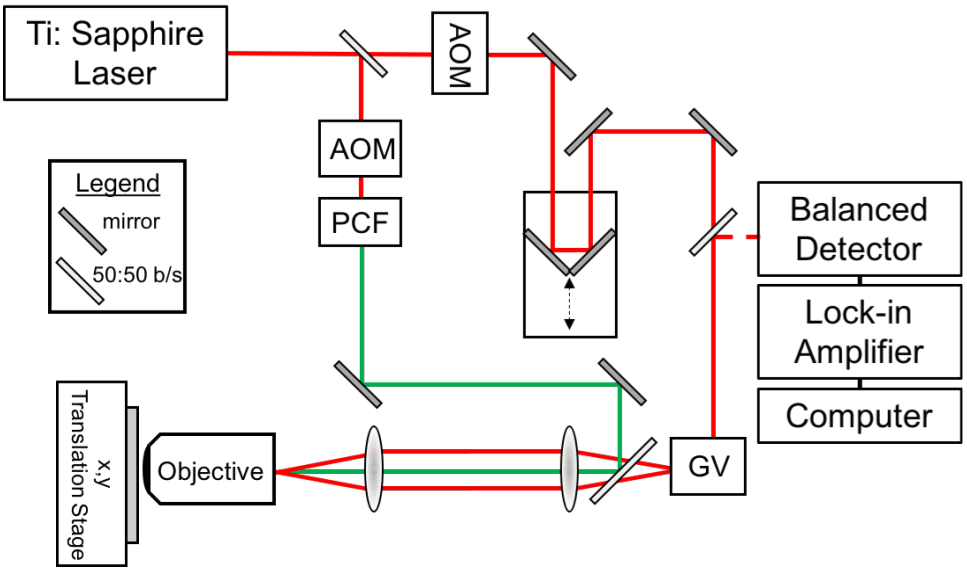

Figure A4. Diagram of homebuilt femtosecond microscope. AOM: Acousto-optic modulator, GV: galvanometer mirrors, and b/s: beam splitter.

A1.5. Obtaining Profiles for Diffusivity Measurements. Spatially separated images are integrated along either the horizontal or vertical axis to obtain longitudinal or lateral profiles of the photoexcited carrier distribution at a specific time delay. The profiles are then fit to a Gaussian distribution to extract a time dependent fwhm from which the diffusivity constant is determined. While lateral drift of the microscope during the course of the experiment can move the center of the profiles ~ 40 nm, the width of the profiles is unaffected. To account for the frame-to-frame drift, we allow the parameter describing the center of the Gaussian model to float in the fitting procedure.

A2. Data Analysis

A2.1. Calculation of Pump Fluence and Carrier Density. The focused pump-pulse is modeled as a two-dimensional Gaussian:

$$G[r] = \frac{I_0\, Log[2]}{\beta^2\, \pi} Exp\left[\frac{-4\, Log[2]\, r^2}{\beta^2}\right] \qquad \text{(S1)}$$

Where I_0 is the measured energy of the pump pulse accounting for transmittance of 550 nm light through the microscope objective, and β is the full-width at half-maximum of the focused beam on the sample. Fluences were calculated using Eq S2 and assuming a 1/e width, $r_0 = 0.60^* \beta$.

$$\frac{\int_0^{2\pi}\int_0^{r_0} G[r]\, r\, \partial r\, \partial\theta}{\int_0^{2\pi}\int_0^{r_0} r\, \partial r\, \partial\theta} \qquad \text{(S2)}$$

Carrier densities are calculated using Eq. S3, assuming an absorption coefficient of $\varepsilon = 2\ \mu m^{-1}$:

$$\frac{\int_0^{2\pi}\int_0^{r_0}\int_0^{1/\varepsilon} G[r]\, \varepsilon\, Exp[-\varepsilon\, z]\, r\, \partial z\, \partial r\, \partial\theta}{\int_0^{2\pi}\int_0^{r_0}\int_0^{1/\varepsilon} r\, \partial z\, \partial r\, \partial\theta} \qquad (S3)$$

A2.2. Photoluminescent Lifetime via Time Correlated Single Photon Counting (TCSPC). TCSPC kinetics of a CsPbI2Br thin film were collected at the peak of the steady state emission spectrum (1.87 eV) after excitation at 2.25 eV. A fit to the kinetics reveals a short 444 ps lifetime and long 6.16 ns lifetime.

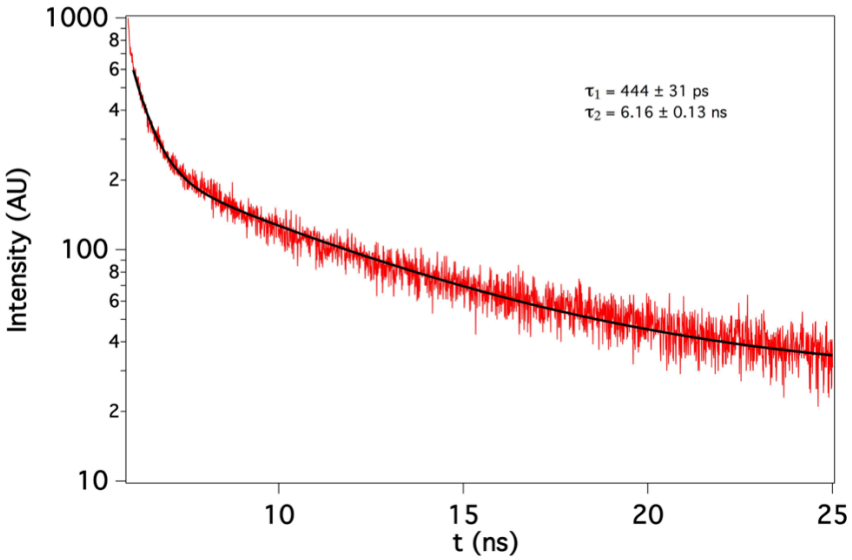

Figure A5. TCSPC for photoluminescent (PL) lifetime. TCSPC measurement of CsPbI2Br thin film. The collected data was globally fit to two exponentials to reveal a short 444 ± 31ps lifetime and a longer 6.13 ± 0.13 ns lifetime.

A2.3. Transient Reflectivity Kinetics. The following table shows the fit parameters (with corresponding 90% confidence error margin) for the data shown in Figure 3A for two separate models, one including k2 and one without. When the data is fit to all three parameters (k1, k2 and k3), k2 is zero within error. Further, k1 and k3 remain the same, within error, for both fits.

Table A2. Power dependent kinetics fit parameters. Shown in this table are the resulting parameters from two different global fits of the kinetics data shown in Figure 3A. When the data is fit to all three parameters, k*2* is zero within error. k*1* and k*3* remain the same, within error, for both fits.

Fit Equation	k_1	Error (±)	k_2	Error (±)	k_3	Error (±)
$\frac{dn}{dt} = -k_1 n[t] - k_2 n[t]^2 - k_3 n[t]^3$	8.9×10^{8}	0.5×10^{8}	-0.6×10^{-11}	1.0×10^{-11}	5.9×10^{-30}	0.5×10^{-30}
$\frac{dn}{dt} = -k_1 n[t] - k_3 n[t]^3$	8.7×10^{8}	0.1×10^{8}	—	—	5.6×10^{-30}	0.1×10^{-30}

APPENDIX B

SUPPORTING INFORMATION FOR CHAPTER 3

B1. Experimental

B1.1. Material Synthesis and Thin-Film Fabrication. Precursor solutions for $CsPbBr_3$ thin-films were prepared by dissolving a 1:1 molar ratio of $PbBr_2$ and CsBr in DMSO at 65 °C. Due to insolubility of CsBr, $PbBr_2$ was dissolved first and then CsBr was added. Precursor solutions for $MAPbBr_3$ thin-films were prepared by dissolving a 1:1 molar ratio of $PbBr_2$ and dehydrated MABr in DMF at 65 °C. Once precursors solutions were prepared, 200 μL of either $CsPbBr_3$ or $MAPbBr_3$ solution was spin-casted onto a glass substrate for 20s at 750 rpm. Immediately after spin-casting, $CsPbBr_3$ samples were annealed at 85 °C in a saturated DMSO atmosphere and $MAPbBr_3$ samples were annealed at 80 °C in a saturated DMF atmosphere, each for one hour. After the annealing process, thin film samples were covered with a microscope slide and sealed using clear enamel. $MAPbI_3$ samples were prepared as previously described.[85]

B1.2. Ultrafast Microscopy. Pump-probe experiments were carried out using a home-built ultrafast pump-probe microscope. The primary excitation source is a Ti: sapphire oscillator which emits 70 fs pulses at 80 MHz and is tunable between 690 and 1040nm. The fundamental (850nm for $CsPbBr_3$ and 800nm for $MAPbBr_3$) is split into two separate lines, the pump and probe. The probe is aligned onto a translation stage, then coupled onto a set of galvanometer mirrors. The translation stage is used to temporally separate the pump and probe pulses and galvanometer mirrors are used to scan the probe and pump beams independently of one another. The pump is frequency doubled via a BBO crystal then recombined with the probe using a dichroic beam splitter. Both the pump and probe are sent through a 4f lens system before being coupled into a

second set of galvanometer mirrors and passed through a second 4f lens system. The two coupled 4f-galvanometer pairs provide the ability to independently position pump and probe. Finally, the pump and probe are focused onto the sample using a 100x (0.90NA) microscope objective. The reflected probe signal is detected using a balanced photodiode coupled to a lock-in amplifier.

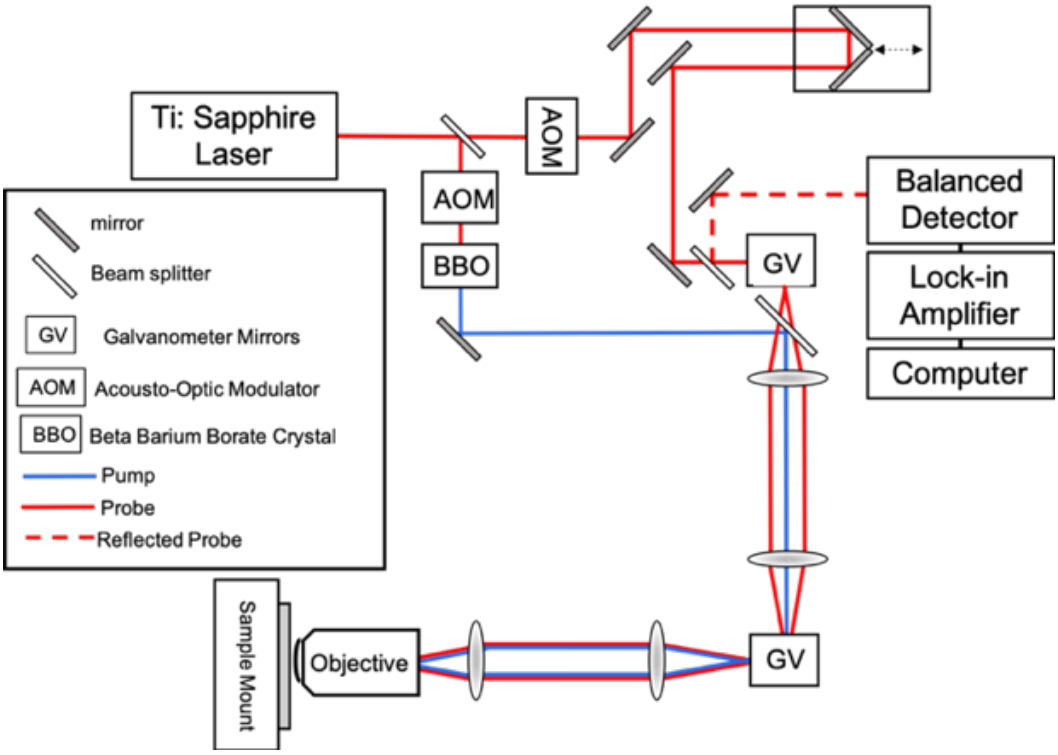

Figure B1. Diagram of homebuilt femtosecond microscope.

B2. Data Analysis

B2.1. Gaussian Pump Spot Size and Carrier Density. The focused pump-pulse is modeled as a two-dimensional Gaussian:

$$g[r] = \frac{I_0 \, \mathrm{Log}[2]}{\beta^2 \, \pi} \mathrm{Exp}\left[\frac{-4 \, \mathrm{Log}[2] \, r^2}{\beta^2}\right] \qquad \text{(B1)}$$

I_0 is the measured energy of the pump pulse, accounting for transmittance of the pump light through the microscope objective and reflection off the cover slip and sample. β is the full-width at half-maximum of the focused beam on the sample. To determine β, a SiC nanowire of sub-diffraction width (~140nm) is imaged by the pump beam and fit by a model which convolves a hemispherical profile (defined to be the same width of the nanowire, as determined by scanning electron microscopy) with a gaussian pump pulse. Modeling performed on three different SiC nanowires produced an average pump FWHM of $\beta \approx 300\mathrm{nm}$. Fluence is calculated using Eq. B2, where r_0 is the $1/e^2$ width of the pulse.

$$G[r] = \frac{\int_0^{2\pi} \int_0^{r_0} g[r] \, r \, \partial r \, \partial \theta}{\int_0^{2\pi} \int_0^{r_0} r \, \partial r \, \partial \theta} \qquad \text{(B2)}$$

Carrier densities are calculated using Eq. B3, where α is the extinction coefficient of the material.

$$N = \frac{\int_0^{2\pi} \int_0^{r_0} \int_0^{1/\alpha} G[r] \, \alpha \, \mathrm{Exp}[-\alpha \, z] \, r \, \partial z \, \partial r \, \partial \theta}{\int_0^{2\pi} \int_0^{r_0} \int_0^{1/\alpha} r \, \partial z \, \partial r \, \partial \theta} \qquad \text{(B3)}$$

B2.2. Carrier Diffusion. Carrier diffusion was measured by directly imaging the spatial evolution of the excited state. For these spatially separated measurements, the probe is scanned over the excited pump volume at a series of increasing pump-probe delay times. Each image is integrated along one axis and the resulting profiles are fit to gaussians. The squares of the time-dependent FWHMs are plotted vs. time. The slope of the fit is proportional to the diffusion constant via:

$$\Delta\beta^2 = \beta(t_0)^2 + 16\ln(2)\, D_{am} \cdot (\Delta t - t_0) \qquad \text{(B4)}$$

$\beta(t_0)^2$ is the square of the normalized excited-state distribution profile FWHM when $\Delta t = 0$ and D_{am} is the ambipolar diffusion constant.

B2.3. Carrier Density Dependence of ΔR. Panels (A) and (C) of Figure B2 show representative TR decay kinetics taken from individual $CsPbBr_3$ and $MAPbBr_3$ perovskite domains, respectively. Panels (B) and (D) illustrate the linear dependence of $-\Delta R_{t=0}$ on carrier density over the entire range measured ($1.48\times 10^{18} - 1.19 \times 10^{19} cm^{-3}$

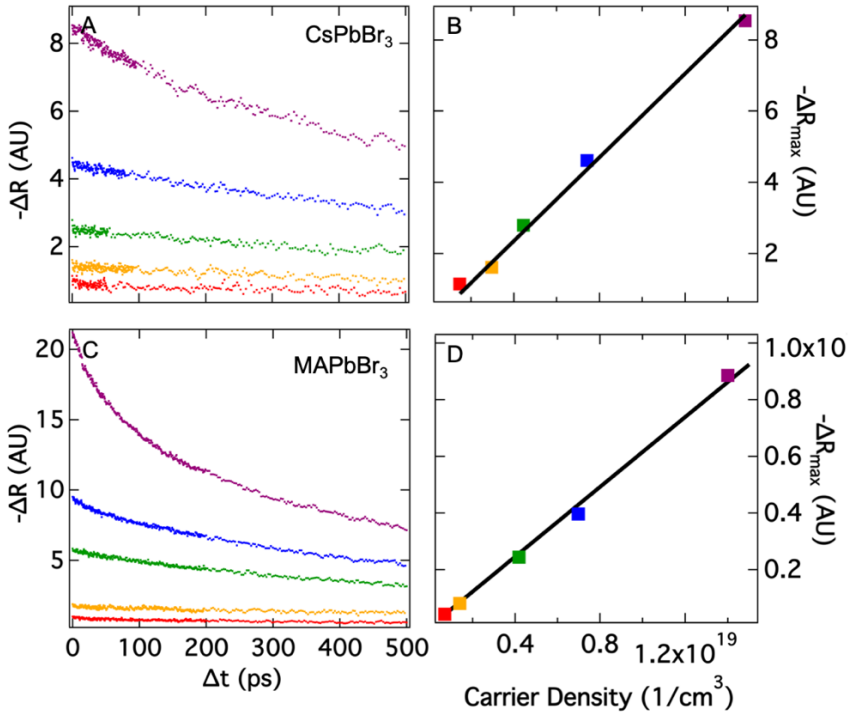

Figure B2. Excitation-Fluence dependent TR decay kinetics. Red, yellow, green, blue and purple dots correspond to kinetics data taken on $CsPbBr_3$ (A) and $MAPbBr_3$ (C) at increasing carrier densities scaled to the lowest carrier density measured ($1.48\times 10^{18}\mathrm{cm}^{-3}$ for $CsPbBr_3$ and $6.98\times 10^{17}\mathrm{cm}^{-3}$ for $MAPbBr_3$. Panels (B) and (D) shows that $-\Delta R$ at $\Delta t = 0$ ps scales linearly with carrier density up to $1.48\times 10^{19}\mathrm{cm}^{-3}$ and $1.40 \times 10^{19}\mathrm{cm}^{-3}$ for $CsPbBr_3$ and $MAPbBr_3$, respectively. Note the y-intercepts on each of the fits is equal to 0.

B2.4. Nonlinear Carrier Recombination. Figure B3 shows a series of excitation dependent kinetics taken on an individual $CsPbBr_3$ domain. Low fluence recombination occurs primarily via first-order (trap-mediated) processes, as shown by the black dots in Fig. B3A. To best visualize contributions from higher-order processes to the observed recombination dynamics, we have removed contributions from first-order processes. Figure B3B shows the kinetics in (A) with the time dependent amplitude of the lowest fluence trace (black dots) subtracted from each kinetics trace in the series. To quantitate

the fraction of carriers recombination occurring via second and third order processes, ($\Delta\Delta R_{NORM}$), the magnitude of each trace in Fig. B3B at $\Delta t = 600ps$ was normalized to the initial decay of the lowest fluence trace and then plotted vs. carrier density (Fig. 4.3D).

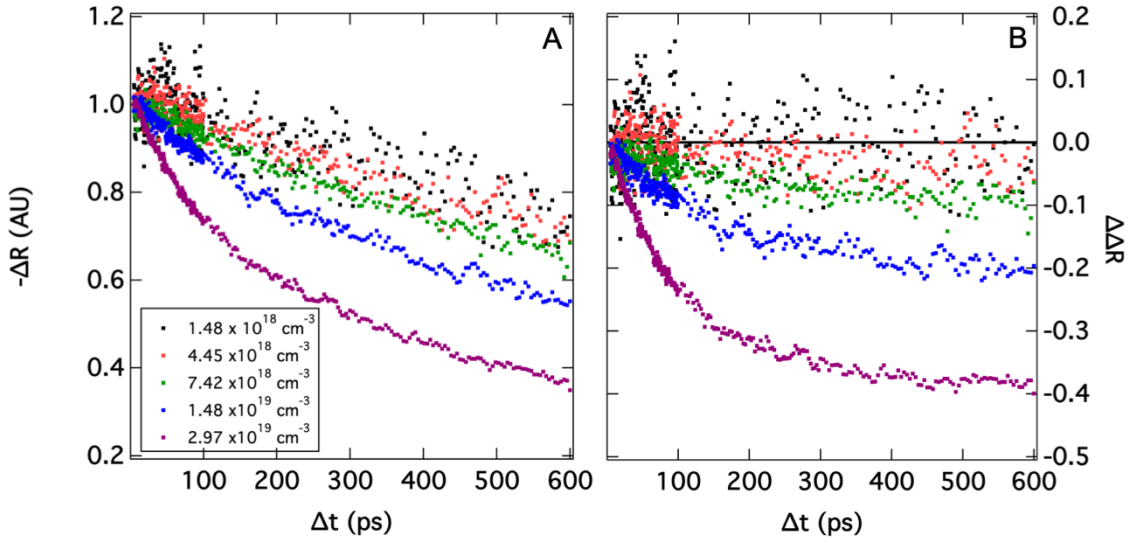

Figure B3. Higher-order carrier recombination. Panel (A) shows a series of excitation-fluence dependent kinetics measurements taken on a single crystalline $CsPbBr_3$ perovskites. Panel (B) shows the kinetics measurements in (A) after removing contributions from first-order recombination.

Figure B4 compares $\Delta\Delta R_{norm}$ values determined from modeled recombination kinetics, where k_1 is increased from $k_1 = 0.0007\ ps^{-1}$ (Fig S4A) to $k_1 = 0.0012\ ps^{-1}$ (Fig B4B). These values of k_1 give rise to kinetics that closely approximate the difference in low-density recombination kinetics in Figure 4.3A and 4.3C. For a given set of nonlinear recombination coefficients, $k_2 = 2.0 \times 10^{-10}\ \mu m^3/ps$, and $k_3 = 1.0 \times 10^{-18}\ \mu m^6/ps$, the difference in the $\Delta\Delta R_{norm}$ determined from the kinetics (Fig B4C) lies within the experimental uncertainty.

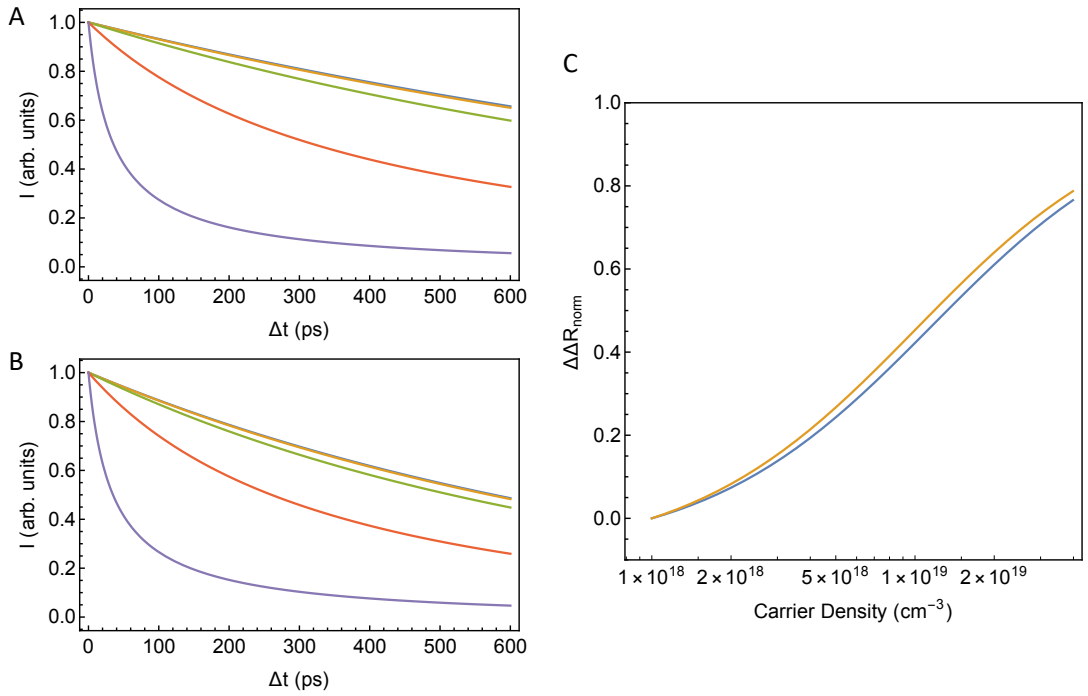

Figure B4. Effects of faster first order recombination on ΔΔR determination. Panel A shows modeled recombination kinetics (between 1×10^{18} and 4×10^{19} cm^{-3}) assuming a first order rate constant of $k_1 = 0.0007$ ps^{-1}, a second order term, $k_2 = 2.0 \times 10^{-10}$ $\mu m^3/ps$, and a third order term, $k_3 = 1.0 \times 10^{-18}$ $\mu m^6/ps$. Panel B shows modeled decay kinetics with the nonlinear recombination terms held constant and with $k_1 = 0.0012$ ps^{-1}. Panel C shows a comparison of ΔΔR determined at Δt = 600 ps for the kinetics shown in panels A (yellow) and B (blue).

Estimation of error in measured D_{am} introduced by nonlinear recombination: In a continuum approximation of the photoexcited carrier density, the temporal and spatial evolution is given (in one dimension) by,

$$\frac{\partial n(t)}{\partial t} = D_{am}\frac{\partial^2 n(t)}{\partial x^2} - k_1 n(t) - k_2 n(t)^2 - k_3 n(t)^3. \qquad \text{(B5)}$$

The first term describes the diffusive motion of charges, and k_1, k_2, and k_3 describe trap-mediated, radiative (bimolecular), and Auger recombination, respectively. Because the center of the excitation profile has higher carrier density, nonlinear recombination can cause the gaussian carrier profile to "flatten out," which can be

interpreted as an apparently faster diffusive process than the nominal D_{am}. To estimate the magnitude of this effect, we numerically solved Eq. B5 at a series of excitation densities (calculated as described above), convolved the carrier profile with a gaussian to model the spatial scanning of the probe beam in our instrument, and fit the resultant profiles to extract the diffusion coefficient (also as described above for experimental measurements). Figure B5 shows the results of this modeling. Panel A shows power-dependent recombination kinetics. At high densities, the nonlinear recombination terms enhance recombination leading to faster decay. Panels B and C show profiles from low and high initial carrier densities. Panel D shows the fit-determined diffusion constants determined by fitting these profiles. In the case of higher excitation density, the nonlinear recombination causes an apparent 13% increase in the measured diffusion coefficient.

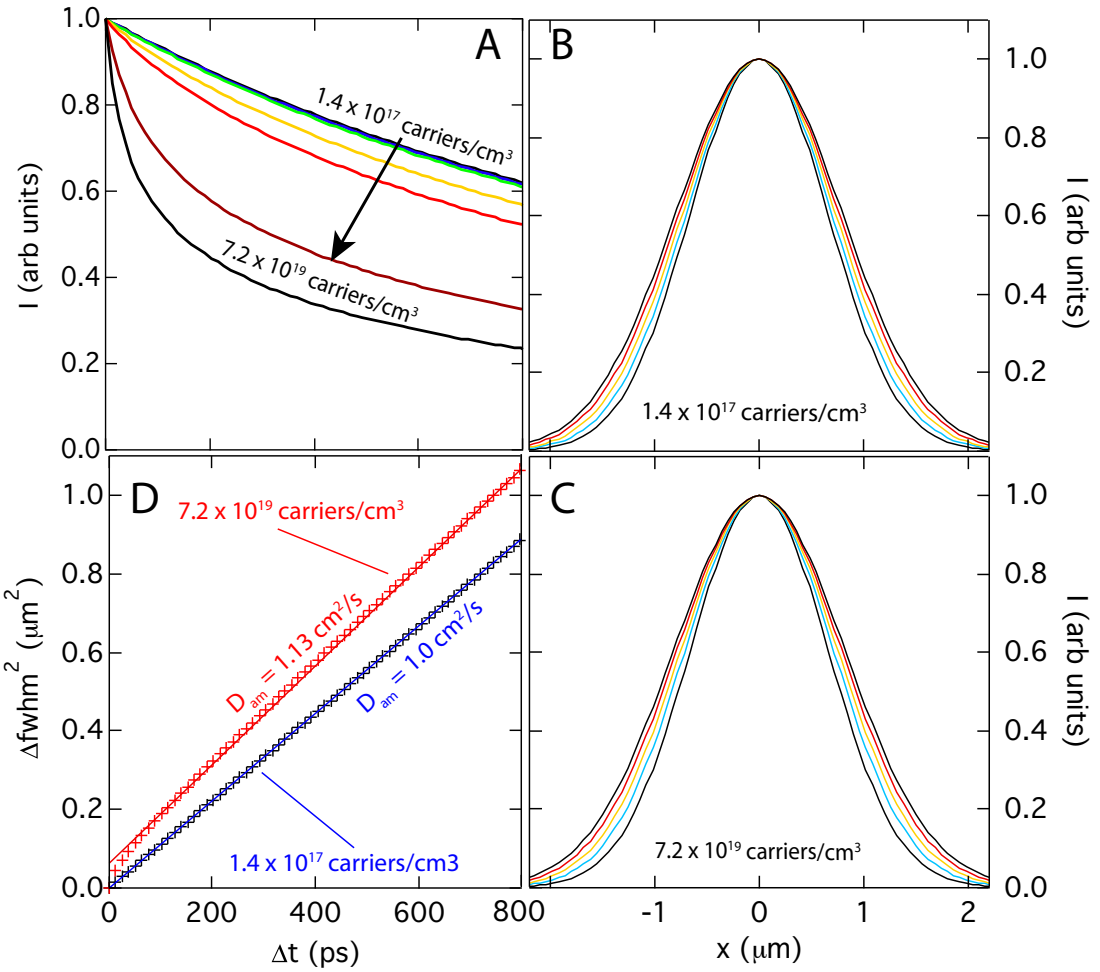

Figure B5. Estimation of error associated with nonlinear recombination. Panel A shows modeled kinetics for increasing excitation densities from 1.4×10^{17} cm^{-3} to 7.2×10^{19} cm^{-3}, assuming $D_{am} = 1.0$ cm^2/s, $k_1 = 2 \times 10^{-4}$ ps^{-1}, $k_2 = 1 \times 10^{-10}$ cm^3 s^{-1}, and $k_3 = 1 \times 10^{-29}$ cm^6 s^{-1} and a 300 nm fwhm gaussian pump pulse. Panels B and C show the time dependent profiles (at $\Delta t = 0$, 250, 500, 750, and 1000 ps), obtained by convolving the probe with the evolving carrier density. Panel D shows the difference in apparent diffusion coefficients, obtained by finding the slope of a best-fit line to the $fwhm^2(\Delta t)$ obtained from profiles like those shown in panels B and C. The apparent 13% increase in D_{am} at high excitation densities is a result of nonlinear recombination, which decreases the signal amplitude near the middle of the profiles (panels B and C) where carrier density is highest.

B2.5. Optical Dielectric. Given a probe energy far below the optical bandgap of the material, the optical dielectric is given by the square of the real index of refraction ($\epsilon_\infty = n^2$). To determine n, both a ground state reflective image (GSR) and an atomic force micrograph (AFM) of a single domain are collected. The two images (GSR and AFM) are pixel matched and interpolated so that correlated data points from each image lay at the same grid position. A median filter is applied to the GSR image to eliminate any low frequency background and center the fringes at R = 0. The filtered ground state images are fit with a Gaussian broadened transfer matrix model to account for the limited spatial resolution of the microscope. A detailed description of the transfer matrix fitting protocol can be found in a previous publication.[100] A representative example of the transfer matrix fitting protocol (TMF) applied to a $CsPbBr_3$ domain is shown in Figure B6.

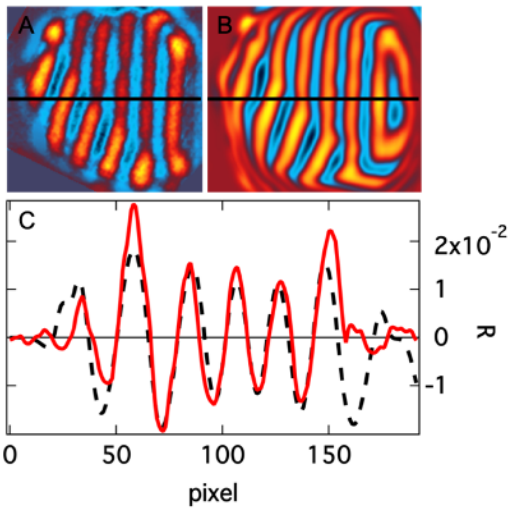

Figure B6. Determination of n in an individual $CsPbBr_3$ domain. (A) Experimental and (B) modeled ground state reflective image of a $CsPbBr_3$ domain assuming a refractive index of n = 2.3. (C) Slices of the GSR image (red) and modeled image (black) taken from the black lines in figures (A) and (B), respectively. Note deviations from the model near the edge of the domain are primarily due to surface roughness.

B2.6. Steady State Spectra. Scanning electron micrographs (SEMs) representative of single crystalline domains on $MAPbBr_3$ (Fig. B6A) and $CsPbBr_3$ (Fig. B6B) thin-films are shown below. The corresponding absorption and emission spectra determine a bandgap energy of 2.30eV for $MAPbBr_3$ and 2.37eV for $CsPbBr_3$.

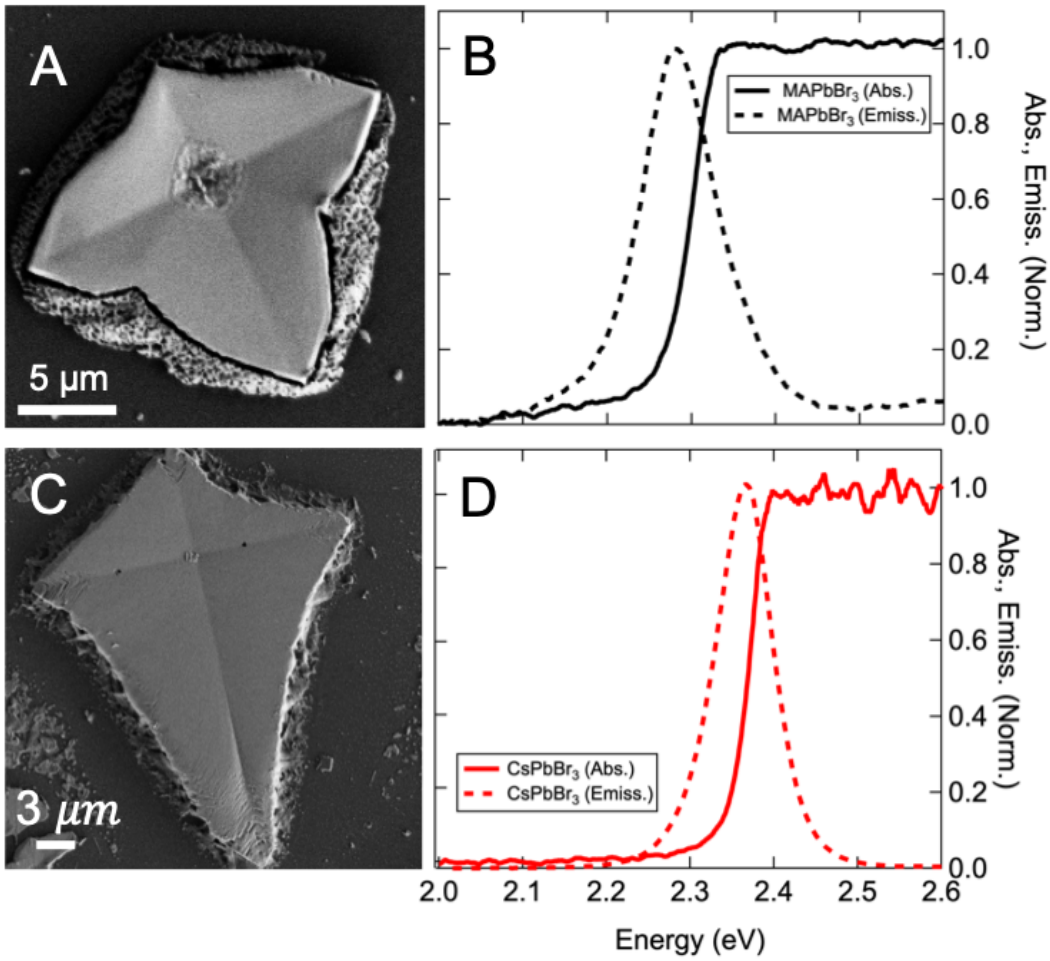

Figure B7. Steady state spectra of $MAPbBr_3$ and CsPbBr. (A) and (C) show representative SEMs of single crystalline $MAPbBr_3$ and $CsPbBr_3$ domains, respectively. (B) and (D) show emission and absorption spectra taken on $MAPbBr_3$ and $CsPbBr_3$ thin-film. The bandgaps for $MAPbBr_3$ and $CsPbBr_3$ are 2.30eV and 2.37eV, respectively.

B1.7. Reported Reduced Masses. The following table lists reduced masses reported in literature for the three perovskite species study in this manuscript.

Table B1. Reported reduced masses. The range of reduced masses reported in the literature for $CsPbBr_3$, $MAPbBr_3$ and $MAPbI_3$ is 0.104 to 0.144.

Perovskite	μ
$CsPbBr_3$	0.126[165], 0.073[166], 0.115[16]
$MAPbBr_3$	0.144[167], 0.117[168]
$MAPbI_3$	0.135[167], 0.128[169], 0.104[168]